UC Berkeley
UC Berkeley Electronic Theses and Dissertations

Title
Exciton dominated optical properties of atomically thin semiconductors

Permalink
https://escholarship.org/uc/item/2fw4r5f4

Author
Yao, Kaiyuan

Publication Date
2019

Peer reviewed|Thesis/dissertation

eScholarship.org Powered by the California Digital Library
University of California

Exciton Dominated Optical Properties of Atomically Thin Semiconductors

By

Kaiyuan Yao

A dissertation submitted in partial satisfaction of the
requirements for the degree of
Doctor of Philosophy
in
Mechanical Engineering
in the
Graduate Division
of the
University of California, Berkeley

Committee in charge:
Professor Liwei Lin, Co-chair
Professor P. James Schuck, Co-chair
Professor Chris Dames
Professor Wick Haxton

Spring 2019

Exciton Dominated Optical Properties of Atomically Thin Semiconductors

© Copyright by Kaiyuan Yao 2019

Abstract

Exciton Dominated Optical Properties of Atomically Thin Semiconductors

By

Kaiyuan Yao

Doctor of Philosophy in Mechanical Engineering

University of California, Berkeley

Professor Liwei Lin, Co-chair

Professor P. James Schuck, Co-chair

Atomically thin transition metal dichalcogenides (TMDs) are a new family of semiconductors with exciting optical properties for practical applications in optoelectronic devices, as well as intriguing many-body behaviors for fundamental explorations in condensed matter physics. In bulk form they are van der Waals layered materials and have been traditionally used as industrial lubricants. When thinned down to monolayers they surprisingly become direct band gap semiconductors with exceptionally strong light-matter interactions dominated by exciton effects. In these monolayer semiconductors, excitons can be robustly observed even at room temperature, in contrast to conventional bulk semiconductors where the electron-hole binding energies are typically lower than the room temperature thermal energy. The strong excitonic effect is a direct result of both fundamental quantum confinement effects and reduced dielectric screening in a two-dimensional system. This dissertation presents experimental investigations on a few central questions in these materials: how strong is the electron-hole binding effect in the prototypical monolayer semiconductor MoS_2 as well as in novel metal-chalcogenolate hybrid materials; how can exciton effects be tuned by carrier doping and controlled by electrostatic gating in real devices; and how can excitons coherently enhance nonlinear optical transitions for the development of novel nonlinear devices and imaging techniques.

The dissertation starts with an introduction to interband optical transitions including exciton effects in low-dimensional electronic systems. The focus is on providing a many-body physical picture for better understanding experimental phenomena, and not as much on a detailed quantitative treatment. Then three major research works surrounding this topic are included in the dissertation. First, we study carrier-induced quasiparticle band gap and exciton energy renormalization effects in monolayer MoS_2. We show that both the quasiparticle band gap and the exciton binding energy can be largely tuned by applying electrostatic gating to a monolayer device. In the second work, we investigate exciton dominated optical properties of a family of "bulk 2D" materials: self-assembled hybrid metal organic chalcogenolate multi quantum wells. Owing to the weak interlayer electronic coupling, the exciton binding energy in these multilayered bulk materials are shown to be close to a true monolayer semiconductor. We also reveal the bright and

dark exciton species by cryogenic photoluminescence excitation spectroscopy, providing further evidence of high exciton binding energy in the bulk layered crystal. In the third work, we come back to atomically thin TMDs and study how exciton resonances greatly enhance their nonlinear optical responses, leading to successful continuous-wave generation of nonlinear signals from monolayer TMDs. Finally, in addition to optical spectroscopy studies, we also present two examples of device applications of two-dimensional materials in micro-electromechanical systems (MEMS). In one example we demonstrate micro strain sensors based on the two-dimensional electron gas formed at the interface of AlGaN/GaN. In the second example we demonstrate efficient ultraviolet photodetectors using graphene/diamond heterojunctions. Together these studies provide crucial knowledge on the utilization and control of exciton enhanced linear and nonlinear optical properties of atomically thin semiconductors and related low-dimensional materials, and guidance towards practical optoelectronic device applications.

To my parents and my fiancé

Table of Contents

Chapter 1 - Introduction 1
1.1 Overview 1
1.2 Interband optical transitions of semiconductors in a single particle picture. 2
1.3 Tightly bound Wannier excitons 6
1.4 Nonlinear optics with atomically thin semiconductors 10
Chapter 2 – Carrier induced renormalization of quasiparticle band gap and exciton binding energies in monolayer MoS_2 14
2.1 Introduction 14
2.2 Identification of quasiparticle band gap from photoluminescence excitation spectroscopy 14
2.3 Experimental observation of carrier induced renormalization effects 18
2.4 Conclusion 21
2.5 Additional contents 22
2.5.1 Material growth and device fabrication 22
2.5.2 Photoluminescence excitation spectroscopy and analysis 22
2.5.3 Identification of exciton and trion states from reflectivity spectra. 27
2.5.4 Determination of gate induced doping concentration from Stokes shift 28
2.5.5 Additional results 29
Chapter 3 – Strongly quantum confined excitons in two-dimensional layered hybrid metal chalcogenide multi quantum wells 31
3.1 Introduction 31
3.2 Crystal structure and electronic band structure of mithrene 31
3.3 Optical characterization of mithrene samples 33
3.4 Revealing bright and dark excitonic states and exciton binding energy with photoluminescence excitation spectroscopy 35
3.5 Ultrafast exciton dynamics of mithrene 37
3.6 Effect of different organic ligands on exciton states 39
3.7 Conclusion 40
3.8 Additional contents 40
3.8.1 Raman spectra of AgSe quantum wells confined by barrier layers of different organic ligands 41
3.8.2 Temperature dependent photoluminescence and emergence of defect-bound excitons 41
3.8.3 Measurement of photoluminescence quantum yield 42
3.8.4 Hyperspectral PL imaging showing uniform distribution of PL energy 43

3.8.5 Photoluminescence excitation (PLE) experiments and temperature dependent PLE spectra ... 44
3.8.6 Temperature dependent time resolved photoluminescence measurements and data fitting ... 47
3.8.7 Additional results from DFT calculation ... 48
3.8.8 Material synthesis ... 48
Chapter 4 – Continuous-wave nonlinear optics with atomically thin semiconductors and van der Waals heterostructures ... 50
4.1 Introduction ... 50
4.2 Second harmonic generation with continuous-wave excitation ... 51
4.3 Revealing the role of excitonic emission resonance in nonlinear transitions by sum frequency excitation spectroscopy ... 53
4.4 Linear and circular polarization dependence of sum frequency generation ... 56
4.5 Imaging interlayer electronic coupling in twisted heterobilayer transition metal dichalcogenides ... 58
4.6 Conclusion ... 59
4.7 Additional contents ... 60
4.7.1 Accounting for interference local field effects on nonlinear characterization and excitation spectroscopy ... 60
4.7.2 Layer-dependent continuous wave SHG and SFG ... 62
4.7.3 Second order helicity selection rules in monolayer TMD crystals ... 62
4.7.4 Determination of the twist angle of heterobilayer sample with polarization dependent SHG ... 63
Chapter 5 - Two-dimensional materials and heterojunctions for applications in microelectromechanical systems (MEMS) ... 65
5.1 Overview ... 65
5.2. A flexible solar-blind UV detector based on graphene-microcrystalline diamond heterojunctions ... 65
5.3 Piezoelectricity-induced Schottky barrier height variations in AlGaN/GaN high electron mobility transistors ... 76
Bibliography ... 82

Acknowledgements

Foremost, I would like to express my sincere gratitude to my advisors, Professor P. James Schuck and Professor Liwei Lin for their valuable guidance throughout my time as a graduate student.

Prof. Schuck has been of enormous help to keep my research on a promising track of scientific progress. I have benefited tremendously from his genius insights in science and wise choice of research directions. For all the time Jim also provides me many valuable opportunities to learn to work collaboratively with other great scientists, which I believe to be extremely beneficial in the long run. Moreover, Jim is always encouraging, positive and supportive, which turns out to be an essential boost to my confidence and motivation for keep doing science.

Prof. Lin has always offered wise advice and extensive freedom to my research works over the entire six years. He also sets up an excellent example of a responsible and dedicated scientist as well as a great person.

During my graduate study, I'm extremely fortunate to receive vast support from my colleagues and collaborators. Particularly, I'm highly grateful to Dr. N.J. Borys who provided excellent mentorship for my projects on far field optics and a lot of insights on photophysics. I'm also highly grateful to Dr. J. Nathan Hohman, Prof. Jeffrey B. Neaton, Prof. Alex Zettl, Prof. Sefaattin Tongay, Prof. Chenming Hu, Dr. Emory Chan, Prof. James Hone, Prof. Dmitri Basov and their groups for the collaboration on material synthesis, device fabrications, theoretical calculations, and all the extremely helpful discussions. I'd also like to acknowledge Dr. Edward Barnard, Dr. Angel F. Bravo, Thomas Darlington and all Schuck group members, as well as Dr. Chen Yang, Dr. Firas Sammoura, Dr. Xining Zang, Dr. Yumeng Liu, Dr. Minsong Wei, Prof. Caiwei Shen, and all members of Linlab.

I would like to thank my parents for their unconditional support and understanding during my graduate study. I always try to look ahead and move fast, but sometimes forget the hands that push me from the back. They also set great examples for being a responsible, diligent, and kind person.

Last but most importantly, this dissertation is dedicated to my fiancé Dr. Fan Cui. She can always enlighten my life in the darkest times, and has been a constant source of support and encouragement during the challenges of graduate school. She is also the best listener to my troubles and problems in both work and life, and always supportive in every decision I made. I'm not at all good at writing sweet words, and can never get satisfied with this paragraph, but I know I'm already the luckiest man in the world.

Chapter 1 - Introduction

1.1 Overview

The recent history of two-dimensional (2D) semiconductors starts soon after the discovery of the two-dimensional semimetal graphene [1]. Over the past couple decades, graphene has been inspiring scientists working in all areas: condensed matter physics, electronic devices, optoelectronic and plasmonic devices, energy and battery applications, etc. However, for optoelectronics applications, the lack of a sizable band gap in visible or near infrared range has been a major limiting factor of graphene. In contrast, transition metal dichalcogenides (TMDs) such as MoS_2 and WSe_2 are found to possess a large direct band gap in monolayer form and have become an emerging family of optoelectronic materials [2] [3] [4]. In the bulk and few-layer form TMDs are indirect band gap semiconductors. But when exfoliated down to their monolayer form, direct band gaps emerge at the K and K' valleys in the Brillouin zone. The direct band gap allows for strong light-matter interactions and efficient photoluminescence, making monolayer TMDs promising for building active optoelectronic devices such as LEDs, lasers, etc. [5] [6] [7].

In addition to the long-desired direct gap, atomically thin TMDs provide many other attractive optical properties. One example is circular dichroism and spin-valley locking [8] [9]. Briefly, this means that the two direct gap valleys in momentum space are selectively coupled to either right or left circularly-polarized light for linear optical transition in monolayer TMDs. This is a result of three necessary ingredients that coexist in monolayer TMDs: large spin-orbital coupling, inversion symmetry breaking and time reversal symmetry. For optoelectronic applications, the circular-dichroism effect opens up the possibility for direct optical generation of carriers in a selected valley, which is highly desired for valleytronic and spintronic information processing. Moreover, when different layers of 2D lattices are stacked together, they can be freely twisted with respect to each other thanks to the weak van der Waals interaction, providing an additional knob to engineer the properties of quantum confined materials [10]. These artificially stacked heterobilayer crystals become an intriguing platform for quantum materials and devices, including the quest for interlayer excitonic Bose-Einstein condensation, single-photon emitters [11], programmable Moire excitonic emitters [12], and so on.

The focus of this dissertation is the strong excitonic effects in atomically thin TMDs and multilayered hybrid metal organic chalcogenolate materials. In these 2D electron systems, as a result of strong quantum confinement and reduced dielectric screening, optically excited electrons and holes form tightly bound excitons. These exciton states have a large influence on linear and nonlinear optical properties, which is the main topic of this thesis. In a many-body picture an exciton state is constructed by a coherent constructive superposition of electron-hole pair excitations across the whole momentum space, and therefore the ground state excitons typically have a very large optical oscillator strength compared with that of single particle excitations as determined from joint density of states [13] [14]. Benefits of the strong excitonic resonances include observed giant enhancement in absorption, emission, reflection, and second harmonic generation [15] [16] [17]. In addition, resonance energies and oscillator strengths of the excitons are also highly tunable by carrier concentration, which is conveniently controllable by electrostatic field effect gating [18] [19] [5], making 2D semiconductors particular attractive for tunable devices, optical modulators, as well as sensors and photodetectors in microelectromechanical systems.

1.2 Interband optical transitions of semiconductors in a single particle picture.

This section briefly introduces interband linear optical transitions in semiconductors, providing descriptions for some unique optical properties in atomically thin TMDs, such as the strong direct-gap transition, dimensionality effects on joint density of states, and valley-coupled circular dichroism.

The response of a semiconductor material to electromagnetic excitations can be described by the polarization response function:

$$\mathbf{P}_i = \varepsilon_0(\boldsymbol{\chi}_{ij}^{(1)}\mathbf{E}_j + \boldsymbol{\chi}_{ijk}^{(2)}\mathbf{E}_j\mathbf{E}_k + \boldsymbol{\chi}_{ijkl}^{(3)}\mathbf{E}_j\mathbf{E}_k\mathbf{E}_l + ...) \qquad (1.2.1)$$

This equation empirically describes how the incident electric field induces electric dipole polarizations **P** in the material. The frequency-dependent polarization susceptibility tensors $\boldsymbol{\chi}$ can be directly measured by experiments as well as modeled by light-matter interaction theories at different levels. The first term with $\boldsymbol{\chi}^{(1)}$ describes linear optical response, and the rest of the terms describe higher order nonlinear responses, which are introduced in section 1.4. In this section, we focus on linear optical properties (and will thus omit the superscripts) in a solid state crystal. In many cases it is also common to express the linear optical response in the relative dielectric function tensor $\boldsymbol{\varepsilon}$ with $\boldsymbol{\varepsilon} = 1 + \boldsymbol{\chi}$. For isotropic materials the two response tensors reduce to scalar numbers which are adopted for the following discussion. Both dielectric functions and polarization susceptibilities are generally complex numbers and related to the linear optical refractive index n by $(\tilde{n} + i\tilde{k})^2 = \varepsilon_1 + i\varepsilon_2$. The real and imaginary part of the dielectric function can be calculated from each other based on the Kramers-Kronig relationship [20]. The imaginary part ε_2 is proportional to the frequency-dependent linear optical absorption coefficient α (ω) which can be directly obtained in experiments.

$$\varepsilon_2(\omega) = \frac{c\tilde{n}}{\omega}\alpha(\omega) \qquad (1.2.2)$$

The optical response of a semiconductor comes from different mechanisms, such as Drude response of free carriers (plasmons), lattice vibrations (phonons), and interband electronic transitions (electron-hole pairs), as well as polariton states when these elementary excitations are strongly coupled with light at surfaces or in nanostructures. The research topics covered in this dissertation are mostly related to electronic interband transitions.

The Lorentz oscillator model is a classical model of the dielectric function, and is an intuitive and useful tool for describing and fitting experimental results. In a Lorentz oscillator model, electrons are considered as an ensemble body bound by a harmonic restoring force with resonant frequency of $\omega_0(i)$, and also affected by a friction or damping force Γ [20]. The complex dielectric function $\varepsilon = \varepsilon_1 + i\varepsilon_2$ can be expressed as:

$$\varepsilon(\omega) = \varepsilon_\infty + \sum_i \frac{\omega_p(i)^2}{\omega_0(i)^2 - \omega^2 - j\omega\Gamma}$$

$$\omega_p(i)^2 = \frac{Nq^2}{\varepsilon_0 m_e} \qquad (1.2.3)$$

Here the summation runs over all individual Lorentz oscillators resonant at frequencies $\omega_0(i)$ with oscillator strengths proportional to the oscillator's plasma frequency $\omega_p(i)$. When using the Lorentz oscillator model to describe experimental spectroscopy results, it's not possible to incorporate oscillators at all frequencies, and a high cut-off frequency is typically used. Therefore, a constant term ε_∞ is used to account for contributions from oscillators with resonance frequencies higher than the cut-off frequency. The mathematical form of Lorentz oscillators will naturally satisfy the Kramers-Kronig relationship. Therefore, by implementing densely-spaced oscillators with their plasma frequency $\omega_p(i)$ and linewidth Γ as optimization parameters, the multi-oscillator model can be used to fit experimental reflectance and absorption spectra from semiconductor samples. Application examples on monolayer MoS_2 are shown in Chapter 2 and also [19] [21] [22].

In order to develop insights on how electronic band structure of a specific material affects interband optical transitions, a quantum mechanical treatment will be needed. Although atomically thin semiconductors are highly excitonic in nature, many of their low energy optical properties can also be conceptually and qualitatively understood within a single particle picture. Then the imaginary part of linear dielectric constant can be linked to electronic band structure as [14]:

$$\begin{aligned}\varepsilon_2(\omega) &\sim \frac{1}{\omega^2}\sum_{vc\mathbf{k}}\left|\mathbf{M}_{vc}(\mathbf{k})\right|^2 \delta[E_c(\mathbf{k})-E_v(\mathbf{k})-\hbar\omega] \\ &\sim \frac{1}{\omega^2}\sum_{vc}\left|\mathbf{M}_{vc}\right|^2 J_{vc}(\omega) \end{aligned} \qquad (1.2.4)$$

Here ω is the angular frequency of electromagnetic wave, $\mathbf{M}_{vc}$ is the electric dipole transition matrix element, $J_{vc}(\omega)$ is the joint density of states. The summation runs over all pairs of Bloch states in conduction band and valence band as indexed by *c* and *v*, respectively. When close to a parabolic band edge, $\mathbf{M}_{vc}$ is typically a slowly varying function of $\mathbf{k}$ and may be treated only as a function of ω, leaving the optical absorption mostly governed by the joint density of states.

For Bloch electron states in a solid state crystal, the transition matrix can be evaluated as:

$$\begin{aligned}\mathbf{M}_{vc}(\mathbf{k}) &= < c,\mathbf{k}' \,|\, \mathbf{E}e^{i\mathbf{q}\cdot\mathbf{r}} \cdot \mathbf{p} \,|\, v,\mathbf{k} > \\ &= \mathbf{E}\cdot\int [e^{-i(\mathbf{k}')\cdot\mathbf{r}}u^*_{c,\mathbf{k}'}(\mathbf{r})]\, e^{i\mathbf{q}\cdot\mathbf{r}}\, \frac{\hbar}{i}\nabla\, [e^{i\mathbf{k}\cdot\mathbf{r}}u_{v,\mathbf{k}}(\mathbf{r})] d^3\mathbf{r} \\ &= \left\{ \underbrace{\mathbf{E}\cdot < u_{c,\mathbf{k}+\mathbf{q}} \,|\, \frac{\hbar}{i}\nabla \,|\, u_{v,\mathbf{k}} >}_{Dipole-allowed} + \underbrace{(\mathbf{E}\cdot\hbar\mathbf{k}) < u_{c,\mathbf{k}+\mathbf{q}} \,|\, u_{v,\mathbf{k}} >}_{Dipole-forbidden} \right\} \delta(\mathbf{k}'-\mathbf{k}-\mathbf{q}) \end{aligned} \qquad (1.2.5)$$

Here $\mathbf{E}$ is the electric field vector of a linearly polarized incident light, the Bloch states are represented as $|\, n,\mathbf{k} >$ where *n* represents band index (*c* for conduction band, *v* for valence band) and $\mathbf{k}$ is the crystal momentum. In the last line, the delta function requires momentum conservation, which is the reason for strong optical transition at the direct gap, not indirect gaps. The real space representation of a Bloch wavefunction is $< \mathbf{r} \,|\, n,\mathbf{k} >= u_{n\mathbf{k}}(\mathbf{r})e^{i\mathbf{k}\cdot\mathbf{r}}$ where $u_{n\mathbf{k}}(\mathbf{r})$ is a periodic function and is constructed by atomic orbital functions [14]. The wavevector of the incident light

is denoted as **q**, which is much smaller than **k** in most far field experimental conditions, so starting from here it may be treated as zero leading to **k'= k** . In the above equation the first term is the electric dipole allowed transition. Due to the orthogonality of atomic orbital combination functions, the first dipole-allowed term is typically orders of magnitude stronger than the second dipole-disallowed term. In this thesis, monolayer TMDs and multilayer hybrid silver benzeneselenolate are studied, both of which are direct gap semiconductors [2] [23]. The first discovery of the directness of band gap in monolayer MoS_2 is evidenced by the emergence of strong photoluminescence (PL) showing the clear PL intensity contrast and energy evolution between monolayer and few layer MoS_2 [2].

A major job for optical spectroscopy experimentalists is the assignment of spectral peaks based on qualitative estimation of matrix elements: is a certain transition allowed or forbidden? is it expected to be strong or weak? Resonant peak features in spectroscopy experiments are governed by selection rules such as parity and angular momentum selection rules.

First, as a result of parity conservation, the matrix element needs to be conserved under parity transformation. Since the momentum operator has odd parity, it would require the initial state $|v,\mathbf{k}>$ and final state $|c,\mathbf{k}>$ to have opposite parities. The electric dipole transitions are controlled by the parity selection rule as mentioned above. For monolayer TMDs, the crystal lattice has broken inversion symmetry and parity is actually not a good quantum number for the Bloch states. As a result, at the single particle level, optical transitions will not be forbidden by parity conservation. For the case of silver benzeneselenolate, the crystal lattice has a preserved inversion symmetry according to current knowledge. The direct band gap is at the zone center **Γ** point, where electron wavefunction at the conduction band minimum (CBM) is dominated by Ag 5s and the valence band maximum (VBM) is a hybridization of Ag 4d and Se 3p orbitals. The parity selection rule should be imposed and the VBM to CBM transition can be determined to be allowed, giving rise to the strong optical transitions observed in our experiments, such as high photoluminescence quantum yield, large radiation rates, etc. The parity selection rules will be further modified when exciton effects are considered. In addition, as discussed in later chapters, our two-photon photoluminescence excitation (PLE) spectroscopy experiments will show that the *net* parity of the underlying Bloch states and the exciton's envelop wavefunction will give rise to distinct bright and dark exciton states in the quantum confined system [24] [23].

Second, as a result of angular momentum conservation, for crystals with rotational symmetry, such as the three fold rotation symmetry in monolayer TMD lattices, total angular momentum of the final state (J_c) needs to be a result of total angular momentum coupling of the initial state (J_v) and the momentum operator (J_p=1), i.e., J_c = J_v-1, J_v, or J_v+1. The magnetic quantum number needs to be conserved, giving $m_c = m_v$-1 or m_v+1 for photons with right or left circular polarization. The selective coupling of photon angular momentum and orbital angular momentum of electron states are the origin of circular dichroism in monolayer TMDs. Moreover, for photons vertically polarized to a 2D system $m_c = m_v$ is expected. In a system with strong spin orbital coupling, the total in spin-orbital coupled angular momentum should be considered. This results in the brightening of dark excitons in monolayer WSe_2 and WS_2 under optical excitation polarized out of plane [25].

In this dissertation, two families of materials are studied: atomically thin TMDs and multilayered hybrid metal organic chalcogenolates. The latter one involves a very complex multi-atom unit cell, and is still under numerical study with density functional theories [23]. Monolayer

TMDs have relatively simple crystal structure and analytical tight binding models have been developed to describe low energy carrier properties. The electronic states around the CBM and the VBM in K and K' valleys mainly take contributions from d orbitals of the transition metal atom and the linear combination is given as [8]

$$
\begin{aligned}
&|\phi_c>=|d_{z^2}> \\
&|\phi_v>=\frac{1}{\sqrt{2}}(|d_{x^2-y^2}>\pm i|d_{xy}>) \qquad (1.2.6)
\end{aligned}
$$

This specific combination of atomic orbitals are derived from numerical density functional calculations and adapted based on the D_{3h} symmetry of the crystal lattice. By careful inspection of the wavefunctions above in real space representations, it can be found that $\phi_{c,\mathbf{k}}(\mathbf{r})$ has orbital angular momentum of +- 1 for K and K' valleys, while $\phi_{v,\mathbf{k}}(\mathbf{r})$ has orbital angular momentum of 0 for both valleys. Note that the derivation of orbital angular momentum needs to consider two factors: rotational symmetry of the atomic d orbitals, and phase winding of Bloch states under $\widehat{C}_3$ rotations [9]. The differences of orbital angular momentum in K and K' valleys lead to the circular dichroism effect in these monolayer TMDs: the K and K' (or –K valley in some literatures) valleys can only be excited by $\sigma+$ and $\sigma-$ circularly-polarized photons, respectively. The valley-coupled circular dichroism effects are promising for optical control of spintronic and valleytronic devices. These results are for linear optical transitions. In Chapter 4, we report our experimental results regarding helicity selection rules in nonlinear sum frequency generation processes.

Since the materials studied in this thesis are in two-dimensional (2D) form, or bulk form with internal 2D stratification, it would be of great interest to introduce how dimensionality effects optical absorption in this context. As shown by Eq. (1.2.4), the spectral shape of optical absorbance is determined by the joint density of states $J_{vc}(\omega)$, since the transition matrix element $\mathbf{M}_{vc}$ typically has a very slow dependence on **k** at energies close to band gap. The joint density of states can be understood as the number of available pairs of $|c,\mathbf{k}>$ and $|v,\mathbf{k}>$ to fulfill energy conservation requirements for transitions with photon energy of $\hbar\omega$:

$$
\begin{aligned}
J_{vc}(\omega) &= \sum_{\mathbf{k}} \delta[E_c(\mathbf{k})-E_v(\mathbf{k})-\hbar\omega] \\
&= \frac{2}{(2\pi)^3}\int_S \frac{1}{\nabla_{\mathbf{k}}(E_c(\mathbf{k})-E_v(\mathbf{k}))} \qquad (1.2.7)
\end{aligned}
$$

It can be readily seen that strong absorption features are expected at momentum space positions where the conduction band and the valence band become parallel to each other, such as the direct band edges and van Hove singularities (the so-called C excitons) in monolayer MoS_2 and WS_2 [26] [4]. Moreover, for electron systems confined within different number of dimensionalities, $J_{vc}(\omega)$ shows distinctive spectral features at the onset of direct band gap [27] [14], as a result of integration in momentum space of different dimensions. Close to direct band gap, if only one pair of sub-bands are considered, the joint density of states $J_{vc}(\omega)$ in 3D, 2D, and 1D can be expressed as Equation (1.2.8) [27]. Note that in this single particle picture, the onset of direct band gap in 2D semiconductors is expected to manifest as a constant step function in linear absorption spectra.

$$J_{vc}(\omega) \sim \begin{cases} (\hbar w - E_g)^{1/2} & for\ 3D \\ Const. & for\ 2D \\ (\hbar w - E_g)^{-1/2} & for\ 1D \end{cases} \qquad (1.2.8)$$

1.3 Tightly bound Wannier excitons

Optical properties of atomically thin TMDs and the multilayered hybrid metal organic chacolgenolates are all dominated by excitons – a quasiparticle resulting from the strong many-body interaction within electron-hole pairs. Although the single particle picture introduced in the previous section can provide satisfactory explanations to many interesting optical effects in 2D semiconductors, a comprehensive and quantitative understanding of optical properties would require a many-body treatment.

Origin of the strong interaction, as well as its tunability via carrier renormalization effects, can be qualitatively understood in a simple jellium model of a homogeneous interacting electron gas. The interaction parameter r_s is defined as the averaged electron-electron distance in units of Bohr radius. In a 2D system it can be expressed as [14]:

$$r_s^{2D} = \frac{m_e e^2 g}{2\varepsilon_{eff}\hbar^2\sqrt{\pi n}} \sim \frac{< E_P >}{< E_K >} \qquad (1.3.1)$$

Here m_e is the effective electron band mass, g is the band degeneracy factor, n is 2D electron density, and ε_{eff} is the effective dielectric constant. Moreover, $< E_P >$ and $< E_K >$ are the average potential energy and kinetic energy per electron in the system. Therefore, the interaction parameter r_s is a direct estimation of the strength of many body interaction and how strongly it affects electron dynamics. For typical bulk materials, r_s is on the order of 1~5 [14]. For monolayer TMDs, it has been estimated to be as large as about 60 when electron concentration is on the order of 10^{11} cm^{-2} [21]. In this dissertation, we first report the exciton dominated optical properties of the multilayered silver benzeneselenolate. We estimate the interaction parameter r_s for the new system to be ~100 at the same electron concentration, using the averaged effective band mass of 1.13 m_0 and 0.44 m_0 as calculated from density functional theory along the two principle in-plane directions at the conduction band edge, and approximating the effective dielectric constant with the dielectric constant of benzene. The multilayer structure may introduce dielectric image-charge effects which could justify using a different ε_{eff}. However, the above estimation of the order of magnitude of r_s could explain the strong excitonic effects in silver benzeneselenolate similar to that in monolayer TMDs.

The interaction parameter also sheds light on how many body interactions can provide tunable optoelectronic properties. It's well-known that semiconductors' electronic and optical properties can be modulated by control of doping concentration. In conventional semiconductors, this is mostly due to the fact that more carriers are present to transport charges and jump between valence and conduction bands. In 2D semiconductors with strong many body effects, the carrier-induced modulation of electronic and optical properties has a more fundamental origin: the so-called renormalization effects. It's evident from Equation (1.3.1) how carrier concentration n can

significantly affect many body effects. The importance of many body interaction in electron dynamics can be roughly estimated by the ratio between average potential energy per electron $< E_P >$ and average kinetic energy per electron $< E_K >$, which is the interaction parameter r_s as shown for 2D electron gas in Equation (1.3.1). When r_s is small, electron dynamics is dominated by their individual kinetic energy; when r_s is large, electron dynamics become dominated by their potential energy which is exerted by other electrons in the whole system. When electron concentration n is increased, kinetic energy grows faster than potential energy, which is a fundamental fact of electronic systems within a parabolic band. Therefore, by reducing/increasing carrier concentration, the importance of the role that many body interaction plays in electron dynamics can be greatly enhanced/suppressed. In addition, a second contribution to carrier-renormalization comes from carrier dependence of the effective dielectric constant ε_{eff}. Coulomb interactions will be more strongly screened with a higher carrier concentration due to the response of free carriers [28]. In typical experimental conditions, electrostatic gating and optical ultrafast pumping methods can easily tune carrier concentration across two-to-three orders of magnitude. When tuned close to the charge neutrality point, the exciton effects will be greatly enhanced as evident from increased oscillator strengths and exciton binding energy. The carrier-induced renormalization effects have been experimentally demonstrated by pump-probe experiments [29] and steady state PLE experiments on back-gated monolayers [19], which will be discussed in more detail in later sections.

From here we start the introduction of how exciton effects can strongly reshape optical transitions in 2D semiconductors. On exciton resonance, the strongly coherent superposition of single particle states leads to greatly enhanced linear and nonlinear optical cross sections, which are beneficial for many applications. In addition, exciton wavefunctions are reshaped by the envelope wavefunction describing how the electron circulates around the hole. The exciton wavefunction has distinct parity and angular momentum which would bring additional ingredients into optical selection rules.

Excitons are typically categorized into two types: Wannier excitons and Frenkel excitons. For Wannier excitons, the electron-hole spatial separation is large compared with the lattice constant, and the k-space distribution of the exciton wavefunction is relatively localized. In most cases the excitons formed by carriers at the direct band gap of a semiconductor are Wannier type. As a comparison, Frenkel excitons are highly localized in real space, and most commonly seen in single molecules. The excitons in monolayer semiconductors are believed to be of Wannier type, as shown by the calculated wavefunction of monolayer MoS_2 in [13].

From here we provide a brief description of Wannier excitons in a many-body picture. The focus is on showing important results and discussing their physical picture, while more detailed derivations can be found in [14]. Exciton states $|\Psi_{ex}>$ in a semiconductor lattice can be constructed as a superposition of electron-hole pair states $|\phi_{\mathbf{k},\mathbf{k}_{ex}}>$ in momentum space.

$$|\Psi_{ex}>=\sum_{\mathbf{k}} A(\mathbf{k})\,|\phi_{\mathbf{k},\mathbf{k}_{ex}}> \qquad (1.3.2)$$

$$|\phi_{\mathbf{k},\mathbf{k}_{ex}}>=c^{\dagger}_{c,\mathbf{k}+\mathbf{k}_{ex}}c_{v,\mathbf{k}}\,|0> \qquad (1.3.3)$$

Here k_{ex} is the exciton momentum and also the momentum the excitation photon. The ground state $|0>$ In Eq (1.3.3) should be approximated as a Slater determinate involving all single particle electron Bloch states in the valence band. From the ground state, the electron-hole pair states $|\phi_{\mathbf{k},\mathbf{k}_{ex}}>$ are obtained by annihilating one Bloch electron state in the valence band ($c_{v,\mathbf{k}}$) and creating one Bloch electron ($c^{\dagger}_{c,\mathbf{k}+\mathbf{k}_{ex}}$) in the conduction band, as schematically represented in the left graph of **Figure 1.3.1**. These electron-hole pair states serve as the many-body basis states for constructing the exciton states $|\Psi_{ex}>$. The $A(\mathbf{k})$ in Eq. (1.3.2) is the distribution of exciton states in momentum space, which is often used to show the contribution from Bloch states at different positions in Brillouin zone [13] [24]. It would be intuitively very convenient to define the real-space exciton envelope wavefunction $F(r)$ using $A(\mathbf{k})$ and plane waves, where $\mathbf{r}$ is the relative position between electron and hole.

$$F(\mathbf{r}) = \sum_{\mathbf{k}} A(\mathbf{k}) e^{i\mathbf{k}\cdot\mathbf{r}} \qquad (1.3.4)$$

For Wannier excitons with a Bohr radius much larger than the unit cells, this envelope function describes the envelope spatial profile of electron motion with respect to the hole, on top of the underlying electronic wavefunctions.

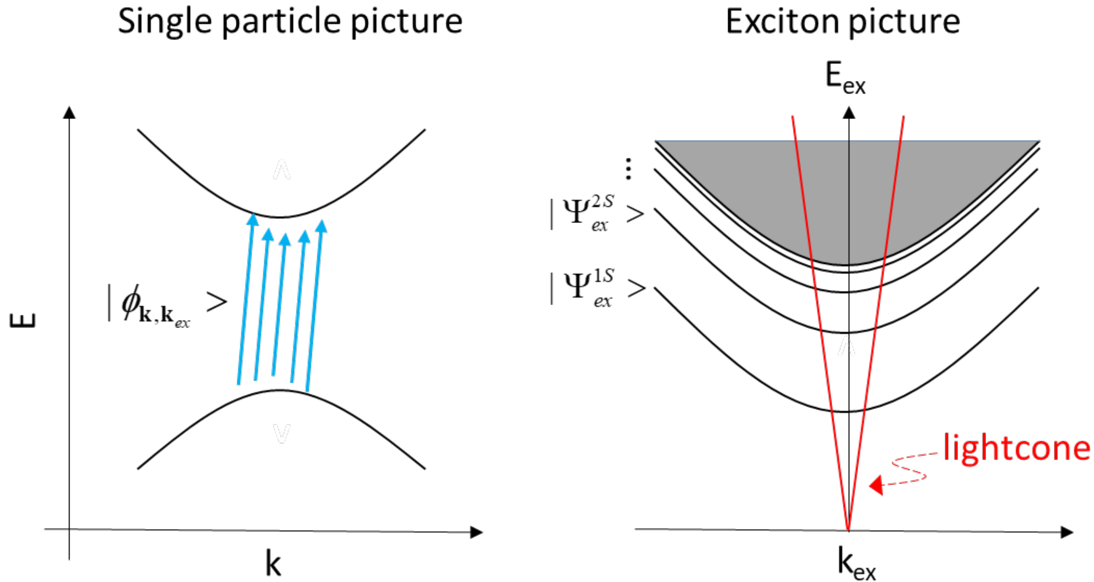

Figure 1.3.1 Illustration of exciton states in the single particle picture (left) and the exciton picture (right). In the single particle picture, the blue arrows are slightly tilted not in scale to show the effect of photon/exciton wavevector k_{ex}. In the exciton picture, the grey shaded area shows the exciton continuum, the red lines sketch the lightcone outside of which the exciton states cannot be directly coupled to far field light.

The Hamiltonian H describing the many electron system should include both the sum of single particle energy of each electron H_1, and the Coulombic interaction between each pair of electrons H_2. Note that in this picture the electron-hole Coulombic energy is manifested as the

interaction between the one excited conduction band electron and N-1 electrons left in the valence band.

$$H = H_1 + H_2$$
$$= \sum_{i=1}^{N} [\frac{\mathbf{p_i^2}}{2m_i} + V(\mathbf{r_i})] \; + \; \frac{1}{2}\sum_{i \neq j} \frac{e^2}{\varepsilon_{eff} r_{ij}} \qquad (1.3.5)$$

Now the eigenenergies E_{ex} and full exciton wavefunctions of the exciton states can be obtained with the basis function given in Eq (1.3.2, 1.3.3) and the Hamiltonian in (1.3.5). We can obtain the resulting effective-mass characteristic equation for exciton binding energy E_{ex} and envelope wavefunction $F(\mathbf{r})$.

$$[E_{cv}(-i\nabla, \mathbf{k_{ex}}) - \frac{e^2}{\varepsilon_{eff}\mathbf{r}} + J_{ex}(\mathbf{k_{ex}})\delta(\mathbf{r})\delta_M]F(\mathbf{r}) = E_{ex}F(\mathbf{r}) \qquad (1.3.6)$$

The term $E_{cv}(-i\nabla, \mathbf{k_{ex}})$ includes the detailed band structure information of a specific material which is defined as $E_{cv}(-i\nabla, \mathbf{k_{ex}}) = E_c(-i\nabla + \frac{1}{2}\mathbf{k_{ex}}) - E_v(-i\nabla - \frac{1}{2}\mathbf{k_{ex}})$ .This is the energy difference between conduction and valence band Bloch electrons, as illustrated in the left panel of Figure 1.3.1. The term J_{ex} is due to exchange interaction between electron and hole and only exists for singlet exciton states with δ_M =1. The exchange term is typically negligible because of the large spatial extent of Wannier excitons.

Close to the direct band edge, the band structure $E_{cv}(-i\nabla, \mathbf{k_{ex}})$ can be approximated by an isotropic 2D parabolic band, resulting in the 2D exciton binding energy as:

$$E_{ex}^{2D}(n) = -\frac{\mu e^4}{2\hbar^2 \varepsilon_{eff}(n)^2 (n - \frac{1}{2})^2} \qquad (1.3.7)$$

Note that although the expression looks similar to a 2D hydrogen model, the effective dielectric constant $\varepsilon_{eff}(n)$ has been experimentally shown to be dependent on the principal quantum number, resulting in a large deviation from the 2D hydrogen series [30]. The effective dielectric constant ε_{eff} is significantly reduced from the value of the bulk material where electron and hole resides. As shown by [30], in a 2D system a large portion of electric field lines extend out of the 2D layer into the surrounding medium (such as air) which has much less screening, while in a 3D system the Coulomb interaction is completely screened by the bulk host material. The reduced screening is major origin for strong excitonic effects in lower dimensions.

The optical dielectric function in the excitonic picture can be obtained by evaluating the dipole transition matrix with the many-body exciton states. The resulting linear excitonic susceptibility can be expressed as the Elliot formula [31] [14]:

$$\chi(\omega) = 2|\mathbf{M}_{cv}|^2 \sum_{\lambda} \frac{|\Psi_\lambda(\mathbf{r}=0)|^2}{E_\lambda - \hbar\omega - i\Gamma_\lambda} \qquad (1.3.8)$$

Here $\Psi_\lambda(\mathbf{r})$ is the wavefunction of exciton state λ expressed in coordinate of relative electron-hole position, i.e., $\mathbf{r}=\mathbf{r}_e-\mathbf{r}_h$. It can be seen that the linear optical absorption is only allowed for exciton states with nonzero amplitude at $\mathbf{r}=0$, which comes from a similar parity selection rule as in the single particle picture. The full exciton wavefunction $\Psi_{ex}(\mathbf{r_e},\mathbf{r_h})$ which can also be obtained as:

$$\Psi_{ex}(\mathbf{r_e},\mathbf{r_h}) = \sum_{\mathbf{R_1},\mathbf{R_2}} F(\mathbf{R_1}-\mathbf{R_2})W_c(\mathbf{r_e}-\mathbf{R_1})W_v(\mathbf{r}_h-\mathbf{R}_2) \qquad (1.3.9)$$

Here W_c and W_v are the standard Wannier functions of conduction and valence band electrons around the $\mathbf{R_1}$ and $\mathbf{R_2}$ lattice points. In this expression, note that the effect of exciton wavevector $\mathbf{k_{ex}}$ is not directly manifested, but buried in the interference between the electrons and hole Wannier functions. As evident from Eq. (1.3.9), parity of the exciton states should be the net symmetry of exciton envelope wavefunction $F(\mathbf{r})$ and the Wannier functions of the underlying electronic Bloch states W_c and W_v giving $\pi(\Psi_{ex}) = \pi(F)*\pi(W_c)*\pi(W_v)$. Therefore the envelope function will significantly modify parity-based selection rules. At the direct band gap, the s-type exciton with even spatial symmetry will still be a dipole-allowed transition from the ground state, but the transition to a p-type exciton with odd spatial symmetry will be dipole-forbidden. This has been experimentally studied for monolayer TMDs [24] before and this thesis includes our investigation on multilayered hybrid silver benzeneselenolate. In order to fully describe the optical selection rules for exciton transitions, a symmetry analysis incorporating crystal structure, electronic states, exciton envelope function, as well as light polarization should be performed.

1.4 Nonlinear optics with atomically thin semiconductors

Atomically thin semiconductors and van der Waals heterostructures hold great promise for nonlinear optical applications. In monolayer (1L) and few layer TMDs, strong excitonic effects and broken inversion symmetry result in resonantly enhanced nonlinear responses such as second harmonic generation [15], two photon photoluminescence [24], saturable absorption [32], and high harmonic generation [33]. The van der Waals interaction between neighboring layers also allows facile integration of two-dimensional (2D) TMDs with nanophotonic devices such as photonic crystal and microdisk cavities where the nonlinear light-matter interaction can be further enhanced [34] [35]. Moreover, the resonance energies and oscillator strengths of exciton states in monolayer TMDs are very sensitive to carrier concentration, which can be conveniently controlled by electrostatic gating [5] [22] [19], providing new solutions to electrically tunable nonlinear susceptibilities [18]. In addition, many nonlinear optical techniques are also crucial for the development and characterization of 2D semiconductor materials and twisted heterostructures, such as the determination of crystal orientation with second harmonic generation (SHG) [36] [37] [38], probing excitonic dark states and measuring exciton binding energies with two-photon photoluminescence excitation spectroscopy [24] [23], imaging edge states and grain boundaries [39], etc.

The major nonlinear optical processes studied in this dissertation are sum frequency generation (SFG), second harmonic generation (SHG), and two-photon photoluminescence (TPPL) from monolayer and twisted bilayer TMDs as well as multi-layered silver benzeneselenolate.

The study of SHG and SFG are important for practical nonlinear applications of 2D semiconductors, in devices such as laser frequency converters, optical parametric amplifiers and oscillators, and spontaneous down conversion for generating quantum entangled photons. The second order nonlinear responses also play important roles in the determination of crystal structure and spectroscopy-based interface-sensitive sensing applications, since inversion symmetry breaking is required. Both SHG and SFG are governed by the second order nonlinear susceptibility $\chi^{(2)}$ as described in **Eq. (1.2.1)**. Since SHG is a special case of SFG, here we focus on discussion of the more general SFG process in a monolayer TMD lattice.

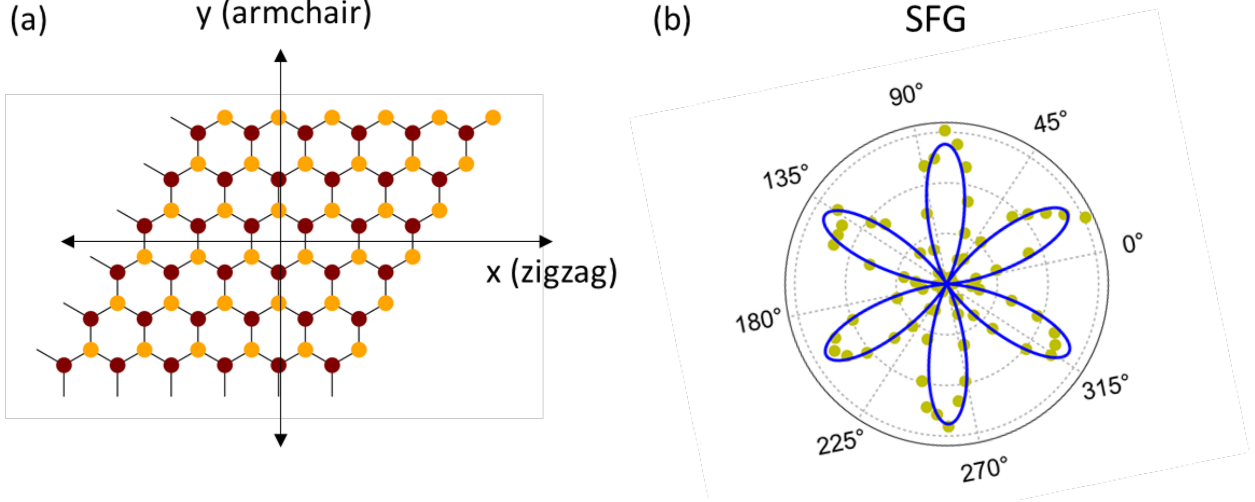

Figure 1.4.1 (a) Schematic of top view of crystal structure of monolayer TMD, with red (orange) representing the transition metal atom (the pair of chalcogenide atoms). (b) Intensity of sum frequency generation (SFG) as a function of laser excitation polarization angle when collection polarization is parallel to excitation.

The space group of a monolayer and other odd layers of TMD or hexagonal boron nitride (hBN) lattice is D_{3h}, which lacks inversion symmetry, and therefore has the following non-vanishing elements of the $\chi^{(2)}$ tensor [40].

$$|\chi^{(2)}| = \chi_{yyy} = -\chi_{yxx} = -\chi_{xxy} = -\chi_{xyx} \qquad (1.4.1)$$

For a generic D_{3h} crystal system, the y direction in Eq. (1.4.1) refers to the mirror plane direction as shown by Figure 1.4.1. In the case of TMDs, this is the armchair direction. Therefore, by measuring second order nonlinear signal such as SHG or SFG as a function of polarization direction, the crystal orientation can be determined.

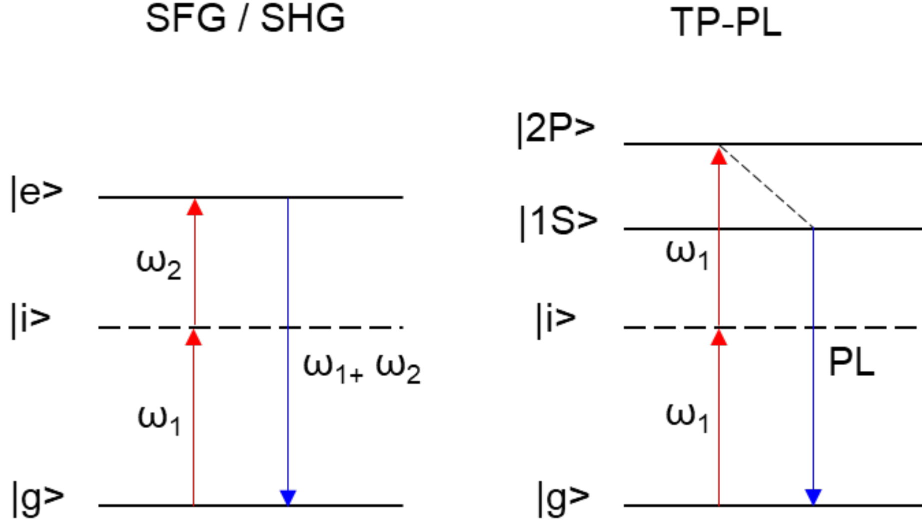

Figure 1.4.2 Schematic level diagram of (left) the sum frequency generation (SFG) process, which is a more generalized case of second harmonic generation (SHG), and (right) two photon photoluminescence (TP-PL).

One part of this thesis is to explore the exciton resonance enhancement and helicity selection rules of second order nonlinear processes. As shown by Figure 1.4.2, the SFG process involves three transitions. First, one photon with energy of $\hbar\omega_1$ is absorbed to bring the system from ground state $|g>$ to an intermediate state $|i>$ which is a virtual state in most cases. Then a second photon with energy of $\hbar\omega_2$ is absorbed to bring the system from the intermediate state to the excited state $|e>$. Finally, one photon with the energy of $\hbar\omega_S = \hbar\omega_1 + \hbar\omega_2$ is scattered/emitted and the system goes back to the ground state $|g>$. The net transition is a triple resonant process, which can be described by the product of three transition matrix elements [40].

$$\chi_{ijk}^{(2)}(\omega = \omega_1 + \omega_2) \sim \sum_{|i>} \left\{ \frac{\mathbf{p}_i^{g,e}\mathbf{p}_j^{e,i}\mathbf{p}_k^{i,g}}{(\omega - \omega_e + i\Gamma_e)(\omega_1 - \omega_i + i\Gamma_i)} + \frac{\mathbf{p}_i^{g,e}\mathbf{p}_k^{e,i}\mathbf{p}_j^{i,g}}{(\omega - \omega_e + i\Gamma_e)(\omega_2 - \omega_i + i\Gamma_i)} \right\} \quad (1.4.2)$$

where $\mathbf{p}_k^{i,g}$ is the electric dipole transition matrix element from $|g>$ to $|i>$ with the polarization k, Γ_e (Γ_i) and ω_e (ω_i) are relaxation rates and resonance frequencies for the excited state (intermediate states). The transition rate is expected to be greatly enhanced when at least one of the three respective photon energies matches with allowed optical transitions. The SHG response of monolayer WSe_2 has been measured as a function of excitation energy [15], showing great enhancement when twice the excitation energy matches both s-type bright excitons and p-type dark exciton states. When twice the excitation photon energy matches the s-type exciton states, the enhancement mainly arises from the second harmonic emission resonance, which is a strong dipole allowed transition. When twice the excitation photon energy matches the p-type exciton states, the enhancement mainly arises from the successive two-photon excitation process, which is also dipole allowed. It's proposed that in both cases, two electric dipole transitions and one magnetic dipole transitions are involved. For SHG experiments it's difficult to directly show whether a certain process is enhanced by excitation resonance or emission resonance, because the two excitation photon energies are identical. In the SFG experiments described in Chapter 4 of this dissertation,

by separately varying the two excitation photon energies, more insights into the emission and excitation resonance of a second order process can be obtained.

Two-photon photoluminescence can probe the unique p-type excitonic dark states, which are dipole-forbidden for one photon transitions. In this dissertation, a two-photon photoluminescence excitation (TP-PLE) technique is employed to probe p-type dark states in silver benzeneselenolate, providing important support for the quantification of exciton binding energy. In a TP-PLE experiment, a femtosecond pulsed laser is used to excite the sample providing large instantaneous population of the intermediate states as shown by Figure. 1.4.2. These intermediate states are virtual states with fast relaxation, so only with a high instantaneous pump pulse can they be further excited to the excited 2P states. Both of the transitions from ground state to the intermediate state, and from intermediate state to the 2P excitonic dark state are electric-dipole allowed. However, the direct transition from ground state to the 2P excitonic state is dipole forbidden, because the envelope exciton wavefunction of 2P states have an odd spatial symmetry, owing to a vanished amplitude at zero relative position of electron and hole. This is also evident from the Elliot formula shown in Equation (1.3.8) showing that the linear polarizability contributed by exciton state λ is proportional to $|\Psi_{\lambda}(\mathbf{r}=0)|^2$. Therefore, two photon PLE can provide crucial information of the excited states and binding energies of a Wannier exciton system.

Chapter 2 – Carrier induced renormalization of quasiparticle band gap and exciton binding energies in monolayer MoS_2

2.1 Introduction

Monolayer transition metal dichalcogenide (ML-TMDC) semiconductors are exquisite optoelectronic materials that synergize the effects of strong confinement [2] [3] [4], intense many-body interactions [21] [41] [42] and spin-coupled valley degrees of freedom [43] in a robust, atomically-thin semiconductor with extended two-dimensional (2D) crystalline order. In ML-TMDCs, electronic excitations are collective phenomena that are described by a quasiparticle band structure which condenses the excitations into particles with momentum and energy that reflect the underlying many-body physics and crystal structure [44, 45]. The energetic separation between the quasiparticle valence and conduction bands, termed the 'quasiparticle band gap', governs the electronic properties in ML-TMDCs such as transport, formation of Ohmic contacts and band alignment in heterostructures [46] [47] [48] [49] [50]. Meanwhile, photoexcitations, which are essential to optoelectronic functionality [6] [7] [17] [51] [52], create electron-hole pairs within the quasiparticle band structure, forming a rich manifold of bound exciton states. The lowest-energy exciton – a strong dipole transition in these materials – determines the 'optical band gap' (i.e., the energetic threshold of optical absorption), which is energetically smaller than the quasiparticle band gap because of the electron-hole binding energy [53] [54] [55]. Strong physical and dielectric confinement make Coulombic interactions central to determining these quasiparticle and optical bandgaps, and an incredibly compelling aspect of ML-TMDCs is the ease by which the strength of this interaction can be manipulated, providing an unprecedented tunability of the quasiparticle and exciton energies [28] [29] [22] [5] [56].

In this letter, we experimentally disentangle and quantify the carrier-induced renormalization of both quasiparticle and optical band gaps in ML-MoS_2, providing a unified picture of these rich and complex effects in two-dimensional semiconductors. This quantification is enabled by the direct, all-optical identification of the carrier-density-dependent quasiparticle band gap using photoluminescence excitation (PLE) spectroscopy combined with steady state electrostatic gating to control the strength of the Coulombic interactions in the ML-MoS_2. Importantly, renormalization effects on the quasiparticle band gap and exciton binding energy tend to counteract each other, leading to only minimal changes in the optical band gap [57]. Thus, in conventional optical absorption spectroscopy, without direct identification of the quasiparticle band gap, quasiparticle and excitonic renormalization effects must be inferred from higher-lying excitonic states [22] [56, 58] [59]. Central to our approach, we demonstrate that the relative photoluminescence from defect-bound excitons (DXs) [60] [61] diminishes with increased carrier doping and can identify the onset of photoexcitation of free carriers at the quasiparticle band gap. When combined with ground-state absorption and PLE spectroscopy, we can (1) track carrier-induced renormalization of the quasiparticle band gap and (2) fully deconvolve excitonic and quasiparticle renormalization effects. For both effects, we find renormalization of more than 150 meV over a moderate range of doping concentrations, agreeing remarkably well with previous theoretical predictions [28]. Further, we observe that at low doping levels the band gap and exciton binding energy can be larger than 2.7 eV and 800 meV, respectively.

2.2 Identification of quasiparticle band gap from photoluminescence excitation spectroscopy

Figure 2.1(a) shows a schematic of the PLE spectroscopy of back-gated ML-MoS_2 that reports the excitation dependent photoluminescence as a function of free carrier density (MoS_2 grown on 285 nm SiO_2 on Si [62]). Complete experimental details are provided in the Supplemental Material [34], but we note that all measurements were performed at 80 K where radiative recombination from the DX states is activated [60]. At unbiased gating, ML-MoS_2 flakes were found to be heavily n-doped with a residual carrier concentration of 8.7×10^{12} cm^{-2}, which likely results from interactions with the underlying substrate [59] [63]. Figure 2.1(b) shows the gate dependence of the relative intensities of the ground state excitonic emission at ~1.86 eV (A exciton) and of the DX states at ~1.72 eV. At an unbiased gate voltage (e.g., Vg=0 V), the PL of our samples is dominated by the trion. Upon reducing the free carriers with increasingly negative gate voltages, the lower-energy emission from the DXs emerge: decreasing the concentration of free carriers increases the relative PL yield of the DX states with respect to the A excitonic emission. To quantify this effect, we estimate the relative yield of the DX emission by comparing the relative amount of emission below 1.80 eV with respect to the total emission (inset, Fig. 2.1(b)).

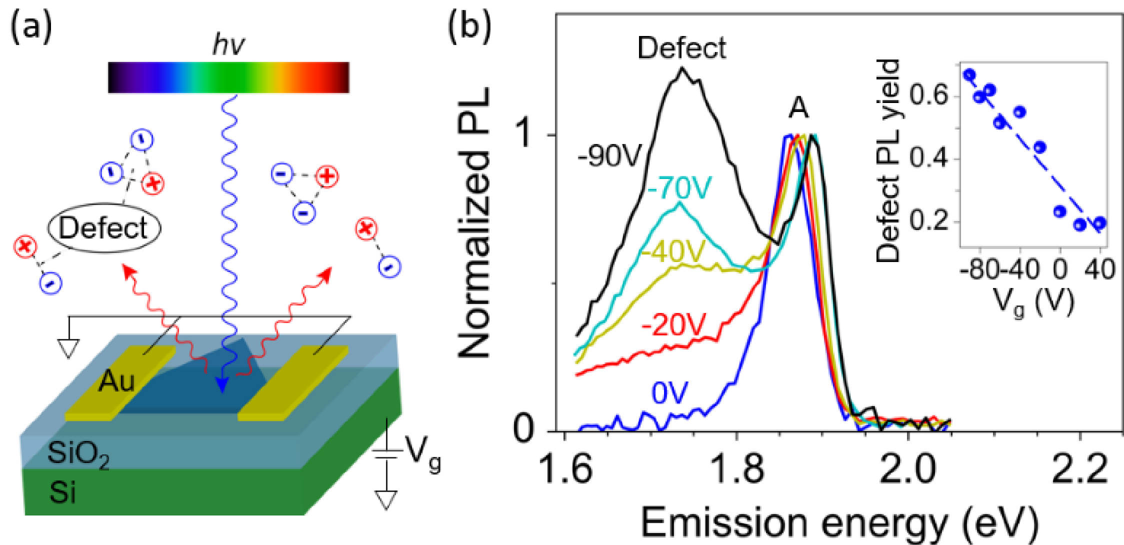

Figure 2.1. (a) Schematic of gate dependent photoluminescence excitation (PLE) spectroscopy on monolayer MoS_2. (b) Normalized PL spectra measured under different gate voltages with 2.5eV excitation. Inset shows the dependence of defect PL yield as a function of gate voltage.

The precise relaxation dynamics that govern the balance of excitonic and DX emission are still not yet fully understood [60] [61]. We speculate that the reduction in the relative yield of the DX emission with increasing carrier density is a combination of increased defect screening and state filling by the free carriers. A similar trend was also noted in ML-WSe_2 [22]. Regardless of the exact mechanism, it is clear that the relative yield of the DX emission depends on the concentration of free carriers, providing a spectroscopic route to detect the photoexcitation of free carriers.

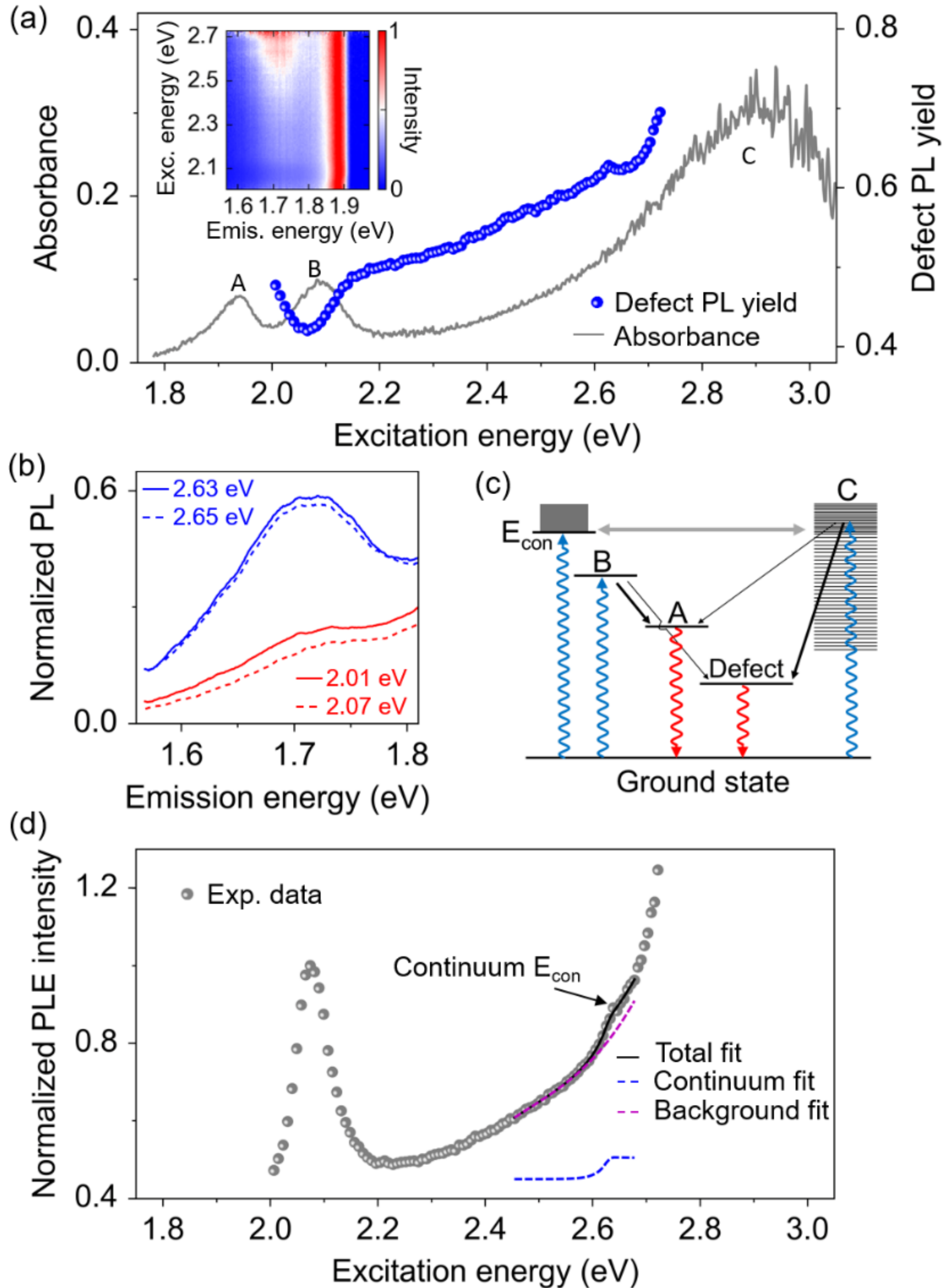

Figure 2.2. Identification of the quasiparticle band gap in monolayer MoS_2 from PLE spectroscopy. (a) Dependence of the yield of defect PL on excitation energy (blue dots), overlaid on the absorption spectrum (gray, taken from samples transferred to a quartz substrate). Inset shows the color contour of normalized PL spectra measured at different excitation energies. (b) Comparing the defect PL spectra (normalized to the A exciton; full spectra are shown in section 2.5) under excitation energies that are on and off resonance of the continuum edge and B exciton. (c)

Schematic level diagrams showing the relevant relaxation pathways of photo-generated excitations. A complete diagram is shown in section 2.5. (d) Experimental PLE spectrum (gray dots) and total fit (black solid line) with contribution from the continuum (blue dotted line, with offset) and tail of the C exciton (magenta dotted line).

Figure 2.2 shows PLE spectroscopy of ML-MoS_2 at an intermediate carrier concentration, where emission intensities from the DXs and main A exciton states are comparable. In Fig. 2.2(a), the relative PL yield of the DX as a function of excitation energy is overlaid with the absorption spectrum, and the three prominent excitonic ‘A’, ‘B’ and ‘C’ absorption resonances are identified [2] [26]. Note first that the ratio of the DX emission to the A exciton emission generally increases with increasing excitation energy nearly in unison with the absorption from the higher-energy ‘C’ band [26] [13]. Secondly, a pronounced dip is observed at 2.07 eV, which nicely corresponds to the resonance energy of the ‘B’ exciton state. And finally, at 2.64 eV a small but pronounced decrease, deviating from the otherwise monotonic increase, is observed. Four individual PL spectra at representative energies are shown in Fig. 2.2(b) which exemplify the differences in the relative yield of DX emission.

The level diagram in Fig. 2.2(c) summarizes the absorption resonances and coupling pathways at these excitation energies in ML-MoS_2 [59] [26]. Although the C exciton is peaked at ~2.9 eV, its absorption resonance is broad, yielding a tail of closely spaced excited states that spans nearly to the optical bandgap. The narrower resonant excitations of the A and B excitons are superimposed on the C exciton at ~1.9 and ~2.1 eV, respectively. At each excitation energy, a fraction of the C excitons can relax to form A excitons [59] [26] and DX states. The generally increasing trend of the DX emission yield vs. excitation energy indicates that the relative coupling of C excitons to DXs strengthens with increasing energy. Direct excitation of B excitons, on the other hand, enhances the relative number of A excitons, presumably because this additional set of absorbing states lies in the same region of the Brillouin zone and preferentially couples to the A exciton, decreasing the relative DX yield at 2.07 eV.

For the higher energy decrease in the DX yield at 2.635 eV, which is weaker than its lower energy counterpart at ~2.07 eV, neither a strong excitonic resonance exists [59] [58] [30] [64] nor are there any corresponding features in the absorption spectrum. Yet the PLE spectrum (Fig. 2.2(d)) of the total emission intensity exhibits a step-like increase at the same energy, which is well-described as the sum of a broad increasing background (from the C exciton tail) and a broadened step function (see section 2.5 for details), similar to a feature observed in our previous work [59]. Such a step-like increase in photoexcitation is anticipated for the absorption at the band edge of non-interacting electrons in two dimensions [44] [30] [64]. In conjunction with the decrease in the DX yield, we reason that this energy marks the onset of photoexcitation of the continuum of unbound electrons and holes [64] [65] near the quasiparticle band gap at the K/K’ valleys. These unbound carriers reduce the emission yield of the DX states following the same mechanism as observed under electrostatic gating (Fig. 2.1(b)). The approximate reduction of defect PL yield at 2.64 eV is 2%. Using the linear trend fitted from Fig. 2.1(b), such a reduction corresponds to an injected carrier concentration of $3\times10^{11}cm^{-2}$ which is on the same order as the estimated number of photoexcitations produced at these energies, of ~8×10^{10} cm^{-2} (see section 2.5).

2.3 Experimental observation of carrier induced renormalization effects

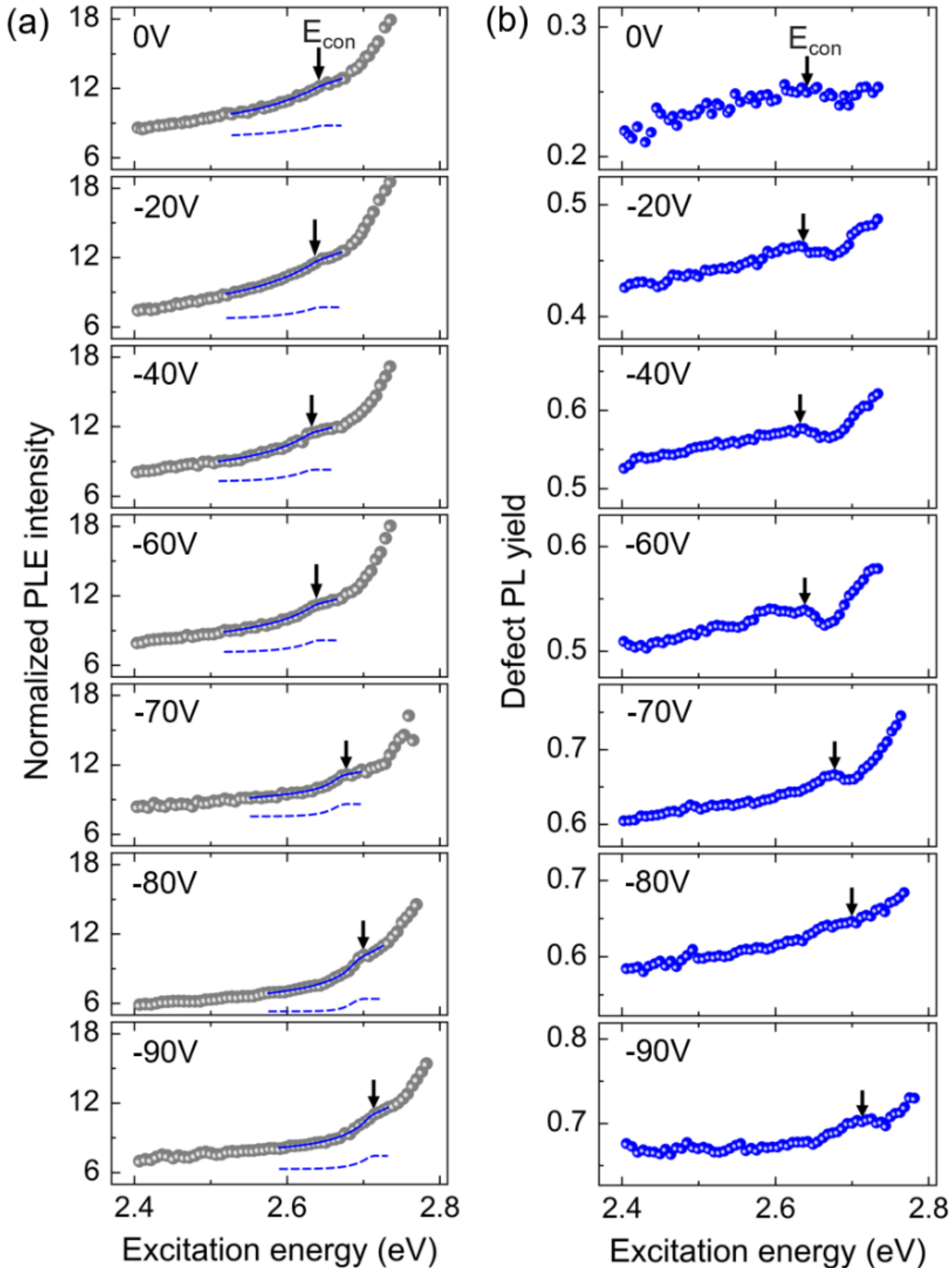

Figure 2.3. Gate dependent PLE spectroscopy of monolayer MoS_2. (a) PLE spectra of the integrated emission measured at different gate voltages. Experimental data, total fit, and the continuum contribution (with offset) are represented as gray dots, blue solid lines, and blue dashed lines, respectively. The PLE intensities are normalized to the oscillator strength (i.e., step height) of the fitted continuum function. (b) The excitation-energy dependent relative yield of defect PL

at different gate voltages. The arrows in (a) and (b) represent the same energy of E_{con} fitted from (a) as described in the text.

If our assertion is correct, the spectral signatures of direct excitation of the quasiparticle continuum in the PLE and relative DX yield should energetically shift with gate voltage as the quasiparticle band gap renormalizes [28]. Gate-dependent PLE and DX emission yield spectra are shown in Figure 2.3. At each gate voltage, the step feature in the PLE spectrum (Fig. 2.3(a)) and corresponding reduction in the relative emission yield of the DX (Fig. 2.3(b)) are observed (complete PLE data sets are shown in the section 2.5). Using the PLE spectra alone, the energetic threshold for optical excitation of the continuum of unbound quasiparticles (i.e., the "continuum", Econ) is extracted from the position of a fitted step function (as described in Fig. 2.2) and are marked by the arrows in both the PLE and the relative DX emission yield spectra. Clearly, the two spectral features exhibit nearly identical renormalization effects. Starting at the residual doping concentration, Econ first shifts to lower energies as the gate voltage decreases to -40 V and then reverses directions, shifting to higher energies as gate voltage further decreases to -90 V, which was our lowest obtainable gate voltage before dielectric breakdown. For positive gate voltages, the continuum excitation features rapidly diminish and are no longer clearly discernible possibly due to increased broadening of the continuum feature [65] and/or increased indirect optical absorption at higher carrier densities [66]. The strongly-correlated renormalization of the step feature in the PLE and the reduction in DX emission yield offer compelling evidence that these spectral features are indeed related to the quasiparticle band gap, and that their spectral shifts with gate voltage provide important insight into carrier-induced renormalization effects.

Notably, direct band-edge and excitonic transitions are expected to behave markedly differently in response to changes in carrier density [57] [65]. In Figure 2.4, the renormalization of the quasiparticle band gap is quantified and compared to previous theoretical studies. The dependence of the continuum onset energy, E_{con}, on carrier concentration is summarized in Fig. 2.4(a) where the gate voltage has been converted to the electron concentration, ne (see section 2.5). Careful distinction must now be drawn between the energetic onset of continuum excitations (E_{con}) and the quasiparticle band gap (E_g). In a doped system, Econ is larger than E_g due to Pauli blocking, as direct transitions can only occur from occupied states in the valence band to unoccupied states in the conduction band above the Fermi energy, E_F (Fig. 2.4(a), inset). Using a parabolic approximation for the band extrema, E_g is related to Econ by $E_g = E_{con} - ne\pi\hbar^2/2\mu q$, where ħ is the reduced Planck constant, q is the electron charge, and μ is the exciton reduced mass [21]. From effective masses reported in literature [13], the quasiparticle band gap (E_g) at the residual doping level ($ne = 8.7\times10^{12}cm^{-2}$) is calculated to be 2.57 ± 0.01 eV where the uncertainty reflects the variations of multiple measurements. With decreasing electron concentration, the measured quasiparticle band gap increases nonlinearly, reaching 2.70 ± 0.01 eV at the lowest carrier concentration ($ne = 1.8\times10^{12}$ cm^{-2}; Vg = -90 V) achieved in our measurements. By fitting a line to quasiparticle band gap E_g at the four lowest electron concentrations, we estimate that E_g of our samples at intrinsic doping concentrations is 2.78 ± 0.02 eV. Remarkably, the majority of the theoretical predictions of quasiparticle band gap from previous studies (Fig. 2.4(a); orange crosses) [28] [13] [67] [68] [69] are within 100 meV of our estimated value. We also note that the band gap we measured at the residual doping condition is comparable to recent photocurrent [70] and PLE [59] [58] measurements, but substantially higher than scanning tunneling microscopy (STM) measurements of ML-MoS_2 on conductive substrates [55] [71]. And further, a recent STM study

of suspended ML-MoS_2 [72] finds a gap approaching the value we determined for the zero-doping condition.

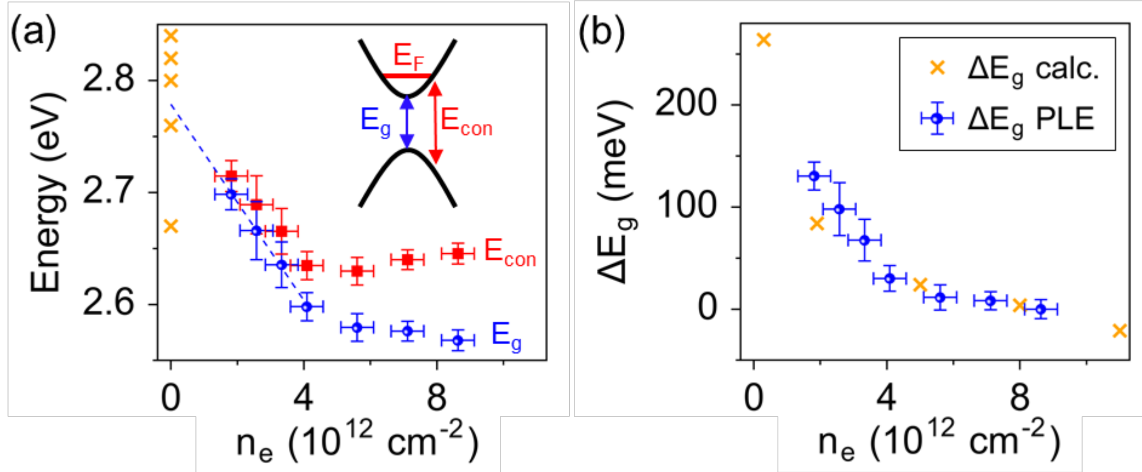

Figure 2.4. Carrier induced renormalization of the quasiparticle band gap of monolayer MoS_2. (a) Dependence on electron doping concentration n_e of the measured continuum onset energy E_{con} (red squares) and quasiparticle band gap E_g (blue dots). Predicted quasiparticle band gap energies from previous studies ([28] [13] [67] [68] [69]) are also plotted for comparison (orange crosses). (b) Direct comparison of the measured *change* of quasiparticle band gap (blue dots) to previous theoretical predictions (orange crosses, [28]).

Such a large, nonlinear renormalization of the quasiparticle band gap has previously been theoretically predicted and attributed to carrier-induced screening [28]. In Fig. 2.4(b), our experimental measurement of the quasiparticle band gap renormalization is compared to theoretical predictions [28] where ΔE_g denotes the change of the band gap from the residual doping concentration. We find that for the relative changes in the quasiparticle band gap, the experimental and theoretical results agree remarkably well. Moreover, the observed band gap renormalization of over 150 meV is more than one order of magnitude larger than any excitonic renormalization effects in ML-TMDCs [2] [5] [56], further corroborating our assignment of the observed step feature in PLE spectra to be the continuum.

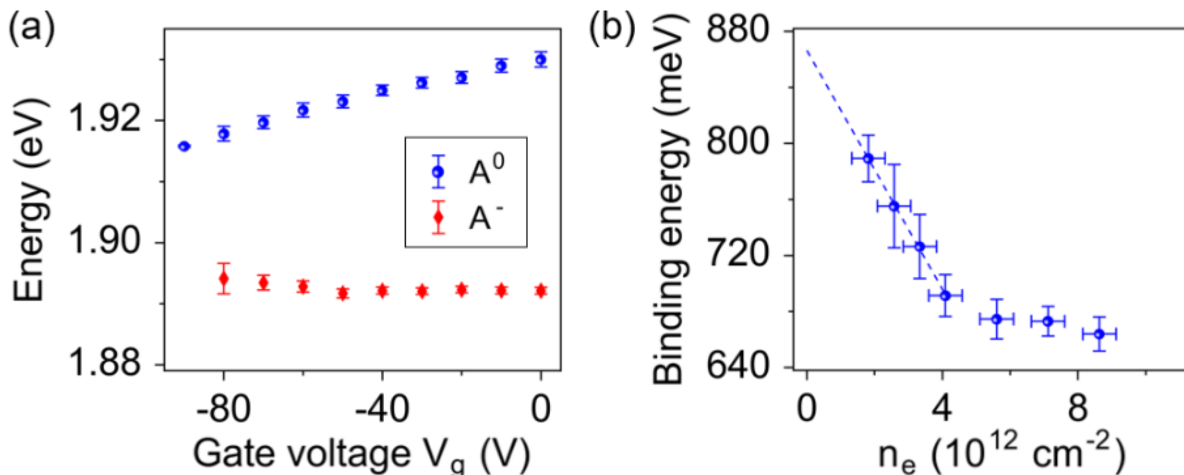

Figure 2.5. Carrier-induced renormalization of the exciton binding energy in monolayer MoS_2. (a) Dependence of the absorption energies of the neutral A exciton (blue dots) and charged A^- trion (red diamonds) on gate voltage. (b) Renormalization of the binding energy of neutral A exciton with electron concentration.

Finally, in Figure 2.5, the renormalization of the exciton binding energy is directly quantified by combining the PLE-derived values of the quasiparticle band gap and the optical band gap measured with gate-dependent absorption and PL spectra (see section 2.5). The extracted energies of the neutral A exciton (A^0) and charged A trion (A^-) states from absorption spectra are shown in Fig. 2.5(a). The corresponding carrier-dependent binding energy of A^0 can be calculated from its energetic separation from the quasiparticle band gap (Fig. 2.5(b)) and is found to be as large as 790 ± 17 meV at the lowest measured electron concentration. Extrapolating to lower concentrations, we estimate that the exciton binding energy at the zero-doping condition is 866 ± 31 meV, which is comparable to what is predicted by GW-BSE calculations [13] [68]. As the electron concentration is increased, the exciton binding energy rapidly decreases to 690±15 meV at an electron concentration of $\sim 4.0\times10^{12}$ cm^{-2} and then more gradually decreases to 660±12 meV at the residual doping condition. This nonlinear behavior likely arises from the combined effects of increased Coulombic screening and phase space filling [73]. Notably, the carrier dependence of the exciton binding energy (Fig. 2.5(b)) follows that of the quasiparticle band gap (Fig. 2.4(a)), experimentally demonstrating how the two renormalizations counteract each other, resulting in comparatively modest changes in the ground-state optical transitions [57].

2.4 Conclusion

In conclusion, using the suppression of defect emission by free carriers in combination with PLE, PL and absorption spectroscopies, we have directly quantified carrier-induced quasiparticle and excitonic renormalization effects in gated ML-MoS_2 devices. At the lowest achieved doping level, the quasiparticle band gap is determined to be 2.70 ± 0.01 eV leading to a binding energy for the A exciton of 790 ± 17 meV. Both the quasiparticle band gap and binding energy renormalize by nonlinearly decreasing by over 150 meV as the electron concentration is increased to the residual doping level. Notably, our experimental results agree very well with previous theoretical predictions of the quasiparticle band gap [13] [67] [68]and renormalization effects [28]. As such, this spectroscopic approach serves as a facile way to identify the quasiparticle band gap in monolayer TMDC semiconductors in a broad range of device configurations, providing an all-optical compliment to STM [53] [55] [71] [72] [74]. Directly quantifying the fundamental quasiparticle band gap and exciton binding energies and their corresponding renormalization effects is essential for developing exciton-based optoelectronic devices in monolayer TMDC semiconductors that capitalize on their remarkable ability to tune the underlying many-body interactions.

2.5 Additional contents

2.5.1 Material growth and device fabrication

Monolayer MoS_2 (ML-MoS_2) was grown by chemical vapor deposition (CVD) [62]. The CVD growth was carried out in a two-zone tube furnace. Sulfur and MoO_3 precursors were placed inside a quartz tube and located in zone 1 and zone 2, respectively, of the tube furnace. The SiO_2/Si substrates for MoS_2 to grow on were placed on top of the crucible that held MoO_3 precursor in zone 2. N_2 gas was flown through the quartz tube during the entire growth process. The temperature for zone 1 and zone 2 was kept at 105 °C for 3 hours, and then ramped up to 517 °C (over 30 minutes) for zone 2 and stayed at 517 °C for 30 minutes while zone 1 was kept at 105 °C during this time. Before this point, the N_2 gas was flown at 200 sccm and was changed to 9 sccm afterwards. The temperatures for zone 1 and 2 were then increased to 400 °C and 820 °C, respectively, and stayed at these temperatures for 10 minutes. After this 10 minutes' growth was over, the tube furnace was turned off and cooled down naturally to room temperature.

The back-gated devices were fabricated by conventional optical lithography, followed by metal (Ti/Au 2nm/50nm) evaporation and lift-off. Electrical transport measurements reveal the typical n-type doping behavior at the residual condition, as shown in Fig. 2.5.1.

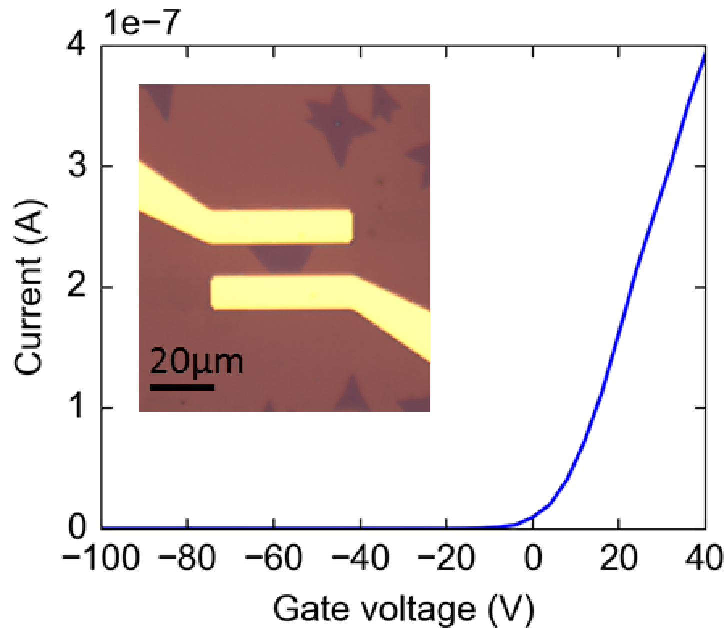

Figure 2.5.1. Typical transfer characteristics of fabricated monolayer MoS_2 field effect transistors measured at 80K. Inset shows the device photograph.

2.5.2 Photoluminescence excitation spectroscopy and analysis

Photoluminescence excitation (PLE) spectroscopy was performed with a supercontinuum laser (5ps pulse width, 40MHz repetition rate) passed through an acoustic optical tunable filter as excitation source. The laser beam was expanded to approximate a parallel incident beam. Diameter of the illumination area was ~10μm. The laser power was kept very low (less than $5W/cm^2$) to

ensure that photoluminescence (PL) intensity scales linearly with excitation power. The PL spectra were collected with a cooled CCD.

Here we estimate the photo-generated excitation density as following. The typical laser power used for PLE is ~7μW measured at the back aperture of objective, corresponding to a photon pump fluence of 5.3×10^{11}cm^{-2} for 2.65eV. The absorbance of ML-MoS_2 at this energy is estimated as 15% from Figure 2(a) of the main text. Then the density of photons absorbed by MoS_2 per pulse is estimated to be 8×10^{10}cm^{-2}. At our measurement temperature of 80K, carrier lifetime is expected to be much longer than the laser pulse width of 5ps, due to the rapid thermalization of photo-generated carriers, and the reduced efficiency of nonradiative processes [75]. Hence, the photoexcitation density at the quasiparticle band edge is estimated to be 8×10^{10}cm^{-2} for our experiments.

For PLE measurements on back-gate devices, the 285nm-thick SiO_2 dielectric layer impose a strong interference effect in the range of our excitation energies. The reflected waves from the SiO_2/Si substrate carry different amplitudes and phases, interfering coherently with the incident wave. Therefore, the actual electromagnetic field intensity felt by the atomically thin MoS_2 on top of the SiO_2 is not proportional to the measured incident laser power. We account for this effect by calculating the interference correction factor which is defined as the ratio of the actual local electromagnetic field intensity felt by MoS_2 on the SiO_2/Si substrate over intensity of the incident field. The directly measured PLE spectra are then scaled per the interference correction factor so that the effective excitation photon flux is the same for each excitation energy. The calculation is performed by the transfer matrix method [76], with wavelength dependent indexes of Si and SiO_2. The optical path length of MoS_2 flake is much shorter than that of 285nm SiO_2, and we hence neglect its effect in interference correction. Fig. 2.5.2(a) shows the calculated interference correction factor. To verify this correction method, similar CVD-grown monolayer MoS_2 flakes were transferred from the growth substrate (SiO_2/Si) to thick quartz substrates for PLE measurements. The PLE spectrum measured on quartz is compared with our interference-corrected PLE spectrum measured on SiO_2/Si, as shown in Fig. 2.5.2(b). The larger noise is due to significantly decreased (estimated to be about two orders of magnitude) quantum yield after the transfer process. We see that the uncorrected PLE spectrum acquired on SiO_2/Si takes a declining trend due to the interference effect (red dots in Fig. 2.5.2(b)), which does not reflect the intrinsic material property, as detailed in our previous work [59]. After correction, the spectrum shows a similar growing trend as that acquired on the interference-free quartz substrate.

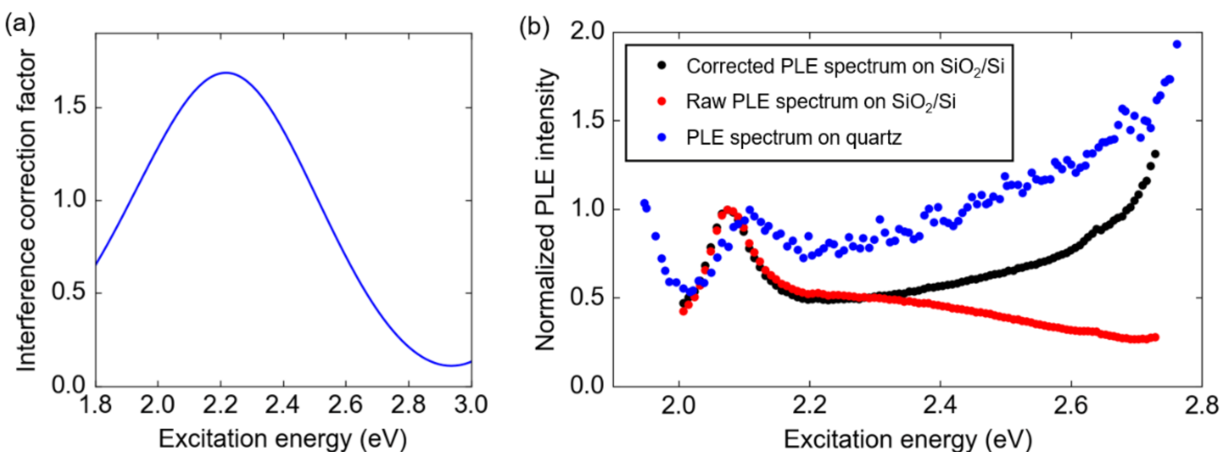

Figure 2.5.2. Correcting substrate induced thin film interference effect on PLE spectra of ML-MoS_2. (a) Calculated interference correction factor, as defined in the text. (b) Raw PLE spectrum measured for ML-MoS_2 on a 285nm-thick SiO_2/Si substrate (red dots), the interference-corrected PLE spectrum (black dots), and PLE spectrum measured for ML-MoS_2 transferred onto thick quartz substrate (blue dots). All three spectra are normalized to the peak of B exciton.

The experimental data of PLE intensity can be well fitted by an exponentially-tailed step-function plus a polynomial background. The absorption contribution from C exciton tail and the ensemble of high-energy Rydberg exciton states of the spin-split B series are accounted for by the polynomial background. The absorption due to the continuum of A band, $I_{cont.}(E_{ext})$, as a first approximation, may be expressed as:

$$I_{cont.}(E_{ext}) = \begin{cases} A_{cont.}, & E_{ext} > E_{con} \\ A_{cont.}e^{\frac{E_{ext}-E_{con}}{E_U}}, & E_{ext} < E_{con} \end{cases} \quad (2.1)$$

Here E_{ext} is the excitation energy, E_{con} is the continuum onset energy, E_U describes the width of low energy tail, and $A_{cont.}$ is a proportionality factor representing oscillator strength of the continuum. The step-like function for $E_{ext} > E_{con}$ is the expected function for free carrier density of states of a non-interacting 2DEG [44] [64, 77] [30]. In a system with strong electron-hole interaction, the absorption lineshape due to free carriers near the quasiparticle band edge may deviate slightly from the simple step-function [14]. Precise modeling of the band edge absorption lineshape warrants future computational works. In this work, however, we find that a step-function with an exponential tail can adequately capture the experimental spectral features. The exponential tail possibly accounts for band edge disorder states and the ensemble of highly excited Rydberg exciton states of the A series close to the continuum edge. Equation (1) is further convolved with a Gaussian function with full width half magnitude (FWHM) of 10meV to account for possible heterogeneous broadenings.

The PLE spectra shown in Fig. 2.2 and Fig. 2.3 of the main text are constructed by integrating the total PL counts in the spectrometer collection range, including emission from both the free A excitons and the defect-bound DX excitons. In Fig. 2.5.3 we compare the PLE spectra obtained by integrating different portion of the PL spectra. Fig. 2.5.3(a) shows the color contour of absolute PL counts measured at each different excitation energies complimentary to the inset of Fig. 2.2(a) of the main text, where the PL counts have been normalized to the A emission peak in order to visualize the variation of relative defect PL yield with excitation energy. Fig. 2.5.3(b) compares the PLE spectra obtained by integrating the total PL counts (green dots), A exciton PL counts (magenta dots), and defect PL counts (yellow dots). All three spectra show identical features (B exciton resonance and the change of slope at ~2.63 eV) only with background differences.

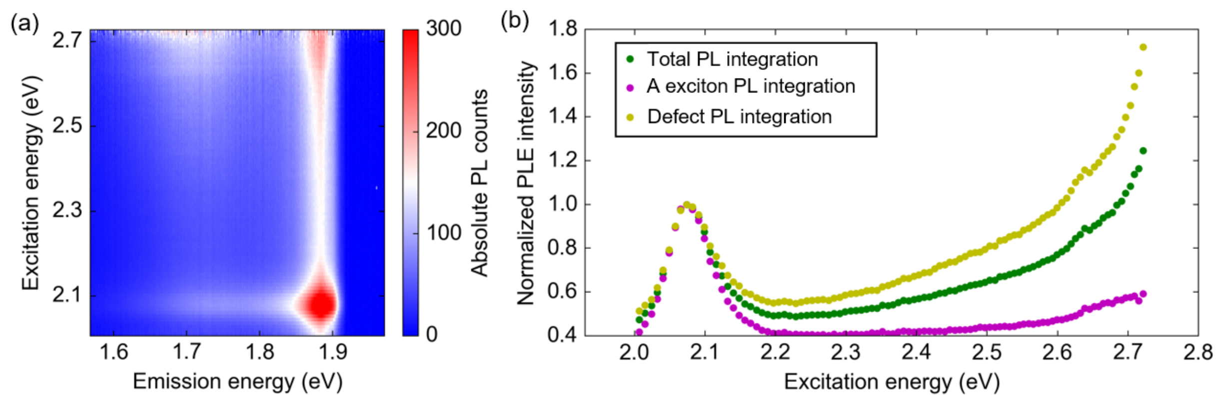

Figure 2.5.3. (a) Color contour of the absolute PL counts measured at each different excitation energies, with a V_g of -60V. Note that this is the same data set as the inset of Fig.2b in the main text, but without normalization. (b) PLE spectra obtained by integrating the total PL counts (green dots), the A exciton PL counts (magenta dots), and defect PL counts (yellow dots). All three spectra are normalized to their intensities at the B exciton peak at ~2.07eV.

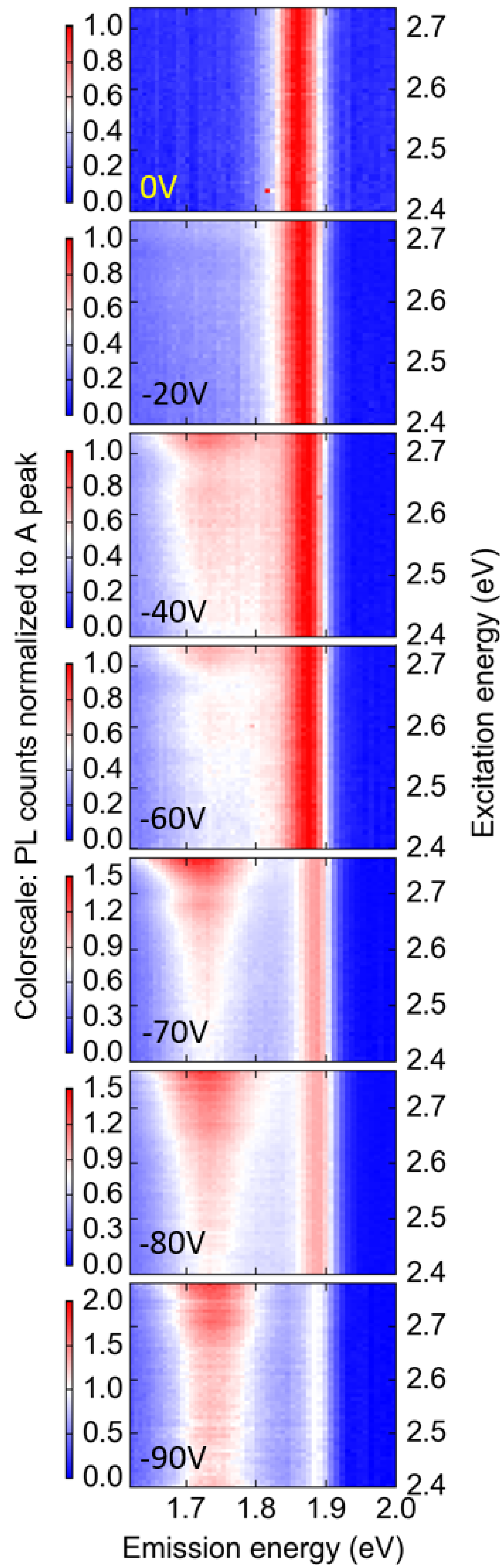
Colorscale: PL counts normalized to A peak
Excitation energy (eV)
Emission energy (eV)
0V
-20V
-40V
-60V
-70V
-80V
-90V
1.0
0.8
0.6
0.4
0.2
0.0
1.5
1.2
0.9
0.6
0.3
2.0
1.5
1.0
0.5
2.7
2.6
2.5
2.4
1.7
1.8
1.9
2.0

Figure 2.5.4. Color contour of normalized PL spectra measured with varying gate voltages, complementary to Fig. 2.3 of the main text.

2.5.3 Identification of exciton and trion states from reflectivity spectra.

Absorption spectra are obtained from reflectivity measurements. A Halogen lamp was used for illumination. A 100μm pinhole was used with a 60X objective (NA=0.6) to ensure that the collected signal comes from a localized area of ~2μm in diameter, much smaller than the typical flake size. The reflectance spectra from the flake R_f and from the substrate (quartz or SiO_2/Si) R_s are collected, and the reflectivity contrast was calculated as $R_{con} = \frac{R_f - R_s}{R_s}$. For samples on quartz substrate, the absorbance A is directly proportional to R_{con} as $R_{con} = \frac{4A}{n_s - 1}$ [78] where n_s is index of substrate. For samples on SiO_2/Si substrate, Kramers-Kronig method [21] is employed for fitting the reflectivity ratio (R_f/R_s) spectra (Fig. 2.5.5(a)) and obtaining the absorption spectra (Fig. 2.5.5(b)). The absorption peak energies of exciton and trion states are determined by fitting gate-dependent absorbance with two Lorentzian functions representing the A^0 neutral exciton (blue dashed line) and negatively-charged A^- trion (red dashed line), and a polynomial background representing the contribution from oscillators located at higher energies outside the fitting range [21]. A 10meV Gaussian broadening has been applied. The fitted resonance energies are shown in Fig. 2.5(a) of the main text. Note that the vertical error bars in Fig. 2.5(a) come from standard deviation of the fitting process.

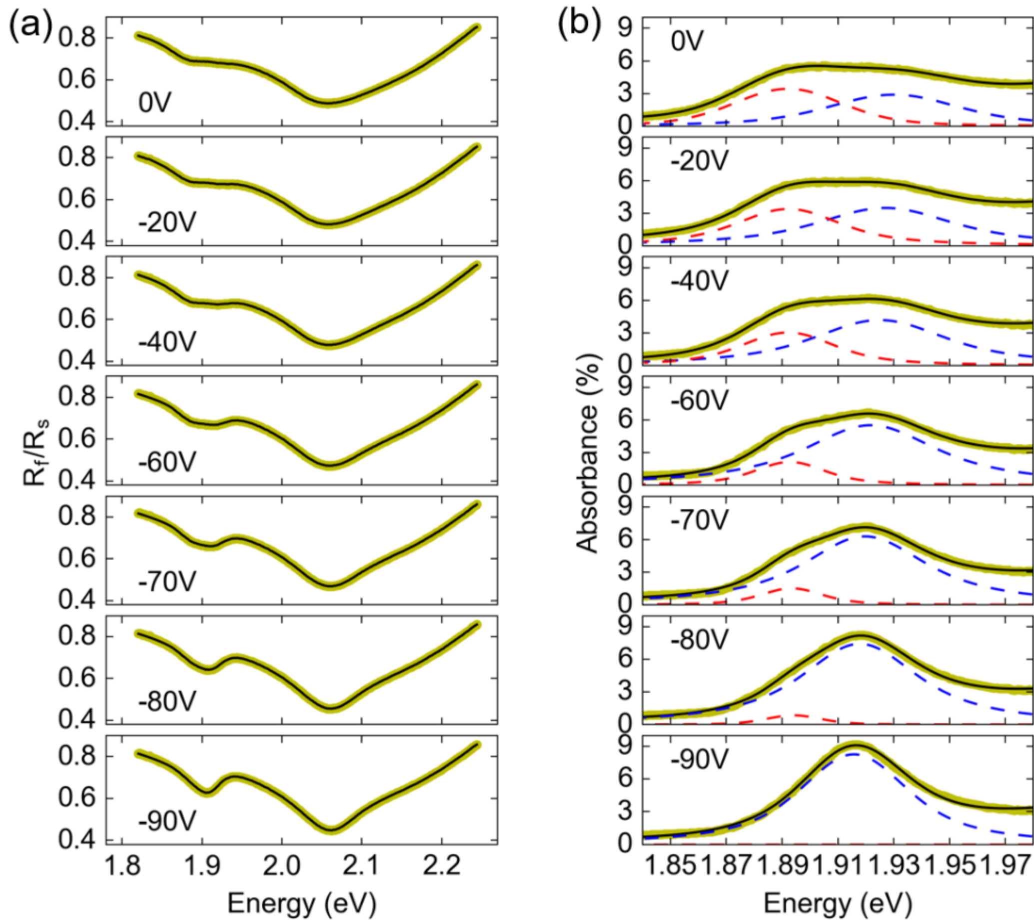

Figure 2.5.5. (a) The experimental data (yellow thick lines) of reflectance ratio R_f/R_s is fitted by Kramers-Kronig method [21] (black thin lines) at different gate voltages as labeled. (b) The gate dependent absorption spectra (yellow thick lines) obtained from the Kramers-Kronig analysis. These absorption spectra are further fitted to identify exciton and trion states. Black thick lines show total fitting results, with blue (red) dashed lines representing the contribution from the A^0 neutral exciton (negatively-charged A^- trion) states.

2.5.4 Determination of gate induced doping concentration from Stokes shift

In this section, we discuss the determination of electron doping concentration at each gating voltage by measuring gate-dependent Stokes shift [21]. Stokes shift here is defined as the energy difference between the absorption peak and PL peak of the same exciton states, which is expected to be linearly proportional to the Fermi energy and carrier doping concentration in a 2D system [21].

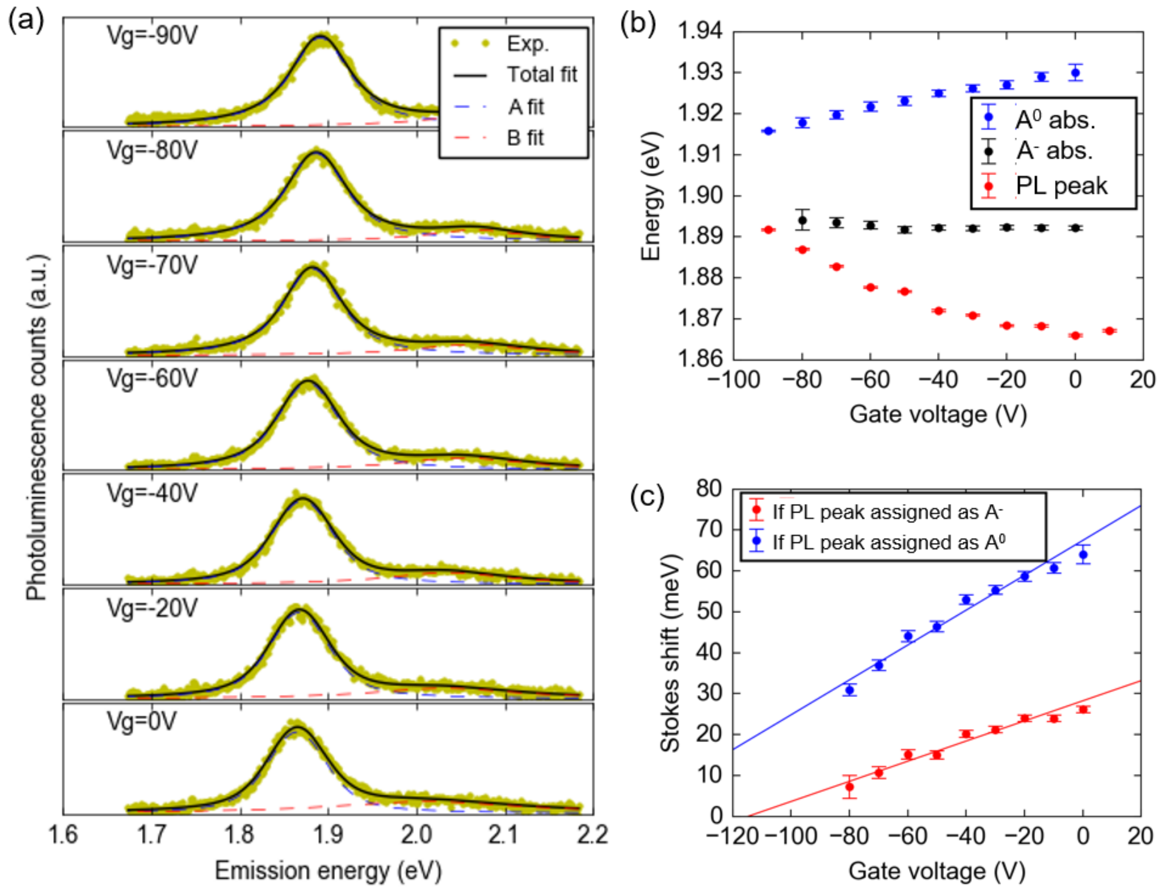

Figure 2.5.6. Determination of the neutral gate voltage that corresponds to zero electron doping concentration. (a) PL spectra measured at different gate voltages V_g, fitted with two Lorentzian functions representing the emission from A and B bands. (b) Dependence of the absorption peak energy of neutral exciton A^0 (blue dots), negatively-charged trion A^- (black dots), and the PL peak energy (red dots) on gate voltage. (c) Dependence of Stokes shift on gate voltage, with two possible assignments of the PL peak. The assignment of A^- state is favored (see text).

The absorption peak energy for trion and excitons states have been determined as in Section III above. In PL measurements, the defect PL overlaps significantly with the direct A exciton PL peak, and cannot be well fitted with simple Gaussian profiles. Since the defect PL has a sublinear power dependence and saturates at higher excitation density [60], the excitation density is increased (~1000W/cm^2) to saturate defect PL for more accurate fitting of exciton energies. We note that this excitation density is still several orders below Mott transition [29], and the A exciton PL peak is not observed to shift or broaden between the relatively higher and lower excitation densities in our experiments. Fig. 2.5.6(a) shows the gate-dependent PL spectra and fitting results. Under all gate voltages, the major PL peak can be well fitted with one single Lorentzian function. Fig. 2.5.6(b) shows the fitted results of peak energies from PL and absorption measurements. The PL peak is red-shifted with increasing electron doping concentration, agreeing well with the previously reported trend of negatively charged trion A^- [21]. Fig. 2.5.6(c) shows the gate dependent Stokes shift, and compares the results for two different assignments (neutral exciton A^0 or negatively-charged trion A^-) of the PL peak. The neutral gate voltage (corresponding to zero doping) is determined as the linearly extrapolated point where the Stokes shift becomes zero. If the PL peak was assigned as from neutral exciton A^0, the neutral gate voltage would be -163V and the electron doping concentration at V_g=-90 V would be as high as ~6×10^{12}cm^{-2}. However, the trion feature in absorption spectra has already disappeared at V_g=-90 V (Fig. 2.5.5), indicating that the electron doping concentration at this gate voltage is already close to intrinsic [22]. Hence, based on the gate-dependent energy shift of the PL peak, as well as the gate-dependent absorption oscillator strength of A^- trion versus A^0 exciton, we determine that the PL peak is from A^- trion instead of neutral exciton A^0. PL from the neutral exciton A^0 is not appreciable, as a possible result of the high residual doping concentration, as well as the low measurement temperature which favors luminescence from the lower energy trion state [21]. With this assignment, the neutral gate voltage V_{g0} is determined to be -114±6V. The electron concentration n_e at each applied V_g is then determined from the capacitance (per area) of the 285nm-thick SiO_2 dielectric layer C_{ox} as n_e= $C_{ox}(V_g$-$V_{g0})$. The horizontal error bars in Fig. 2.4 and Fig. 2.5 of the main text come from the standard deviation of the fitted neutral gate voltage.

The binding energy of the ground state neutral exciton A^0 is determined as the energy difference between quasiparticle band gap E_g and the energy E_{A^0} (i.e., the optical band gap) required to create an A^0 exciton. We note that E_{A^0} could ideally be obtained from the PL peak of A^0. However, as discussed above, the PL spectra we measured at low temperature is dominated by A^- and the features of PL from A^0 is not appreciable. On the other hand, A^0 and A^- can be well deconvolved from absorption spectra as in Fig. 2.5.5, and the measured absorption peak energy $E_{A^0}^{abs}$ of the A^0 neutral exciton state is expected to be only slightly higher than the optical band gap E_{A^0} by the Stokes shift E_{sts} [21]. Thus, the optical band gap is rigorously obtained as $E_{A^0}=E_{A^0}^{abs}-E_{sts}$. Hence the binding energy is calculated as $E_{bnd}=E_g-E_{A^0}=E_g-E_{A^0}^{abs}+E_{sts}$, and shown in Fig. 2.5(b) of the main text as a function of electron concentration, where the error bars of E_{bnd} sum up that of E_g, $E_{A^0}^{abs}$ and E_{sts}.

2.5.5 Additional results

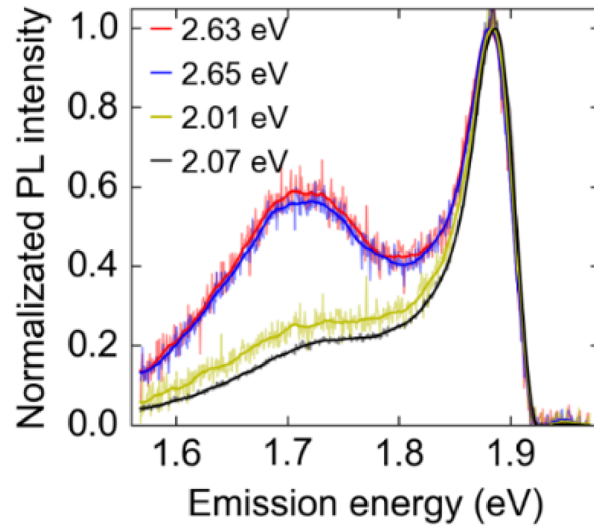

Figure 2.5.7. Full PL spectra showing the suppression of defect photoluminescence with resonant excitation of B exciton at ~2.07 eV and the continuum at ~2.65 eV, as complimentary to Figure 2 (b) of the main text. Semi-transparent thin lines represent the raw data. Solid thick lines show the smoothed spectra using a second order Savitzky Golay filter with a window size of 20 meV.

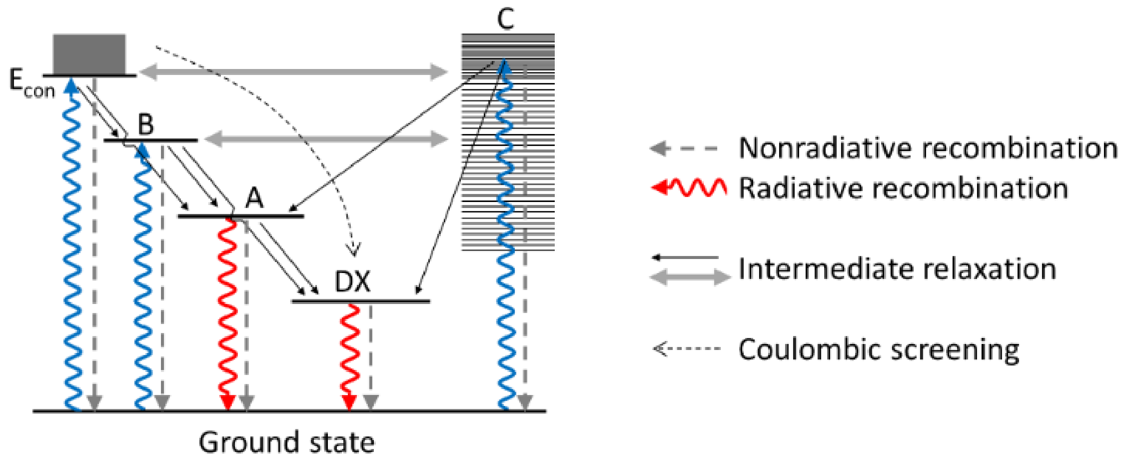

Figure 2.5.8. Complete level diagram as complimentary to Figure 2.2 (c) of the main text.

Chapter 3 – Strongly quantum confined excitons in two-dimensional layered hybrid metal chalcogenide multi quantum wells

3.1 Introduction

Two-dimensional (2D) transition metal dichalcogenide (TMD) materials represent the extremum of quantum confinement in semiconductors - down to only one monolayer of unit cells. At this limit, many-body interactions dominate optical responses leading to excitons, trions and biexcitons with binding energies significantly larger than those in bulk semiconductors and robust for manipulation at room temperature [30] [13] [24] [19] [21] [79] [80]. In addition to fundamental interests, the strong excitonic effects greatly enhance light-matter interaction, allowing one monolayer of TMD to show strong absorption, reflection, emission, and nonlinear optical responses absorb more than 10% of light on its exciton resonances [19] [59] [17] [16] [81] [39]. Notably, applications such as light emitting diodes [82], excitonic lasers [6] [83] [84], and ultrafast modulators [85] would benefit from creating stacks of such monolayers separated by insulating barriers, effectively resulting in a multi-quantum-well (MQW) structure with atomic-level confinement and exceptionally high optical cross sections. Such an ideal three-dimensional system allows for efficient interactions between excitons and photons over the full volume of a photonic cavity mode, which is critical for most device platforms, particularly those aiming for control and utilization of exciton-polaritons [86] [87] [88]. Recently, significant efforts have been dedicated to the development and facile chemical synthesis [89] [90] of such structures based on the halide perovskite materials system, resulting in hybrid organometallic "bulk" crystals of stacked, minimally interacting 2D layers with tunable exciton energies [91] [92] [93]. However, the metal-chalcogenide analog of such systems has yet to be realized, despite offering a compelling combination of strain-, field-, and polarization- tunable excitonic structure and material stability.

In this work, we report the optical properties of a new metal chalcogenide direct-gap layered 2D semiconductor, silver benzeneselenolate ($[AgSePh]_\infty$), also named as "mithrene" in short, which is engineered to form the desired three dimensional multi quantum well structure via facile self-assembly [94] [95]. We find that the optical transitions are dominated by tightly-bound excitons with ultrafast dynamics. A family of bright and dark exciton states are revealed by one-photon and two-photon photoluminescence excitation (PLE) spectroscopy. The ground state excitons have a large binding energy of approximately 0.4 eV, similar to those in monolayer TMDs and layered 2D perovskites [19] [92] and significantly higher than conventional three dimensional semiconductors such as GaN, ZnO, etc. [96] [97]. Exciton lifetimes below 20 ps are determined from time resolved photoluminescence measurements, consistent with the intrinsically strong oscillator strength of the ground state exciton. Density functional theory calculations imply significant quantum confinement of electronic carriers within inorganic layers and that the ligand has only a small impact on the electronic structure of the band gap. Finally, to further elucidate the quantum confinement nature within these materials, mithrene derivatives are studied where the composition of organic barrier layer is varied while the semiconducting layer remains unchanged. PLE measurements on these derivatives establish how structural modifications can affect excitonic optical properties.

3.2 Crystal structure and electronic band structure of mithrene

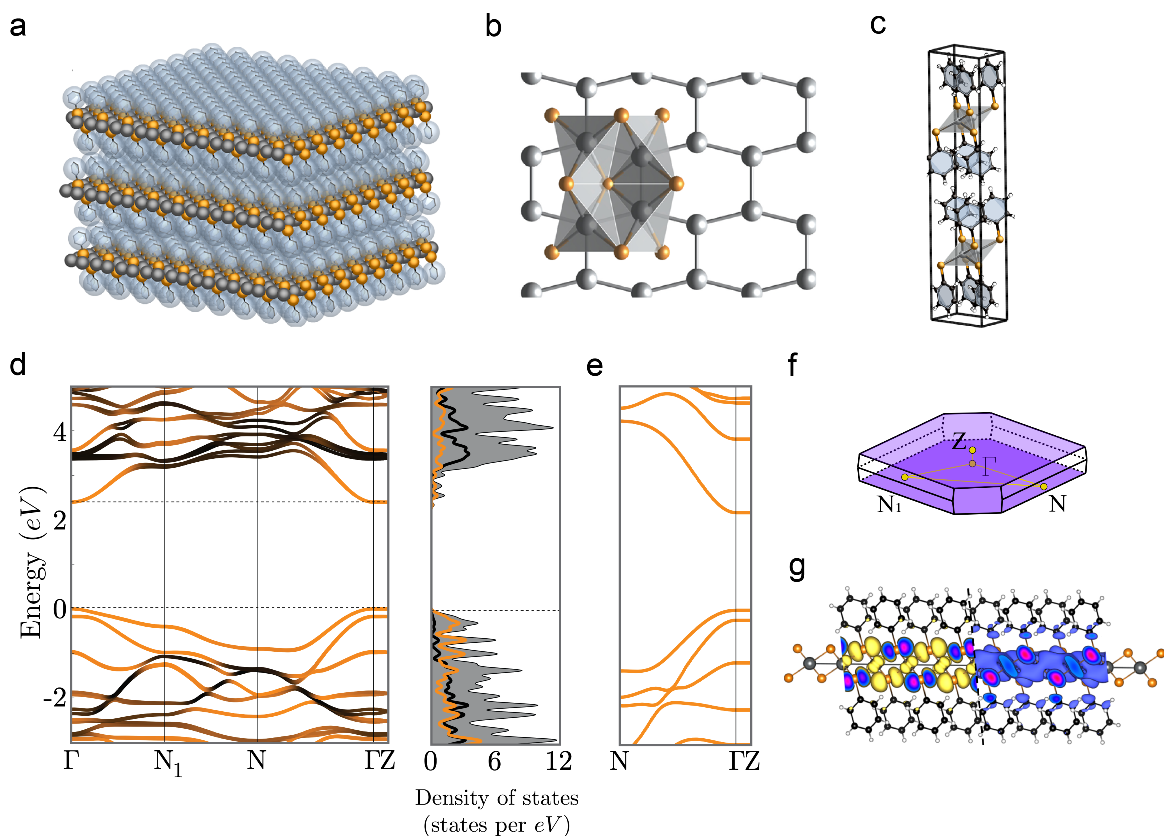

Figure 3.1. Crystal structure and electronic band structure of mithrene. (a) Perspective view of the multilayered crystal structure. The inorganic semiconducting monolayers of AgSe are electronically decoupled via the benzene moieties oriented above and below. (b) Top view of the in-plane lattice of one AgSe layer. Silver atoms are crystalized in to a distorted hexagonal lattice with Ag-Ag separation of 3 Å. (c) The conventional unit cell of mithrene. Silver is represented as the grey spheres, selenium in dark orange, and carbon in black. Aromatic rings are accented in blue. (d) Electronic band structure and density of states of bulk mithrene crystal from density functional theory calculations. The band structure calculated for a monolayer shown in section 3.8 is indistinguishable from bulk crystals. A direct band gap is found at the Γ point. Band color signifies the fractional contribution of states centered on inorganic (orange) and organic (black) layers in the crystal. The total density of states is shown in grey. Low energy carriers at band edges are predominantly from inorganic AgSe layers. (e) Electronic band structure of a ligand-modified mithrene layer where phenyl rings are replaced by hydrogen atoms. (f) The Brillouin zone for the conventional cell. The path in the Brillouin zone used for displaying the band structure is identified by yellow lines and k-point labels. (g) Side view of the charge density maps of band edge electrons. The valence band maximum (VBM) and conduction band minimum (CBM) at Γ are accented in yellow and blue, respectively. The band edge carriers are confined within the 2D monolayer of AgSe.

Mithrene is an organic-inorganic layered hybrid material with a self-assembled multi quantum well structure as shown by Figure 3.1a. Ag and Se atoms form an inorganic semiconducting layer, and each AgSe layer is sandwiched between two organic layers of benzene molecules. The adjacent benzene layers are bonded together by van der Waals forces, and the

interlayer spacing between two neighboring AgSe layers is 1.4 nm [95] [94]. In contrast to manually stacked heterostructures consisting of monolayer TMDs separated by few-layer hexagonal boron nitride (hBN) barrier layers [98] [99], these layered crystals are grown at immiscible water-toluene interfaces, or via a bulk solution based synthesis, both are in a single pot syntheses [94] [95]. Within the semiconducting layers of AgSe shown schematically in Figure 3.1b, the Ag atoms adopt an elongated hexagonal lattice, with each Ag atom bonded to four surrounding Se atoms in a tetrahedral geometry. The Ag-Ag in-plane separation is determined to be 3 Å [100] . Each AgSe layer is sandwiched between two organic layers of benzene molecules which have a large energy gap of above 5 eV between its highest occupied molecular orbital (HOMO) and lowest unoccupied molecular orbital (LUMO). Intuitively, the organic layers naturally serve as the barriers for confining electrons and holes within the AgSe layers. Figure 3.1c shows the conventional unit cell.

The electronic band structure of mithrene calculated by density functional theory (DFT) is shown in Figure 3.1d, with the first Brillouin zone sketched in Figure 3.1f. A direct band gap of about 2.4 eV is found at the Γ point. To better understand the system, we calculate band structures for bulk mithrene and monolayer mithrene and found them to be indistinguishable at the DFT level as shown in section 3.8. This implies that interlayer coupling is extremely weak. As shown by the layer-resolved fractional contribution of states, the low-energy electron states close the band edges are predominantly contributed by Ag and Se atoms in the inorganic layer, while the organic phenyl layers only affect the states energetically far away from the band edge, consistent with the relatively large HOMO-LUMO gap of benzene. In Figure 3.1e, we show part of the band structure for a ligand-modified monolayer mithrene layer where the phenyl rings are replaced by hydrogen atoms. The full band structure is included in section 3.8. The low energy states in the AgSe layer are minimally affected by ligand modifications, as experimentally verified by optical spectroscopy in later parts. Figure 3.1g shows iso-surfaces of the square of the wavefunction for mithrene's conduction band minimum (CBM) and valence band maximum (VBM) states at the Γ point. While the state at the VBM exhibits directional bonding associated with Ag 4*d* and Se 3*p* character, the CBM is more delocalized, featuring significant Ag 5*s* character. As seen in Figure 3.1e, the minimal contribution of *p* states from phenyl groups to band edge states – with VBM and CBM iso-surface density visible only on the carbon atoms adjacent to the AgSe layer – reflects the weak coupling between AgSe layers. The DFT calculated band structure and electronic wavefunctions present the multi quantum well electronic structure of mithrene.

3.3 Optical characterization of mithrene samples

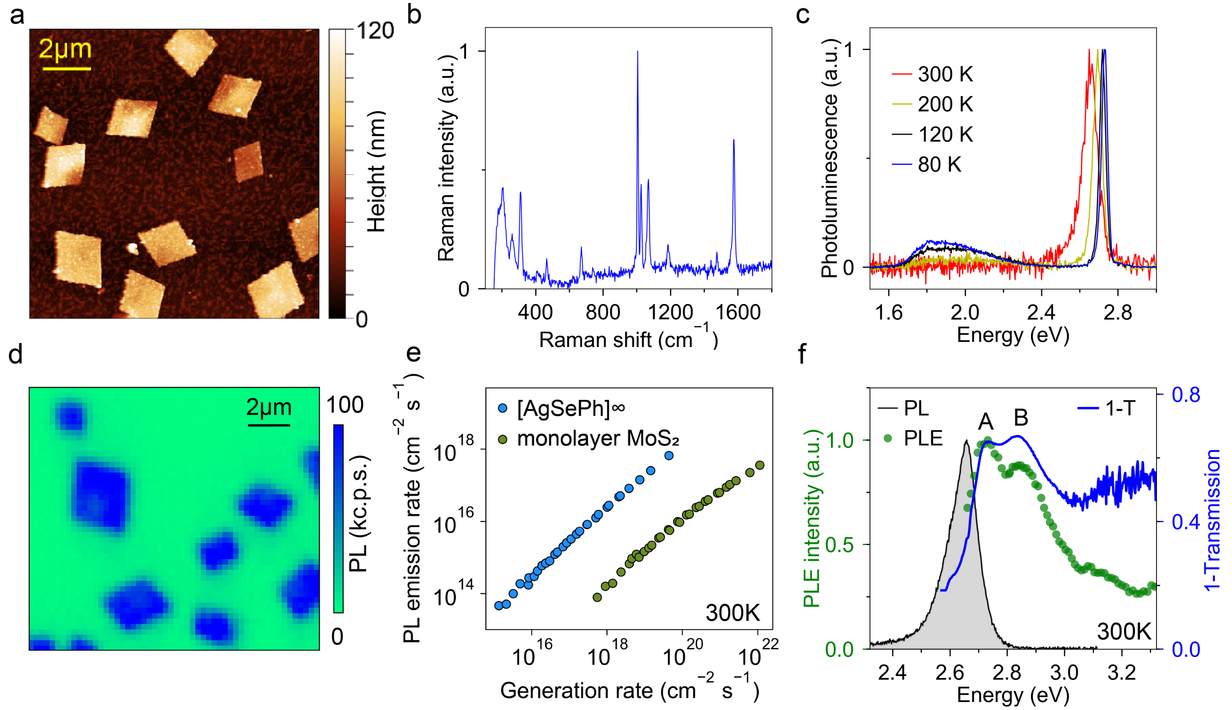

Figure 3.2. Optical characterization of mithrene samples. (a) Atomic force microscopy of mithrene micro-platelet crystals dropcasted on quartz substrate. (b) Raman spectrum and (c) temperature dependent photoluminescence (PL) spectra of mithrene. (d) Confocal PL imaging of the same sample. (e) Typical PL photon emission rate as a function of carrier generation rate (photon absorption rate). Data for a piece of mithrene single crystal is compared with a monolayer MoS_2 flake. An extrinsic quantum efficiency of ~2% can be extracted for mithrene. (f) Absorption spectrum and photoluminescence excitation (PLE) spectrum at room temperature, showing two prominent excitonic resonances at 2.73 eV and 2.84 eV, labeled as A and B excitons respectively. The normalized PL spectrum is also plotted with grey filling for comparison.

An atomic force microscopy (AFM) image of a typical single crystal mithrene sample is shown by Figure 3.2a. The mithrene sample crystallizes into a micro platelet shape with an edge angle of ~77°, resembling the shape of its first Brillouin zone. The average thickness for this sample is approximately 75 nm corresponding to roughly 53 layers of quantum wells. A Raman spectrum of mithrene is shown in Figure 3.2b, where we identify strong A_1g benzene ring breathing modes around 1000 cm^{-1} and the E_2g benzene C-C in-plane stretching mode at 1580 cm^{-1}. The multiple peaks around the A_1g mode may be induced by symmetry breaking due to C-Se bonding. The low energy Raman peaks at 310 cm^{-1} and 265 cm^{-1} are observed for AgSe quantum wells confined with different organic ligands (see section 3.8), and thus are likely to be intrinsic optical phonon modes of the AgSe lattice.

Selected temperature-dependent photoluminescence (PL) spectra are shown in Figure 3.2c, and PL spectra at more temperature points are included in section 3.8. At room temperature the PL is dominated by a single peak at 2.66 eV with a lower energy tail. As temperature is reduced to 80K, the major PL peak blue shifts to about 2.70 eV and the lineshape becomes more symmetric, indicating that the asymmetric PL lineshape may be related to exciton-phonon interaction. A more detailed analysis of temperature dependent PL lineshape is included in section 3.8 as well.

Moreover, a new emission band at much lower energy around 1.8 eV gradually emerges with decreasing temperature. We assign this feature as photoluminescence from defect-bound excitons based on the sublinear dependence of its emission intensity versus excitation power section 3.8. Figure 3.2d shows a confocal PL imaging of the same sample in Figure 3.2a but at a different area. In order to estimate photoluminescence quantum yield, the excitation and collection efficiencies of the confocal microscope and the single photon detector used for measurement are quantitatively calibrated at the excitation laser wavelength and photoluminescence peak wavelength of mithrene and a reference sample of monolayer MoS_2 grown by chemical vapor deposition on sapphire substrate [101]. Figure 3.2e shows the PL photon emission rate as a function of generation rate. The generation rate is the photon flux (number of photons per unit area per second) being absorbed by the sample. The incident laser power is measured and then converted to generation rate based on sample's optical absorption. For the 75-nm-thick mithrene crystals we estimate an optical absorption of 60% for the 430nm laser based on transmission spectra in Figure 3.2f. For monolayer MoS_2 the absorption is estimated to be 30% at 430 nm according to previous literatures [19]. The PL emission rate is the photon flux directly measured by an avalanche photo diode, and then multiplied by a calibration factor accounting for microscope collection efficiencies. More experimental details are included in section 3.8. The ratio of PL emission rate over generation rate directly gives the extrinsic quantum efficiency at room temperature, which is determined to be ~2% for mithrene and 0.02% for monolayer MoS_2. The measured extrinsic quantum efficiency of monolayer MoS_2 agrees well with other reports [102] [83]. We note that, inside 75-nm-thick platelet, the emitting photons are likely being trapped inside the crystal due to cavity effect or total internal reflection. If the lateral size of the platelet is significantly larger than exciton diffusion lengths, the intrinsic quantum yield may be estimated as $4n^2$ times the extrinsic quantum efficiency with n being the refractive index [103]. Thus, the 2% extrinsic quantum efficiency would point to an even higher internal quantum yield which makes mithrene promising for constructing active optoelectronic components.

Figure 3.2f shows the spectrum of 1- transmission measured from an individual 75-nm-thick mithrene crystal on quartz. A collection pinhole is used to spatially filter the light for minimizing edge scattering effects. Figure 3.2f also shows the PLE spectrum which is obtained by plotting integrated PL intensity as a function of excitation laser energy and further normalized to the excitation photon flux [19] [59]. Both data show two prominent exciton peaks with similar oscillator strength at 2.73 eV and 2.84 eV, and are labeled as A and B excitons respectively. These two peaks may be arising from excitons comprising of holes from the two closely-spaced valence bands near the VBM at Γ point in the band structure in Figure 3.1c. The A and B absorption peaks may also arise from band splitting induced by spin orbital coupling which is not considered in the current DFT calculation. It's also interesting to note that the lowest A exciton absorption peak is about 70 meV higher than the PL peak at 2.66 eV. The large energy separation is unlikely to be simply due to a large spatial-heterogeneity effect, since the PL emission peak energy is very uniform across one piece of crystal as revealed by hyperspectral PL imaging section 3.8. In fact, we notice that there is a very subtle change of slope in the absorption spectra in Figure 3.2f around 2.67 eV. It suggests that the PL could come from the trion state [21] of the A exciton, or another exciton state closely degenerate to the A exciton.

3.4 Revealing bright and dark excitonic states and exciton binding energy with photoluminescence excitation spectroscopy

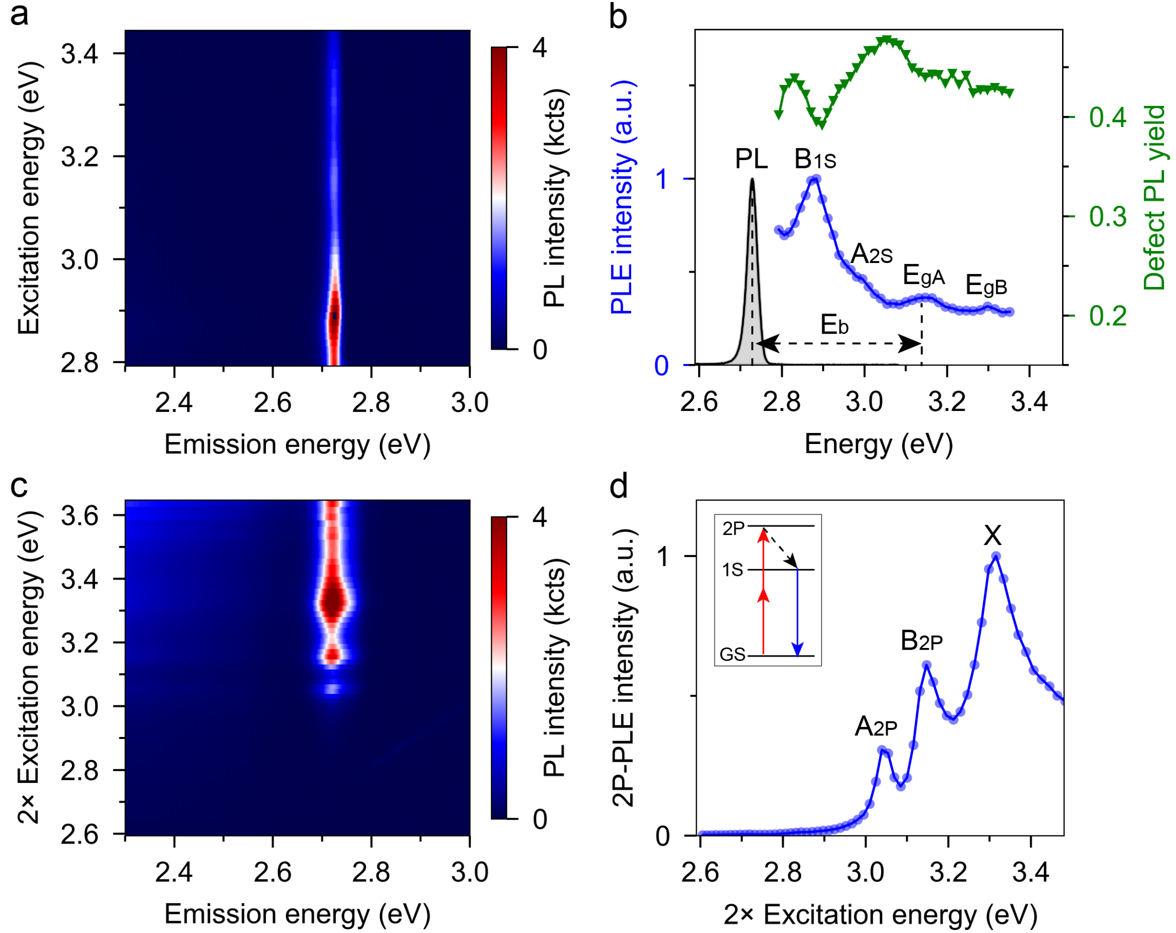

Figure 3.3. Revealing bright and dark excitonic states and exciton binding energy with one photon and two photon photoluminescence excitation (PLE) spectroscopy. (a) Color map of PL emission spectra versus one-photon excitation energy. (b) Dependence of integrated PL intensity (blue) and defect PL yield (green) versus excitation energy. A representative PL spectrum (black with grey shade) excited at 2.9 eV is also shown for comparison. A strong B_{1s} exciton is observed at 2.87 eV, while the weaker features at higher energy are assigned as exciton excited states A_{2s} and quasiparticle band edge features E_{gA} and E_{gB}. Quenching of the defect PL yield is observed upon resonant excitation at quasiparticle band edge, as discussed in the text. (c) Color map of two-photon excited PL spectra versus twice the excitation photon energy. (d) Two photon PLE (2P-PLE) spectrum showing the intensity of 2P-PL emission versus twice the excitation photon energy. Dark excitons at 3.04 eV, 3.15 eV and 3.32 eV are observed, and the lowest two peaks are assigned as A_{2p} and B_{2p}. The data shown here are collected at 5K. Temperature dependent PLE data are included in section 3.8.

To gain further insight into the nature of the optical transitions, we perform photoluminescence excitation (PLE) spectroscopy under both one-photon and two-photon excitation conditions. This allows us to reveal bright and dark exciton states, and also to quantify exciton binding energies, as shown previously in monolayer TMD semiconductors [19] [24]. The data measured at 5K are shown in Figure 3.3 with temperature dependent results reserved for section 3.8. Figure 3.3a shows a color map of PL spectra collected under different one-photon

excitation energies. The PL emission peak is at 2.72 eV at all excitation energies. The integrated PL emission intensity is shown as a function of excitation photon energy in Figure 3.3b as the PLE spectrum. Four main features are observed and assigned as exciton Rydberg series: the ground state B exciton (B_{1s}) peak at 2.87 eV, the A_{2s} exciton excited state at 3.0 eV, and two broad peaks labeled as E_{gA} and E_{gB} at 3.13 eV and 3.27 eV, respectively. The spectral feature of the B_{2s} exciton excited state is likely obscured due to its energy overlap with the E_{gA} transition. As shown previously in Figure 3.2c, PL from defect-bound excitons are observed at low temperatures. Here in Figure 3.3b we also show the relative PL yield of these defect-bound excitons over the total PL emission from all spectrum range. Importantly, quenching of relative defect PL is also clearly observed at E_{gA}, consistent with previous observations for free carrier excitation at the energy of the quasiparticle band gap within monolayer TMDs [19]. This is due to the additional screening of Coulomb interactions between defect sites and free excitons by the photo-excited free carriers. Therefore, we assign E_{gA} to be the quasiparticle band gap, yielding an exciton binding energy of 410 meV as indicated by E_b in Figure 3.3b. E_{gB} is tentatively assigned to be the quasiparticle band gap for the B exciton, resulting in a B exciton binding energy of 400 meV. The exciton binding energy obtained from PLE spectroscopy agrees well with quantitative GW-Bethe-Salpeter equation (GW-BSE) calculation of mithrene as reported in a separate work [104]. The large exciton binding energy in three dimensional crystals of mithrene is already comparable to that of atomically thin two-dimensional semiconductors [54] [30] [19]. This is a direct result of the multi-quantum-well structure of self-assembled mithrene crystals.

Excitonic optical transitions follow selection rules based on the net spatial symmetry of the envelope exciton wavefunction and the underlying electronic orbitals [105] [14]. Linear spectroscopies only access the excitonic bright states with s-type symmetry. On the other hand, excitonic dark states with p-type symmetry are probed by nonlinear two-photon PLE [24] [54]. In this measurement, near-simultaneous absorption of two low energy photons can excite excitonic dark states, which subsequently relax to the bright A exciton states. The resulting two photon PL emission spectra are collected at each two-photon excitation energy as shown by Figure 3.3c. It's verified that the two photon PL emission intensity indeed scales quadratically with the infrared excitation laser power section 3.8. The integrated two photon PL intensity of the A exciton is plotted versus twice the excitation energy in Figure 3.3d. Three sharp excitonic dark states can be identified at 3.04 eV, 3.15 eV, and 3.31 eV. The lowest two resonances have comparable oscillator strength, and have the same energy splitting as that between the A_{1s} and B_{1s} bright excitons. Therefore they're assigned as the 2p excited states of A and B Rydberg exciton series. The 3.31 eV resonance has a much stronger oscillator strength than the 2p excitons, so we exclude the possibility of it being a 3p dark state. Instead, we speculate that it could be a dipole-forbidden transition from other bands [14]. The unambiguous identification of dark excitons and the large energy separation between 1s and 2p states in the Rydberg series corroborate the finding of giant exciton binding energy, and clearly evidence the strong many-body interaction and quantum confinement of charge carriers in the system.

3.5 Ultrafast exciton dynamics of mithrene

Exciton oscillator strength, or optical transition probability, is generally proportional to its binding energy [14]. Therefore, tightly-bound excitons are expected to be manifested in ultrafast recombination dynamics [106]. Figure 3.4a shows the temperature dependent photoluminescence decay traces of the major PL exciton around 2.7 eV measured at selected temperatures. The data are fitted with a biexponential decay model, with a fast picosecond-scale decay component and a

slow nanosecond-scale decay component. At all temperatures, amplitudes of the fast picosecond-scale components are about 50 times larger than the slow nanosecond-scale components. Complete data and fitting results are included in section 3.8. The extracted exciton lifetimes of the major fast decay are shown in Figure 3.4b versus temperature from multiple repeated measurements. We found that mithrene has an exciton lifetime of below 25 ps across the whole temperature range from 5 K up to room temperature. The short exciton lifetime is comparable to those observed in monolayer TMDs [107]. This is consistent with the knowledge that mithrene's ground state exciton is confined within an atomically thin layer of AgSe. It is also interesting that the temperature dependence of the lifetime shows opposite trends below and above approximately 150 K. At lower temperatures, the exciton's decreasing lifetime with increasing temperature is most likely due to increased nonradiative recombination rates. At higher temperatures, it has been suggested that the excitons can be effectively thermalized with a significant population out of the light cone, resulting in an increasing lifetime with temperature [107].

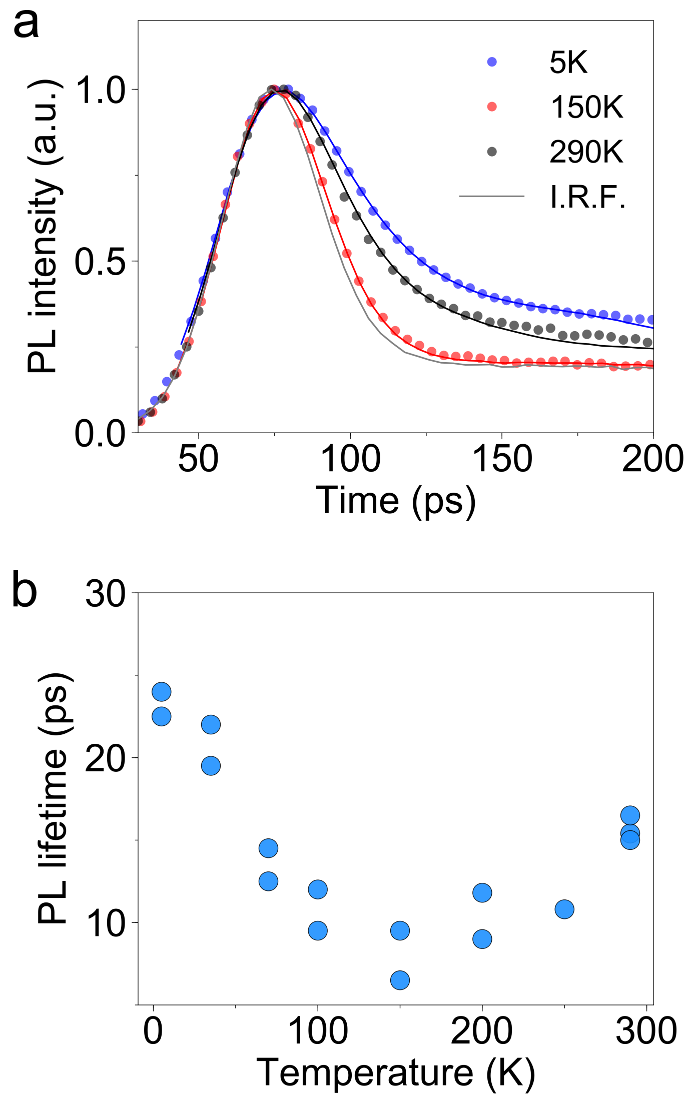

Figure 3.4. Ultrafast exciton dynamics of mithrene. (a) Photoluminescence decay traces measured at different temperatures. The measured data are deconvolved by the instrument response function (I.R.F.) to obtain PL lifetime. (b) Extracted PL lifetime versus temperature.

3.6 Effect of different organic ligands on exciton states

Finally, we demonstrate the tuning of optical properties by changing the organic ligands that form the quantum well barrier layers. DFT calculation suggests that the wavefunction of band edge electrons and holes are mostly constructed by Ag 4p, Se 4p, and Ag 5s orbitals, with very little contribution from the organic barrier layer. However, the extremely strong quantum confinement within these quantum-well layers is expected to push a portion of the exciton wavefunction into the barrier layers. Therefore, to further investigate such quantum confinement effects, we perform PL and PLE measurements on mithrene analogs prepared with different ligands. The benzene rings that construct the organic barrier layers are changed to biphenyl and methoxybenzene, and these structural modifications are verified by Raman spectra (section 3.8) of the synthesized materials that show characteristic vibrational modes of these substituted organic ligands. All three samples are direct band gap semiconductors, as evidenced by PL at room temperature as shown in Figure 3.5 a b c. The PL peak energies for mithrene, biphenyl-mithrene, and methoxybenzene-mithrene are close and are at 2.66 eV, 2.58 eV, and 2.59 eV, respectively. The insensitivity of PL energy to ligand modifications suggests that the band edge carriers forming the ground state exciton are not significantly affected by atoms in the barrier layer, thus further consolidating the multi quantum well nature of the system. Notably, the PLE spectra show features of A and B excitons close to the optical band gap for all three samples, but show very different absorption lineshapes at higher energies. As shown by the layer-resolved band structure in Figure 3.1c, the electronic states with energy far away from VBM and CBM take significant contribution from the organic layers, opening up the possibility of tuning optical response in the blue and ultraviolet region by ligand modifications. The three ligands used in this work all have much larger HOMO-LUMO gap compared with the AgSe layer. The relative alignment of the organic and inorganic states as shown by DFT calculations in Figure 3.1 also suggests an opportunity to tune the near-band edge character of each component by choosing a ligand with a smaller HOMO-LUMO gap, such as pentacene, which could contribute states hybridizing with those of AgSe at the band edges. Thus, it may be possible to achieve complete tunability of electronic properties of this system, as well as the coupling between layers, by ligand design.

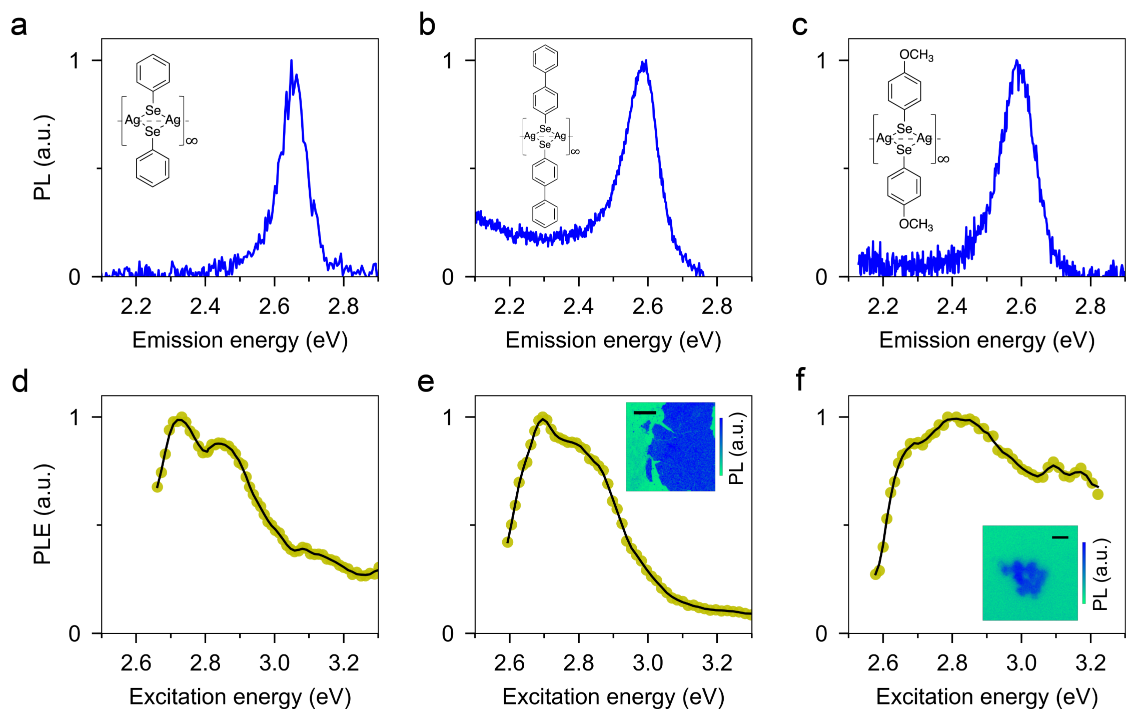

Figure 3.5. Effect of different organic ligands on exciton states. (a, b, c) Room temperature PL and (d, e, f) PLE spectra of samples where benzene, biphenyl, and methoxybenzene ligands, respectively, are used as quantum well barrier layers. Insets of (a, b, c) show the schematic structure of each crystal, and insets of (e, f) show the confocal PL imaging of biphenyl mithrene and methoxybenzene mithrene samples with scale bars of 20μm and 5μm, respectively. We note that (a, d) are from the same PLE dataset shown in Figure 3.2f, and are re-plotted here for comparison purpose.

3.7 Conclusion

In summary, we report a detailed study of the strongly excitonic optical properties of mithrene, a direct band gap metal chalcogenide semiconductor in the form of multilayered atomically-thin 2D quantum wells. The quasi 2D confinement in the multilayered structure results in a large exciton binding energy of about 0.4 eV, allowing clear observation and robust control of excitons at room temperature, making this family of mithrene materials a promising candidate for exploring and engineering many-body states in three dimensions. For device applications, mithrene features high photoluminescence efficiency, ultrafast exciton dynamics, and structural tunability with the potential to exchange ligands, metal atoms and chalcogen atoms [108] to tailor its properties. Mithrene could open up new possibilities for novel hybrid metal chalcogenolate based photodetectors, light emitting diodes, solid-state lasers, quantum cascaded devices, and ultrafast optical modulators, etc. As such, we anticipate the emergence of a whole family of easily-synthesized, mithrene-inspired layered excitonic materials in the form of multi-quantum-wells for both fundamental research and practical applications.

3.8 Additional contents

3.8.1 Raman spectra of AgSe quantum wells confined by barrier layers of different organic ligands

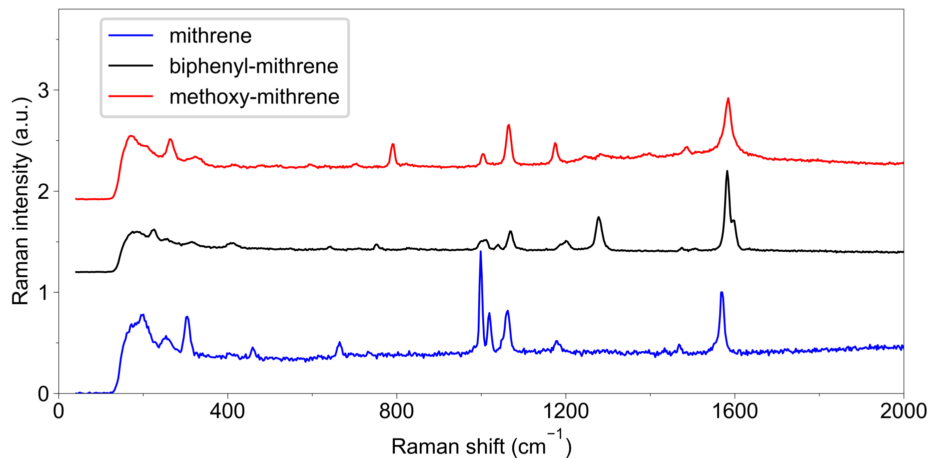

Figure 3.8.1. Raman spectra of mithrene, biphenyl-mithrene, and methoxy-mithrene. In mithrene/biphenyl-mithrene/methoxy-mithrene, the monolayer AgSe quantum wells are confined by barrier layers of benzene/biphenyl/methoxybenzene molecules, respectively. Excitation laser is 633 nm.

Different organic molecules can be used to substitute benzene to form the barrier layer, and these structural modifications are revealed by Raman spectra. On benzene-coordinated mithrene samples, a strong peak is observed at 1006 cm^{-1} which is attributed to the A_{1g} ring breathing mode of the benzene molecules. The energy of this mode is slightly blue-shifted compared with that observed on isolated benzene [109]. More peaks are observed at 1025 cm^{-1} and 1068 cm^{-1} which are likely the appearance of originally-inactive vibrational modes (for example, the E_{1u} in-plane C-H bending mode originally at 1037 cm^{-1}) due to the broken symmetry in the hybrid crystalline system. In addition, we do not clearly observe the double-peak Fermi resonance features at 1584 cm^{-1} and 1606 cm^{-1} which are characteristics of stand-alone benzene molecules [110]. Instead, a single peak with a very weak low energy shoulder is observed at 1575 cm^{-1} which is likely the fundamental E_{2g} C-C stretching mode [109] [110]. In comparison, the biphenyl-mithrene samples show two obviously additional Raman peaks: a 230 cm^{-1} peak corresponding to the low frequency phenyl-phenyl stretching mode, and a 1280 cm^{-1} peak corresponding to the inter-ring C-C stretching mode [111] [112], proving the successful substitution of benzene molecules with biphenyl molecules in the system. On methoxy-mithrene samples, a strong peak is observed at 795 cm^{-1} which has been identified as the B_{1U} ring stretching mode which is sensitive to the $–OCH_3$ group [113]. Finally, we notice that the low energy Raman peaks at 310 cm^{-1} and 265 cm^{-1} are observed on all three samples and thus assigned to be intrinsic optical phonon modes of the AgSe lattice.

3.8.2 Temperature dependent photoluminescence and emergence of defect-bound excitons

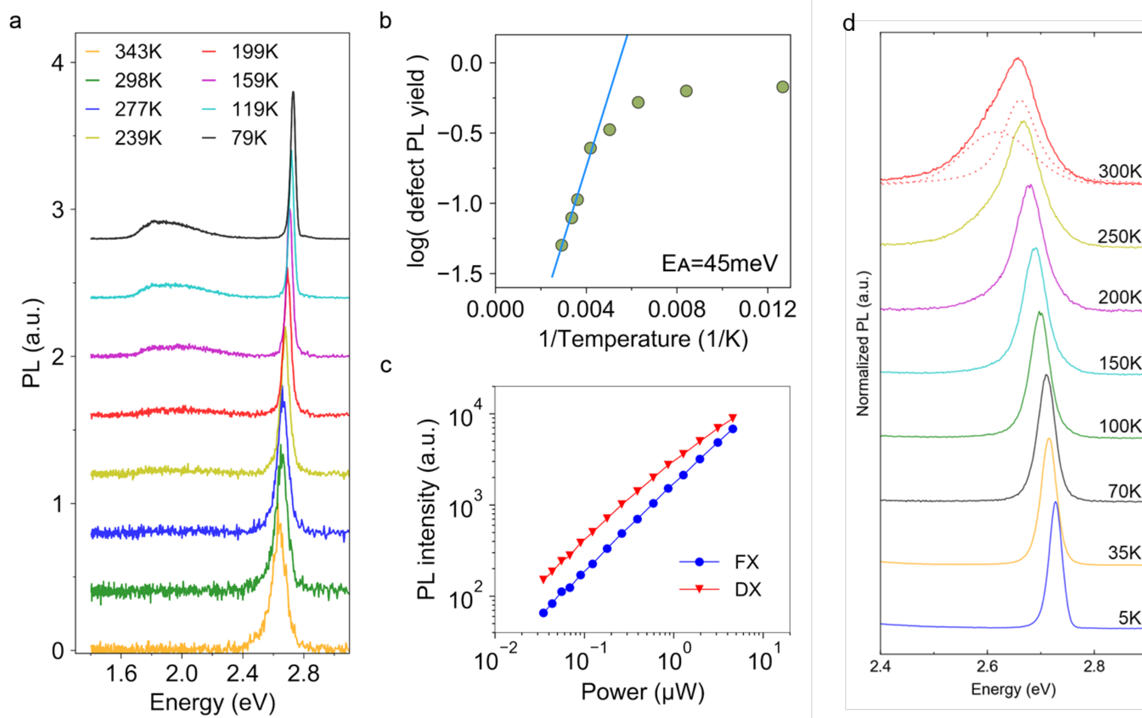

Figure 3.8.2. Experimental signatures of photoluminescence from defect-bound excitons in mithrene. (a) Temperature dependent PL spectra, showing the emergence of a low energy PL band at ~1.9 eV with decreasing temperature. (b) Change of relative defect PL yield (defined as the ratio of defect PL over total PL intensity) with temperature. A thermal activation energy of 45 meV can be deduced from the slope of the linear part at high temperatures. (c) Power dependence of the PL intensity of free exciton (FX) and defect-bound excitons (DX) at 79 K. The sublinear trend of DX at high power is a signature of defect PL due to saturation of limited amount of lattice defect sites. (d) Temperature dependent PL taken with a finer grating centered around the PL peak, for a different sample. As temperature goes up, the PL peak becomes more and more asymmetric with a second low energy peak showing up, indicating an exciton-phonon interaction.

3.8.3 Measurement of photoluminescence quantum yield

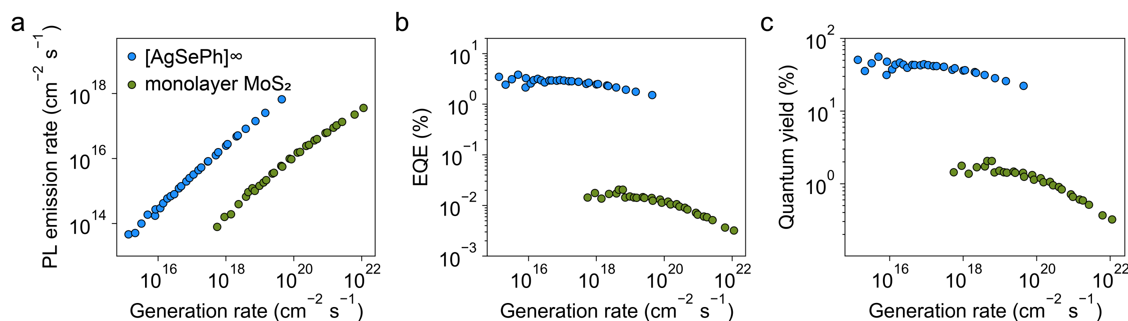

Figure 3.8.3. Power dependent quantum yield measurement of mithrene ($[AgSePh]_\infty$) and compared with monolayer MoS_2. (a) PL emission rate measured as a function of generation rate. (b) External quantum efficiency (EQE) as extracted from raw data presented in (a). (c) Intrinsic quantum yield of mithrene as calculated from the directly-measured EQE.

Mithrene is shown to be an efficient blue light emitter. We perform power-dependent emission intensity measurements on single crystal samples at room temperature. For this experiment, we use a 100X NA=0.95 objective and 430nm excitation laser which is in close resonance with the B exciton. We first perform a diffraction-limited confocal imaging with an avalanche photodiode (APD) to locate a piece of single crystal and then measure power-dependent PL intensity. The excitation laser power is continuously tuned across four orders of magnitude using a motorized neutral density filter wheel. We measure the laser power before entering the microscope in the real time of data collection with a pick-off beam splitter. The ratio between the laser power coming out of the objective and the laser power measured at the pick-off position is calibrated by replacing the sample with a silicon photodiode powermeter. In order to calibrate collection efficiency, the laser is tuned to the emission wavelength and kept at a low power, and the sample is replaced with a spectralon diffuse reflector which provides isotropic reflectance close to 100%. The laser reflection intensity is then measured by the APD with a protective neutral density filter. The same experiments are performed on a sample of monolayer MoS_2 on sapphire substrate as a comparison. In Figure 3.9.3a, the measured PL emission rates are plotted as function of generation rate with a laser energy of 2.82 eV. We note that the generation rate has taken into account the absorption and reflection of the samples. We consider that 30% of excitation power at this energy is absorbed by the monolayer MoS_2 in accordance with previous literatures [19]. For the mithrene sample with average thickness of 75nm, we consider that the 60% of incident power is all absorbed by the material. Fig. 3.9.3b shows the directly-measured EQE (extrinsic quantum efficiency) of mithrene and monolayer MoS_2. In Fig. 3.9.3c the EQE data is converted to intrinsic quantum yield (QY) based on the light trapping model [103], i.e., $QY = 4n^2 \times EQE$. Our results show that mithrene has a very high PL QY of about 40% using a refractive index of 2 at the PL peak wavelength as measured by ellipsometry on Ag-tarnished thin film samples. The measured QY slightly decreases with increasing generation rate, which is likely due to stronger Auger recombination and/or thermal heating effects under high excitation power.

3.8.4 Hyperspectral PL imaging showing uniform distribution of PL energy

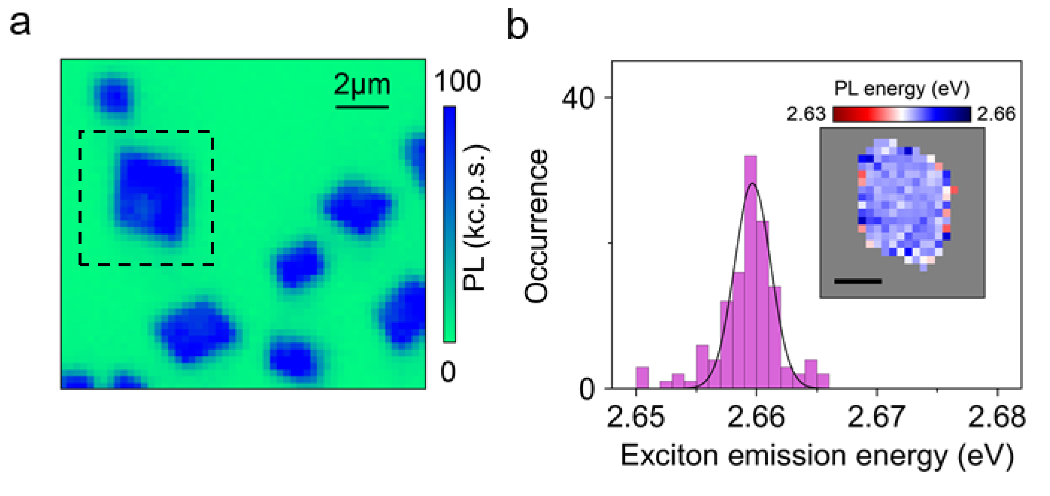

Figure 3.8.4. Hyperspectral imaging of mithrene micro-crystals. (a) Map of PL emission intensity. (b) Histogram of PL peak energy measured at different positions in the boxed region of (a). Inset of (b) shows the spatial distribution of PL emission energy.

In order to investigate sample homogeneity, we perform confocal hyperspectral microscopy with diffraction-limited resolution of about 200 nm. A 100X NA1.3 objective is used to image the micro-crystal sample with a 400 nm excitation laser. The map of PL intensity is shown in Figure 3.9.4a and the distribution of exciton emission energy in the boxed region is presented in Fig. 3.9.4b. We find that mithrene has an extremely homogeneous distribution of PL peak energy within only 5 meV which is much smaller than the PL spectral linewidth, indicating that any inhomogeneous broadening is beyond the diffraction limit. This is in stark contrast to monolayer transitional metal dichalcogenides which typically has a very large emission energy variation of several tens of meV over one flake. The homogeneous emission property of mithrene implies that the micro-crystal samples have minimal defects and edge states.

3.8.5 Photoluminescence excitation (PLE) experiments and temperature dependent PLE spectra

The one photon PLE experiments performed in this work use the second harmonic generation signals from a femtosecond Ti:Sapphire laser as a continuously tunable laser source to excite the sample. For two photon PLE experiments, the main output beam of the Ti:Sapphire laser is used for excitation. In both cases, a continuously tunable neutral density filter wheel and a pick-off powermeter is being automated together and controlled with a PID program to maintain a uniform photon excitation flux. The transmission efficiency for the excitation beam path is also calibrated. The reported PLE and two photon PLE data are all normalized in such a way that the photon excitation flux are constant across the excitation energy range. The samples are mounted in a liquid helium cryostat and optically accessed with a 50X NA 0.55 objective. To minimize chromatic aberration and sample drifting at low temperature, the laser beam is typically slightly defocused to about 5-10 µm with an additional lens before the objective. The photoluminescence spectra are collected in a back-scattering fashion with the same excitation objective, dispersed by a 150g/mm grating, and measured by a cooled CCD camera. Proper filters are used to clean out the excitation laser signals from the collection beam.

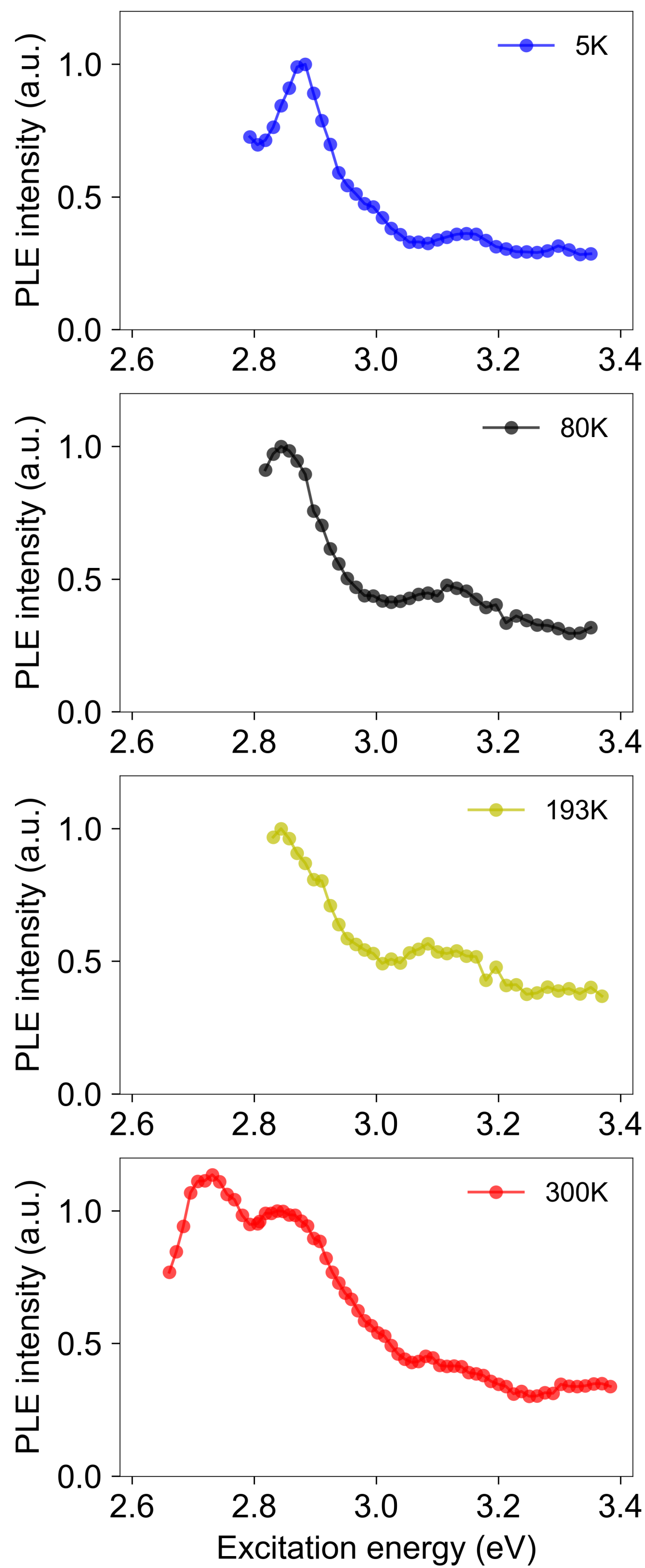

Figure 3.8.5. Photoluminescence excitation (PLE) spectra measured at different temperatures. All the four spectra are normalized to the B exciton peak at about 2.8~2.9 eV. Both the B exciton peak

and the band edge feature around 3.1~3.2 eV red shifts with increasing temperature, an expected behavior for semiconductor band gaps. We note that only in the room temperature (300K) experiments can we resonantly excite the A exciton at 2.73 eV. This is simply due to lab availability of suitable fluorescence filters.

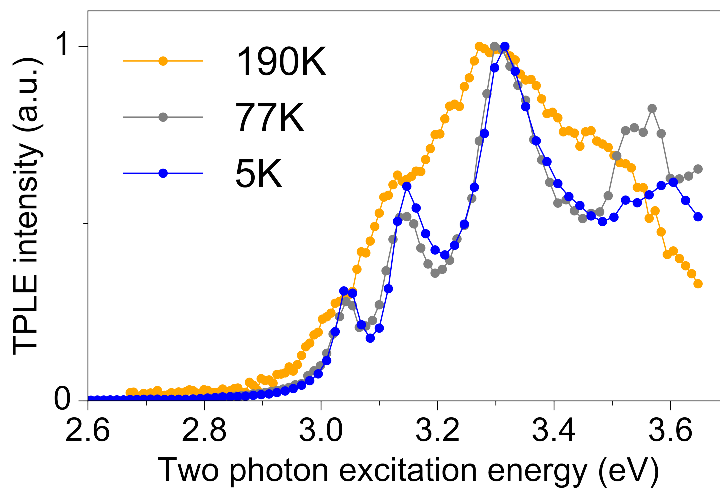

Figure 3.8.6. Two photon photoluminescence excitation (TPLE) spectra measured at different temperatures. The dark excitons can be observed up to about 190K, and they experience red shift with increasing temperature. We note that the peak at ~3.55 eV is observed on some samples but not others.

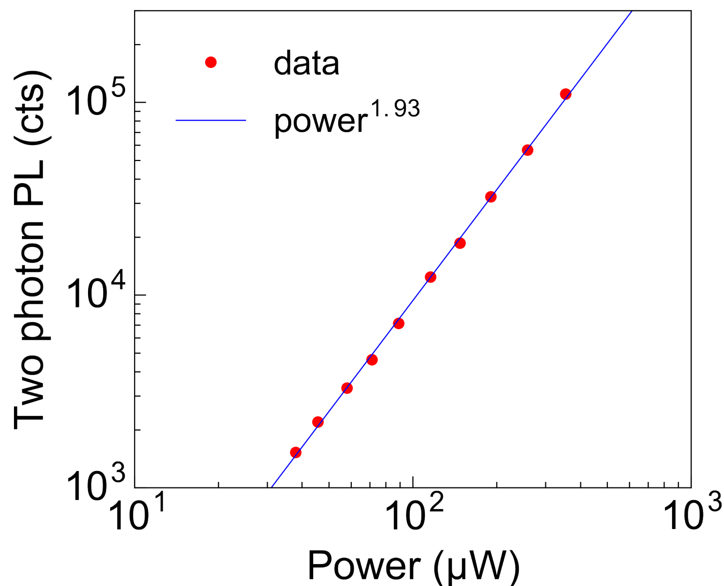

Figure 3.8.7. Intensity of two photon photoluminescence versus the power of femtosecond laser operated at 800 nm. The data can be well fitted by a power law relationship with power of 1.93, indicating that it's indeed a two photon process.

3.8.6 Temperature dependent time resolved photoluminescence measurements and data fitting

In TRPL measurements, sample are mounted in liquid helium and optically accessed by a 50X NA0.55 objective. Second harmonic generation of Ti:Sapphire laser at 390 nm is used for excitation. A 400 nm short pass filter is used to clean up laser signal. The pulse width is about 150 fs. Photoluminescence from mithrene samples are filtered with a 470/100 nm bandpass filter to ensure that the collected PL signal does not include contributions from defect-bound excitons. A bi-exponential decay model is used for extracting PL lifetime.

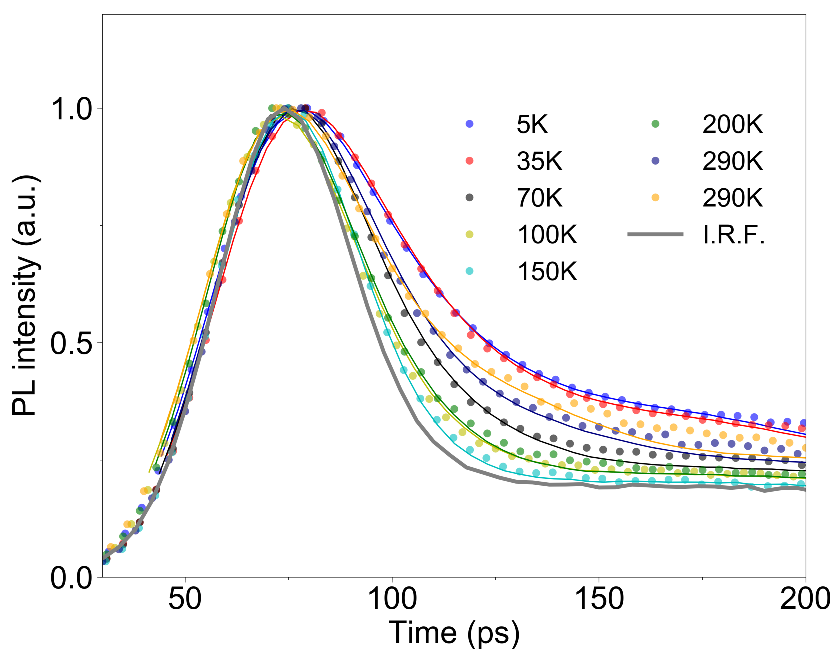

Figure 3.8.8. TRPL traces measured at all temperature points as supplementary data to Figure 3.4 in main text.

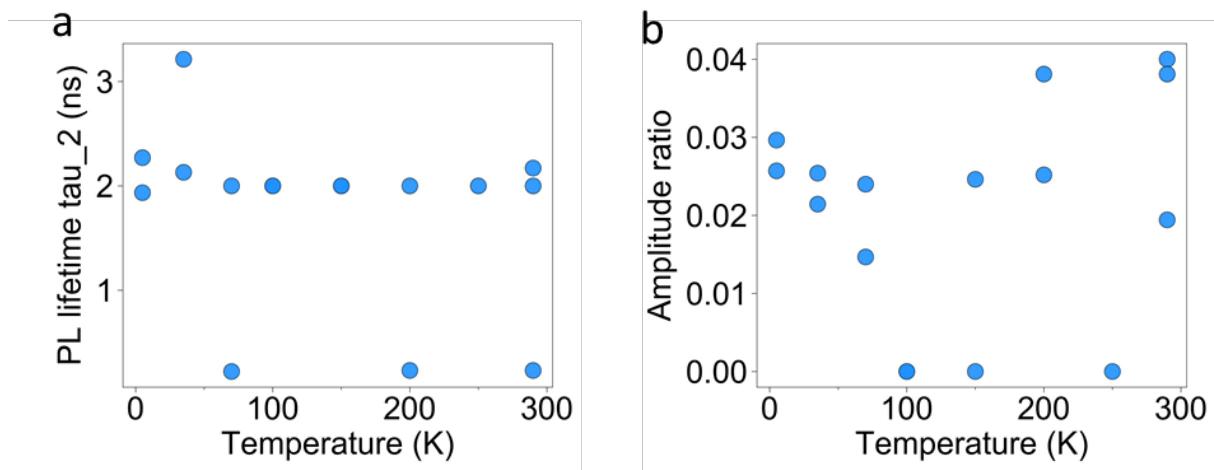

Figure 3.8.9. (a) Fitted lifetime of the second minor component. (b) Amplitude ratio of the second minor component over the first major component.

3.8.7 Additional results from DFT calculation

Methods and more details regarding density functional theory (DFT) calculation of silver benzeneselenolate are included in the [114]. Here we only include some key results.

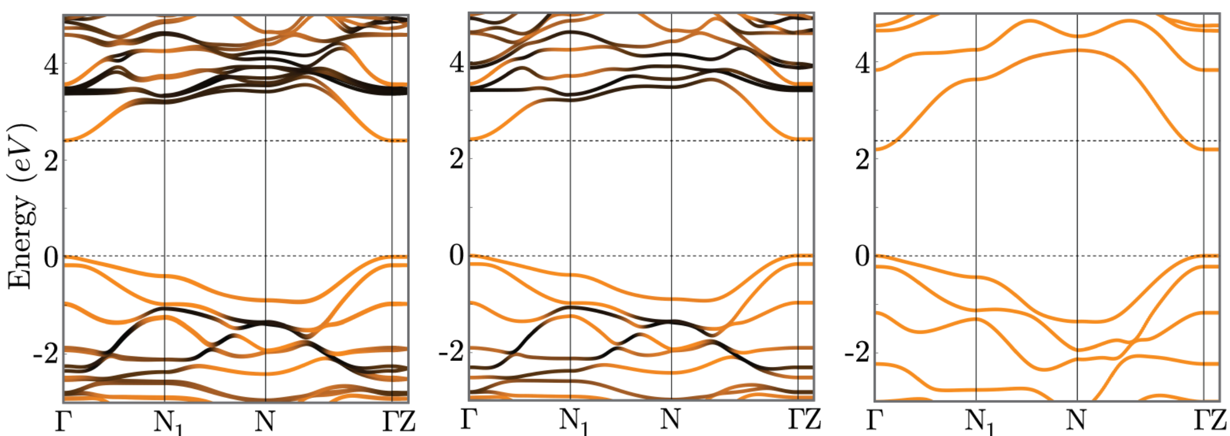

Figure 3.8.10. HSE band structures for bulk and single-layer [AgSePh]∞ and single layer [AgSePh]∞ with the phenyls replaced with hydrogens Dashed lines show the Fermi level (at 0 eV) and the HSE band gap for bulk and single-layer [AgSePh]∞. Color of band signifies the fraction of band occupations by inorganic atoms (Ag and Se) versus organic atoms (C and H).

3.8.8 Material synthesis

The mithrene materials used for this work are synthesized based on previously reported method [115] [94]. Ligand modified mithrene materials were prepared using similar methods, and varying the diselenide ligand used. The synthesis of all diselenide precursor ligands have been previously reported. Work expanding the set of ligand modified mithrene materials is currently ongoing, and more synthetic details will be included in future publications.

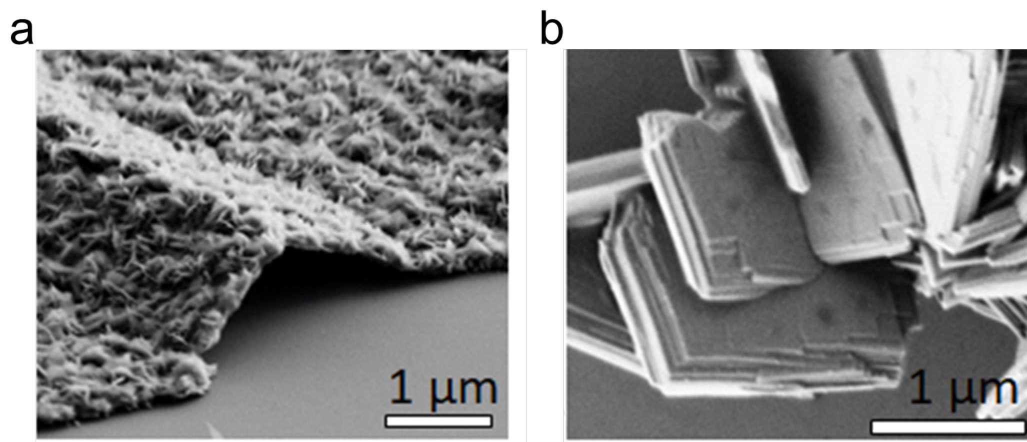

Figure 3.8.11. Scanning electron microscopy images of samples of (a) biphenyl mithrene and (b) methoxybenzene mithrene.

Chapter 4 – Continuous-wave nonlinear optics with atomically thin semiconductors and van der Waals heterostructures

4.1 Introduction

As noted in section 1.4, atomically thin semiconductors and van der Waals heterostructures has opened exciting new opportunities in novel nonlinear optical device applications with the benefits of strong and tunable light matter interaction. In the meanwhile, nonlinear optical spectroscopy and imaging techniques are also powerful tools in the development of two-dimensional (2D) materials and the exploration of intriguing many body physics in these systems.

Nonlinear optical experiments on 2D semiconductors are conventionally performed with pulsed excitation lasers where an extremely high instantaneous pump irradiance on the order of several to hundreds of TeraW/m^2 is typically delivered to the material [116] [37] [36] [38] [33]. Since nonlinear optical responses scale with high order of powers of the instantaneous pump irradiance [40], the pulsed excitation scheme can allow easy detection of the nonlinear signals of interest with high signal-to-noise ratio. However, realization of robust continuous-wave (CW) operation would be highly desirable for many practical applications such as low-cost on-chip laser sources and modulators, compact frequency converters for optical communications, and highly integrated optical sensors [117] [118]. Moreover, CW operation could also inspire the development of convenient, tunable, and multimodal spectroscopy and imaging techniques for the study of quantum materials. The CW nonlinear signals inherit the ultrafine linewidth of the CW pump laser, which is typically a few wavenumbers down to even sub-wavenumber, allowing the probe of exciton, plasmon, and phonon polariton fine structure with nonlinear excitation spectroscopy [119] [15] [120]. Many other complex nonlinear characterization techniques such as sum frequency generation (SFG), differential frequency generation, and four wave mixing would require simultaneous excitation of the sample with multiple laser beams. These applications may also be greatly simplified if CW operation would be possible since it relieves the necessity of delicate temporal overlap of multiple pump pulses.

The previous reports of CW-generated nonlinear signals are mostly achieved using optical cavities with exceptionally high quality factors [117] [118] [35], or waveguides made of nonlinear crystals with millimeter-long integration lengths and carefully-designed phase-matching conditions [121] [122]. When operated close to the phase-matched cavity resonance, these devices can provide very high enhancement factors for efficient generation of second or third harmonic waves. However, the possibility of generating broadband CW nonlinear signals based on a material's intrinsic polariton resonance enhancement has remained unexplored, and it would also hold great potential for further Purcell enhancement in an integrated device.

In this work, we demonstrate the CW generation of SHG and SFG from 2D TMDs and van der Waals heterostructures. By performing CW dual-beam excitation spectroscopy with SHG and SFG signals, we show that second order nonlinear transitions in 1L-TMDs are enhanced when the emission energy becomes resonant with the broadband of high energy exciton states. The peak values of 2nd order susceptibilities for 1L-MoS_2, 1L-$MoSe_2$, 1L-WS_2, and 1L-WSe_2 are all measured to be on the order of 10 nm/V. Compared to SHG, SFG has the unique advantage of allowing independent manipulation of the properties of the two pump photons. We show that SFG from monolayer TMDs can only be generated if the two pump photons have the same circular polarization, which could be a novel method for generating and probing of carriers in selected

valleys [43] [8] [9]. We also demonstrate dual-beam confocal nonlinear imaging of twisted heterobilayer TMDs, where the interlayer electronic coupling in selected regions can be strengthened by the "nano-squeegee" process [123] [124]. The SHG and SFG signals can be imaged together providing a direct visualization of local strength of interlayer electronic coupling.

4.2 Second harmonic generation with continuous-wave excitation

We demonstrate that SHG signals from atomically thin transition metal dichalcogenides can be directly observed under CW laser excitation, with pump irradiance three orders of magnitude lower than conventional schemes employing pulsed laser excitation. The CW-SHG reported in this work shares the same dependence on crystal symmetry and laser polarization as in previous pulsed experiments [36] [37] [116]. Figure 4.1a shows a representative confocal SHG image of mechanically exfoliated WSe_2 flakes on SiO_2/Si substrate excited by an 885 nm CW laser with a power density of 10^{10}W/m^2. Strong CW-SHG intensities are observed in the monolayer and trilayer region where inversion symmetry is broken, while the bilayer region as indicated by the dashed box with a preserved inversion symmetry shows negligible CW-SHG. The inset of Figure 4.1a shows the polarization-resolved CW-SHG when excitation and collection polarizations are parallel, measured at the location indicated by the star marker. The polar angle represents laser polarization direction and is already aligned to the coordinate of the confocal image. The six-fold flower pattern is characteristic of the crystal structure of odd-layered TMDs which belongs to the D_{3h} point group. The only nonvanishing 2nd order susceptibility tensor elements are $|\chi^{(2)}|=\chi^{(2)}_{yyy}=-\chi^{(2)}_{yxx}=-\chi^{(2)}_{xxy}=-\chi^{(2)}_{xyx}$ with y being the armchair direction and x being the zigzag direction [40]. Figure 4.1b shows the emission spectra of CW-SHG with a linewidth as narrow as 4 cm^{-1} which is 50 times narrower than conventional pulsed SHG. With the benefits of ultra-narrow linewidth, CW-SHG could serve a desirable excitation spectroscopy technique for revealing excitonic fine structures such as Moire excitons [12], and probing quantum interference effects at cryogenic temperatures [120]. In this work, room temperature CW-SHG excitation spectroscopy is performed on monolayer WSe_2 and monolayer MoS_2 flakes as shown by Figure 4.1c. The samples for excitation spectroscopy are first mechanically exfoliated onto SiO_2/Si substrates and then transferred onto quartz substrates assisted by a handle layer of hexagonal boron nitride (hBN, typically 20-40 nm thick) which is between the monolayer and the quartz substrate in the final structure. Values of the 2nd order susceptibility $\chi^{(2)}$ are obtained after proper calibration of system collection efficiency and substrate effects as detailed in section 4.7. Note that $\chi^{(2)}$ in this work is defined as the effective nonlinear susceptibility which are related to the sheet nonlinear susceptibility $\chi^{(2),S}$ as $\chi^{(2)}=\chi^{(2),S}/d$ where d is the thickness for monolayer samples. On the sample of 1L-WSe_2, giant enhancement of $\chi^{(2)}$ are observed when twice of excitation energy is at 2.4 eV and 2.9 eV which are matching the resonances of the A' and B' excitons, respectively. The nature of the A' and B' excitons are believed to be the splitting of ground state A and B excitons induced by strong perturbation of Se p-orbitals to W d-orbitals [4]. In addition we notice that both of the two peaks of $\chi^{(2)}$ are further split into two finer peaks separated by about 75 meV, which are not observed in linear optical absorption [4] and may originate from dark exciton states warranting further theoretical investigations. For 1L-MoS_2 samples $\chi^{(2)}$ is greatly enhanced when twice of excitation energy is resonant with the C exciton at about 2.85 eV [13]. Figure 4.1d summarizes the measured values of $\chi^{(2)}$ on the C exciton peaks for monolayer MoS_2 and WS_2, on the B' exciton peaks for monolayer $MoSe_2$ and WSe_2, which gives the highest nonlinear susceptibilities. Shown as comparison are reported $\chi^{(2)}$ values from previous literatures [38] [37] [36] [125] [116] [126] [18] [127]. As a direct result of the strong wavelength-dependence shown in Figure 4.1c, large

variations of $\chi^{(2)}$ values have been previously reported obscuring the practical application of atomically-thin TMDs in nonlinear optical devices. Here we confirm that the peak $\chi^{(2)}$ values of monolayer TMDs are in fact about three orders of magnitude higher than conventional bulk nonlinear crystals such as BBO and $LiNbO_3$ [40] [128], which is also directly corroborated by our observation of continuous-wave pumped SHG.

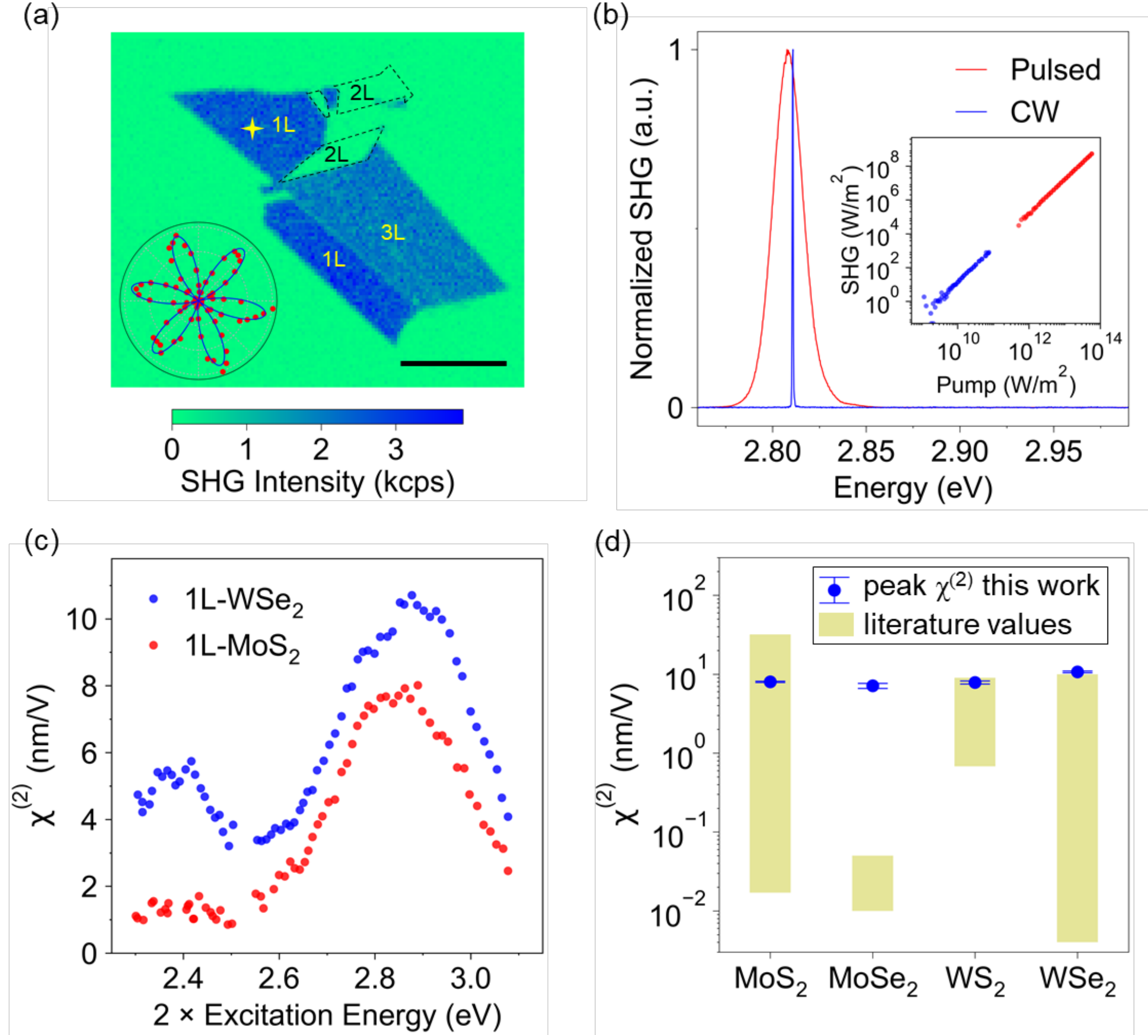

Figure 4.1. Continuous-wave (CW) second harmonic generation (SHG) from atomically thin semiconductors with high second order susceptibilities. (a) SHG confocal image of an exfoliated WSe_2 flake excited with a CW 885 nm laser. Inset shows the polarization-dependent SHG intensity in the parallel configuration and is aligned to coordinate of the image. Red dots are experimental data and blue lines are fitting results based on the $\chi^{(2)}$ tensor of the D_{3h} point group. Scale bar is 10 μm. (b) Ultra-sharp SHG emission spectra with 4 cm^{-1} linewidth excited by CW laser, compared with conventional broad SHG emission excited by pulsed laser. Inset shows the dependence of SHG irradiance on pump irradiance for both CW (blue) and pulsed (red) excitation at 885 nm. For pulsed excitation data the irradiance represents the peak irradiance of a laser pulse. (c) Measurement of effective second order susceptibility $\chi^{(2)}$ for monolayer (1L) WSe_2 and 1L-MoS_2 on quartz substrate. Second order nonlinear cross-sections are greatly enhanced on A' (2.4 eV) and B' (2.9 eV) exciton resonance of 1L-WSe_2 and C exciton (2.85 eV) resonance of MoS_2. (d)

Peak $\chi^{(2)}$ values measured on exciton resonances for 1L-MoS_2, 1L-$MoSe_2$, 1L-WS_2, and 1L-WSe_2. Values reported in literatures are shown for comparison.

4.3 Revealing the role of excitonic emission resonance in nonlinear transitions by sum frequency excitation spectroscopy

Second harmonic generation (SHG) is a special case of the more general sum frequency generation (SFG) process where two photons at different frequencies ω_1 and ω_2 are absorbed by the system generating one photon at the frequency of $\omega_1+\omega_2$ as illustrated in Figure 4.2a. The inset shows a schematic level diagram of the SFG process where |*g*> is the ground state, |*i*> is the intermediate state, and |*e*> is the excited state. The entire SFG process is a combination of three optical transitions as shown by the diagram. Figure 4.2b shows a representative emission spectra from 1L-WSe_2 when excited by two spatially-overlapped CW laser beams at ω_1 and ω_2 together. The two lasers are collinearly polarized in this measurement. Three pronounced peaks at $2\omega_1$, $\omega_1+\omega_2$, and $2\omega_2$ can be observed corresponding to the SHG of ω_1 laser, SFG of the combined excitation, and SHG of the ω_2 laser. The inset of Figure 4.2b shows the dependence of intensities of the three signals on pump irradiance of ω_2, which are clear support for our assignments of the three peaks.

Nonlinear response of two-dimensional semiconductors are highly dependent on excitation energy and strongly enhanced by exciton resonance, as shown by the wavelength dependent CW-SHG in Figure 4.1 as well as conventional pulsed SHG in [15] [18] [38]. In this work we investigate the exciton induced dispersion of the more general sum frequency generation (SFG) where energies of the two individual pump photons can be separately controlled. Figure 4.2c shows the result from dual-beam nonlinear excitation spectroscopy on 1L-WSe_2 on quartz substrate. In this experiment, photon energy $\hbar\omega_2$ is scanned while $\hbar\omega_1$ is kept at a constant value of 1.27 eV. Emission spectra are collected at each combination of ω_1 and ω_2. Since the intensities of different signals have different power dependences as shown in Figure 4.2b, a feedback control loop is implemented to maintain a constant excitation photon flux when the laser at frequency ω_2 is being tuned. Figure 4.2d shows the extracted intensities of the $2\omega_2$ SHG and SFG signals as a function of emission energy. Interestingly, the intensities of $\omega_1+\omega_2$ and $2\omega_2$ are both greatly increased when the emission energies approach 2.4 eV and 2.9 eV, regardless of how the summed energy is distributed between the two contributing pump photons. The 2.4 eV and 2.9 eV resonances correspond to the A' and B' excitons in 1L-WSe_2. Moreover, SFG and SHG shows very similar spectral lineshape for their intensity dependence on emission energy. We also note that the SFG intensity becomes strongly suppressed compared to SHG when emission energy goes above 2.9 eV. In this regime, the excitation energy $\hbar\omega_2$ exceeds the optical band gap at 1.65 eV resulting in the generation of large concentration of excess carriers. The continuous wave ω_2 irradiance for this experiment is about 10^{10} W/m^2. Considering an optical absorption of 5% [129] and a room temperature excited state relaxation time of 300 picoseconds [130], the photo-induced excess carrier density can be estimated to be about 5×10^{13} cm^{-2} when $\hbar\omega_2$ become resonant with the optical gap. The high excess carrier density will induce strong renormalization effects [19] [29] which greatly reduce the excitonic optical oscillator strengths, leading to decreased nonlinear cross section. In our pulsed excitation experiments with photon energies above the optical band gap, monolayer samples are easily burned in ambient environment, since the instantaneously generated excess carrier density is several orders of magnitude higher than the CW excitation scheme as shown previously by Figure 4.1b. The strong renormalization effects suggest that direct excitation

above optical gap is not desired for nonlinear applications. In addition, Figure 4.2 e and f shows the dual-beam nonlinear excitation spectroscopy performed on monolayer MoS_2 samples. Similar to the results obtained from 1L-WSe_2, both SHG and SFG of 1L-MoS_2 are greatly enhanced when emission energies are resonant with the C exciton at about 2.85 eV. In addition, since excitation energy never goes above the optical band gap of 1L-MoS_2 [19] [13], renormalization effects on nonlinear transitions are not observed, leaving the spectral lineshape of SFG and SHG almost exactly overlapping with each other in Figure 4.2f.

With the capability to distinguish between two pumping photons, SFG excitation spectroscopy provides additional insights on how nonlinear transitions are enhanced by exciton states. The 2nd order susceptibility tensor $\chi^{(2)}{}_{ijk}$ can be expressed as [40]:

$$\chi_{ijk}^{(2)}(\omega=\omega_1+\omega_2)\sim\sum_{|i>}\left\{\frac{\mathbf{p}_i^{g,e}\mathbf{p}_j^{e,i}\mathbf{p}_k^{i,g}}{(\omega-\omega_e+i\Gamma_e)(\omega_1-\omega_i+i\Gamma_i)}+\frac{\mathbf{p}_i^{g,e}\mathbf{p}_k^{e,i}\mathbf{p}_j^{i,g}}{(\omega-\omega_e+i\Gamma_e)(\omega_2-\omega_i+i\Gamma_i)}\right\} \tag{4.1}$$

where $\mathbf{p}_k^{i,g}$ is the electric dipole transition matrix element from $|g>$ to $|i>$ with the polarization k, Γ_e (Γ_i) and ω_e (ω_i) are relaxation rates and resonance frequencies for the excited state (intermediate states). The first term in the summation is as sketched by the level diagram of Figure 4.1a, while the second term switches the absorption sequence of ω_1 and ω_2. It can be seen that SFG, which becomes SHG when ω_1 equals ω_2, is a triple resonant process. It has also been suggested that when the excited state $|e>$ is an optically bright exciton, the ω_1 absorption transition has to be mediated by a magnetic dipole transition from the ground state to a 2P-type exciton state, followed by electric dipole transition from this 2P-type intermediate state to the bright exciton state $|e>$ [15]. Our data shows that $\chi^{(2)}$ is not sensitive to variation of ω_1 and ω_2 as long as the sum frequency is constrained, indicating that ω_1 and ω_2 are far away from any strong excitonic resonances within the energy range of our experiments, and that the triple resonance condition is dominated by the (ω-ω_e+$i\Gamma_e$) term. Therefore, combing the analysis above and the strong nonlinear renormalization effects, it will be highly desirable to utilize the excitonic emission resonance for maximizing 2nd order nonlinear efficiencies in 2D semiconductors.

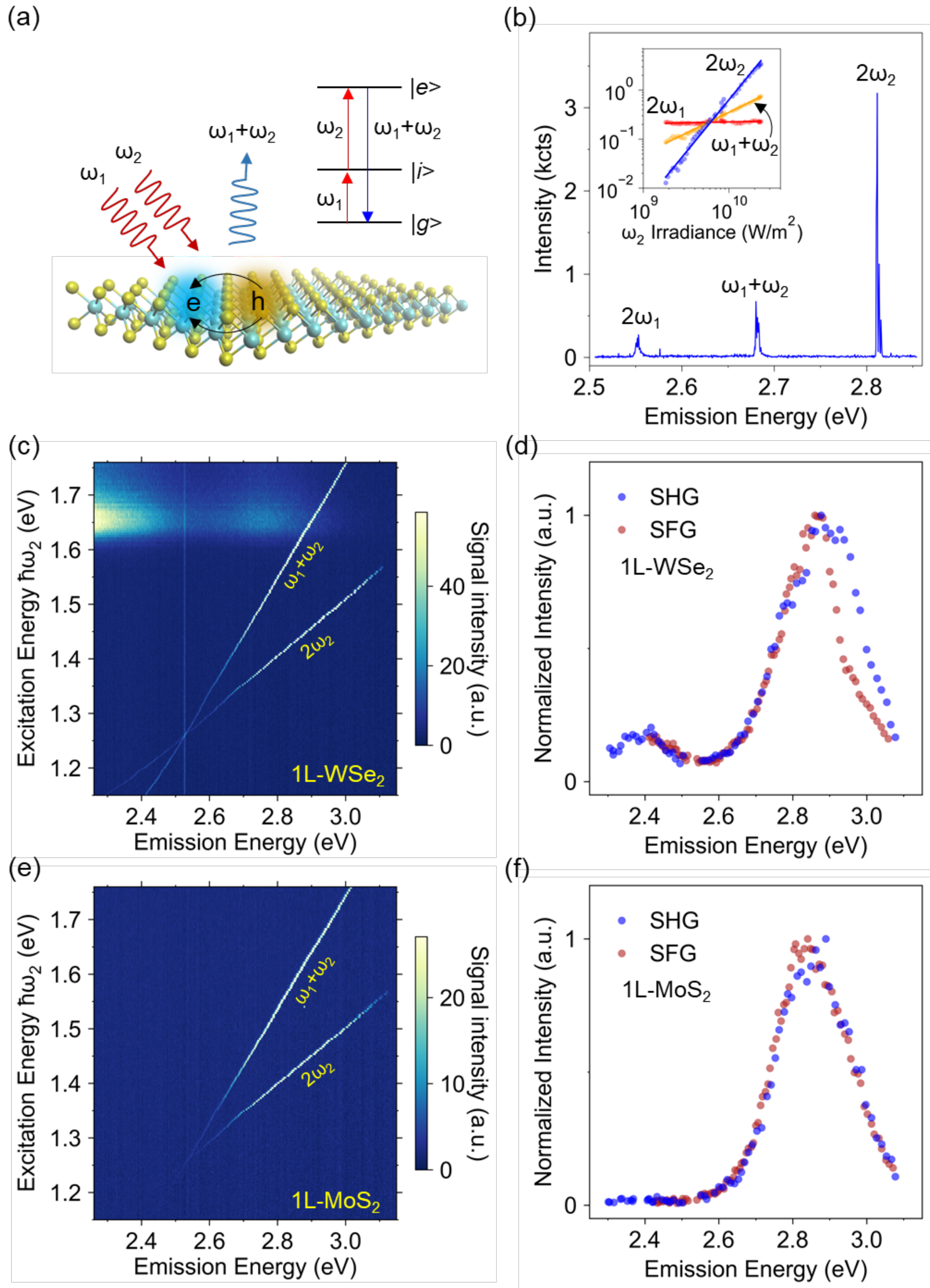

Figure 4.2. Continuous-wave sum frequency generation (CW SFG) and giant enhancement of nonlinear response on excitonic emission resonance. (a) Schematic of SFG process in an excitonic 2D semiconductor where two photons at frequencies ω_1 and ω_2 are combined to generate an

emission photon at $\omega_1+\omega_2$. In the level diagram |g> is the ground state, |i> is the intermediate state, and |e> is the excited state. (b) A typical SFG emission spectra excited by two spatially-overlapped CW lasers. Inset shows the dependence of emission intensity at $2\omega_1$ (red), $\omega_1+\omega_2$ (yellow), and $2\omega_2$ (blue) as a function of the CW excitation irradiance at ω_2. Dots are experimental data and solid lines are powerlaw fitting results with powerlaw coefficients of 0.03, 0.88, and 2.11 for the emission at $2\omega_1$ (red), $\omega_1+\omega_2$ (yellow), and $2\omega_2$ (blue), respectively. (c) Heatmap of excitation energy ($\hbar\omega_2$) dependent SHG ($2\omega_2$) and SFG ($\omega_1+\omega_2$) spectra on 1L-WSe_2. The excitation photon energy ω_1 is kept constant while ω_2 is scanned. Each row shows the color coded emission spectrum excited by a varied combination of ω_1 and ω_2. (d) Intensity of SHG and SFG as a function of emission energy extracted from (c). Both SHG and SFG are enhanced when emission energy is resonant with A' and B' excitons of 1L-WSe_2. Inset shows a schematic level diagram of SFG process. (e) Heatmap of excitation energy dependent SHG and SFG spectra of 1L-MoS_2. (f) Intensity of SHG and SFG as a function of emission energy extracted from (e).

4.4 Linear and circular polarization dependence of sum frequency generation

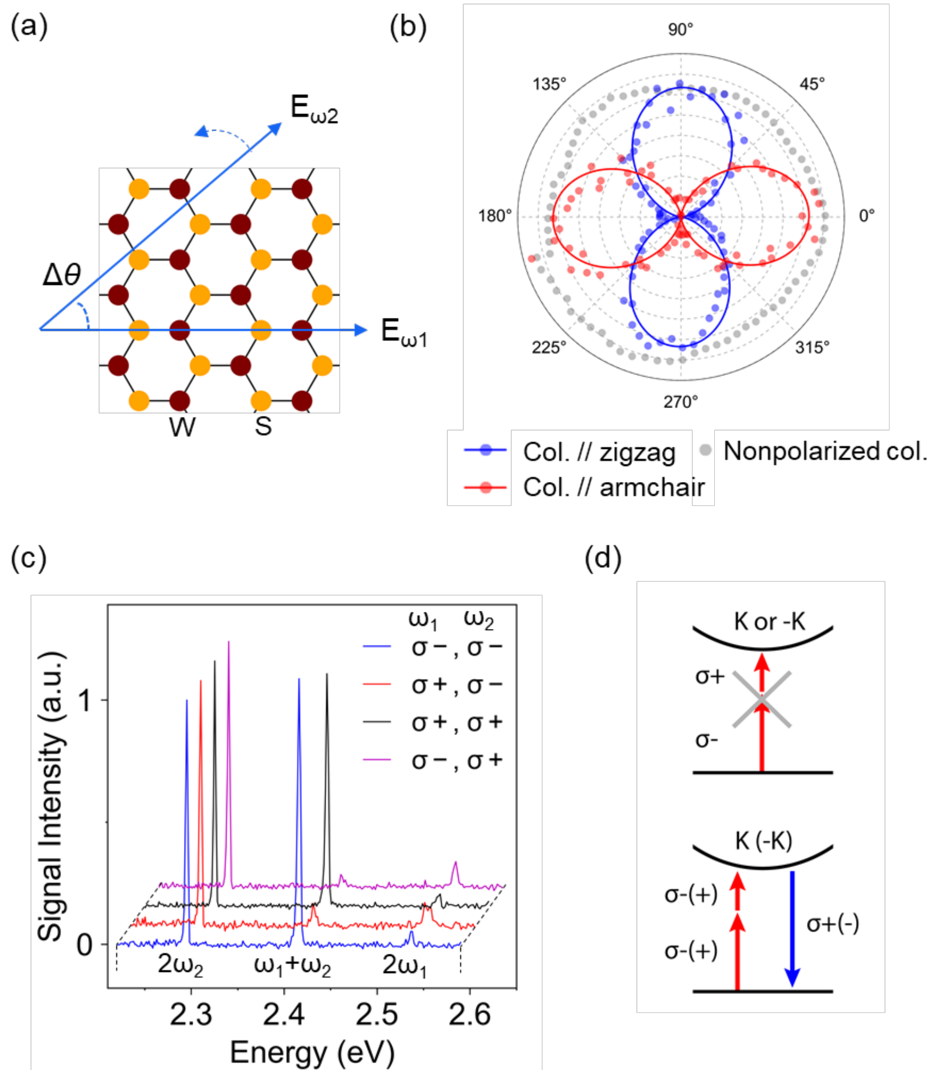

Figure 4.3. Linear and circular polarization dependence of sum frequency generation (SFG). (a) Illustration of monolayer transition metal dichalcogenide crystal and the electric fields of two laser beams for linear polarization experiments. The polarization of ω_1 is kept constant along the armchair direction, while the polarization of ω_2 is dynamically rotated. (b) Intensity of SFG signal as a function of cross-polarization angle $\Delta\theta$ between the two laser beams. Grey dots are for non-polarized collection showing that the SFG intensity remains constant with cross polarization angle. Blue (red) dots are data with collection along the zigzag (armchair) direction of the crystal. Blue (red) lines are fitting with $\sin^2(\Delta\theta)$ ($\cos^2(\Delta\theta)$) functions. (c) SFG spectra excited with different combinations of circular-polarization states of two laser beams, where σ+(-) represents right (left) circularly polarized light. (d) Illustration of the valley-coupled helicity selection rule for sum frequency generation that requires $\sigma_{\omega 1}+\sigma_{\omega 2}-\sigma_{\omega 1+\omega 2}=3N$ with N being an integer.

SFG offers the unique capability of separately controlling the polarization state of the two pump photons which could inspire new optical methods for probing complex crystal orientations and novel designs for polarization optical devices. In the all experiments presented so far the two CW laser beams are kept to be collinearly polarized. Figure 4.3 presents investigation of the dependence of CW SFG on linear and circular polarization states of the two pump beams, using 1L-WS_2 as an example. In linear polarization experiments, the pump beam at ω_1 is polarized along the armchair direction of the lattice, while polarization of the other pump beam at ω_2 is rotated. It's observed that the total SFG intensity does not depend on the cross-polarization angle $\Delta\theta$ of the two beams, as shown by the nonpolarized collection data in the polar plot of Figure 4.3b. However, the SFG electric field components along the armchair direction and zigzag direction are strongly modified by $\Delta\theta$. Using the characteristic form of $\chi^{(2)}$ tensor for D_{3h} space group, it can be derived that:

$$I_y^{\omega_1+\omega_2} = |\chi^{(2)}|^2 I^{\omega_1} I^{\omega_2} \cos^2(2\theta_1 + \Delta\theta) \quad (4.2a)$$

$$I_x^{\omega_1+\omega_2} = |\chi^{(2)}|^2 I^{\omega_1} I^{\omega_2} \sin^2(2\theta_1 + \Delta\theta) \quad (4.2b)$$

where $I_y^{\omega_1+\omega_2}$ and $I_x^{\omega_1+\omega_2}$ represents the SFG intensity along armchair and zigzag direction, respectively, I^{ω_1} and I^{ω_2} are intensities of the two pump beams, and θ_1 is the angle between polarization of pump beam ω_1 and the armchair crystal direction. The solid lines in Figure 4.3b are fitting results of the experimental data with θ_1 being fixed at zero.

Figure 4.3c shows the CW SFG and SHG spectra when the two laser beams have different circular polarizations with σ+(-) representing right (left) circularly polarized light. In this experiment one 976 nm CW laser and one 1080 nm CW laser are used for excitation. No analyzers are used in the collection path. The $2\omega_2$ peak and $\omega_1+\omega_2$ peak are much stronger than the $2\omega_1$ peak because $2\omega_2$ and $\omega_1+\omega_2$ are close to the B exciton resonance of 1L-WS_2 at 2.4 eV [129]. Surprisingly, the SFG signals at $\omega_1+\omega_2$ show a pronounced helicity selection rule: strong SFG can be generated when the two pump beams have the same circular polarization, while very weak SFG are observed when the two pump beams have different circular polarizations. In contrast, the SHG signals are not appreciably affected by circular polarization states of the two pump beams. This observation of SFG originates from the threefold rotational symmetry of the crystal lattice of monolayer TMDs. A general helicity selection rule for SFG can be derived (section 4.7) as:

$$\sigma_{\omega_1} + \sigma_{\omega_2} - \sigma_{\omega_1+\omega_2} = 3N, \;\; N = 0,1,2... \quad (4.3)$$

where σ_{ω_1}, σ_{ω_2}, and $\sigma_{\omega_1+\omega_2}$ are the circular polarizations of the two pump photon and the generated SFG photon. In monolayer TMDs, a direct gap forms at K and -K valleys which are selectively coupled to σ+ and σ- photons for linear optical transitions as a result of inversion symmetry breaking and spin orbital coupling [9] [8]. For second harmonic generation it has been shown that two σ-(+) photons can selectively excite the K (K-) valley and generate SHG with opposite helicity σ+(-) to that of the pump photons [18], which is a special case of Eq (4.3). SFG provides the capability to separately control the helicity of two excitation photons and to directly probe the resulting signal, and thus could be employed for probing valley coherence and inter-valley coupling.

4.5 Imaging interlayer electronic coupling in twisted heterobilayer transition metal dichalcogenides

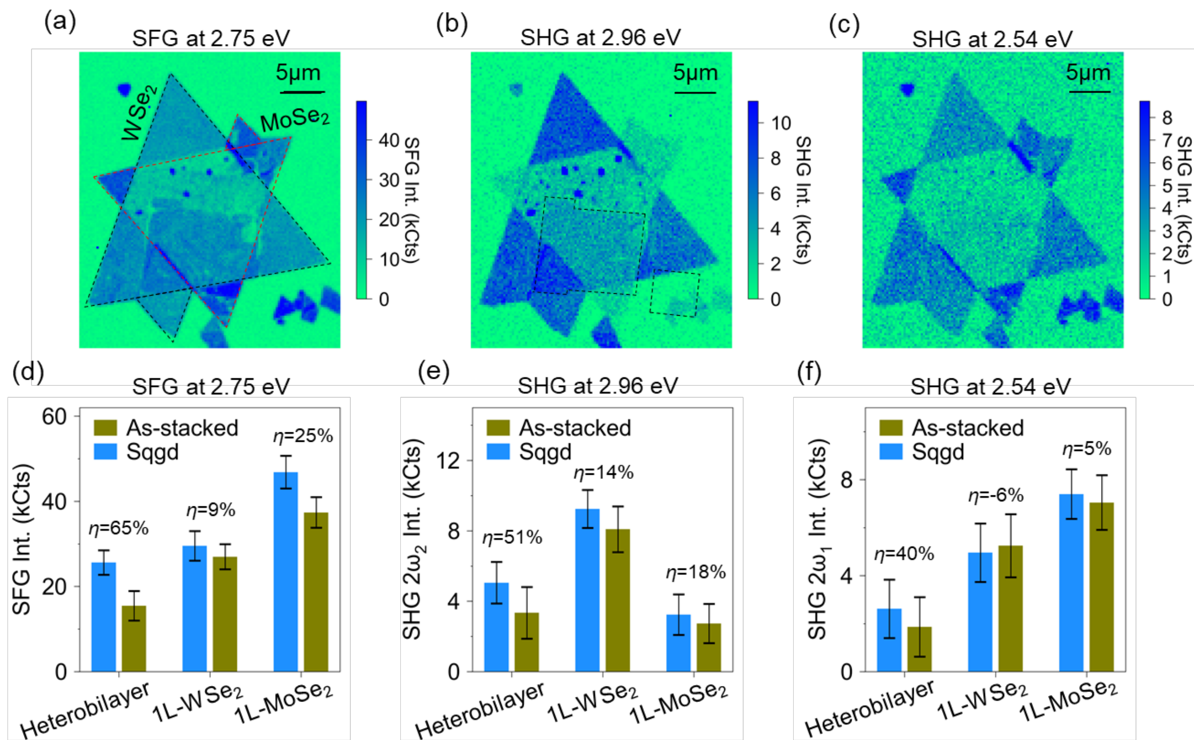

Figure 4.4. Imaging of interlayer electronic coupling in twisted heterobilayer transition metal dichalcogenides. (a, b, c) Dual-beam continuous-wave confocal nonlinear imaging of a 62° twisted heterobilayer of 1L-$MoSe_2$ on 1L-WSe_2, providing maps of simultaneously collected sum frequency generation (SFG, a) and second harmonic generation (SHG, b and c) intensities. The black (red) dashed triangles in (a) illustrates the edges of the 1L-WSe_2 (1L-$MoSe_2$) flakes. The two black dashed boxes in (b) label the regions that have undergone the "nano-squeegeed" process to enhance interlayer electronic coupling. (d, e, f) shows the average intensities of (d) SFG, (e) $2\omega_2$ SHG and (f) $2\omega_1$ SHG collected from different regions of interest. Blue bars are the average intensities from the squeegeed ('sqgd') region and olive bars are averaged intensities from as-stacked un-squeegeed region. The enhancement factors η are the percentage increase of nonlinear emission intensity from as-stacked regions to squeegeed regions.

Finally, we demonstrate the application of CW nonlinear confocal imaging for investigating interlayer electronic coupling in twisted heterobilayer transition metal dichalcogenides. The sample studied is a heterobilayer of 1L-$MoSe_2$ and 1L-WSe_2 grown by chemical-vapor-deposition (CVD), and sandwiched between bottom and top hBN layers. The whole structure is on a 280 nm SiO_2/Si substrate. The twist angle is determined to be $62^o \pm 1^o$ using polarization-dependent SHG technique, and measured to be $61^o \pm 1^o$ based on the angle between major edges of the overlapped flakes. More details on sample characterization are reserved for section 4.7. The slight discrepancy in twist angles determined by the two different methods may be due to local strain effects. Moreover, part of the sample has undergone the "nano-squeegee" process where the tip of an atomic force microscopy (AFM) cantilever is scanned in contact mode with a relatively high normal force. It has been shown that this method can enhance interlayer electronic coupling between TMDs and induce photoluminescence from interlayer exciton states even at room temperature [123]. The two squeegeed regions are outlined by dashed black boxes in Figure 4.4b.

Figure 4.4 shows the confocal hyperspectral imaging of nonlinear signals generated by the sample when excited by two collinearly-polarized spatially-overlapped CW lasers with $\hbar\omega_1$=1.27 eV and $\hbar\omega_2$=1.48 eV. The intensity map at ω_1+ ω_2, $2\omega_2$, and $2\omega_1$ can be simultaneously obtained during one scan, as shown by Figure 4.4 a, b, and c, respectively. For our sample with a twist angle very close to 60°, if interlayer electronic coupling is weak, very low SHG and SFG intensities are expected in the heterobilayer region, as a result of the destructive optical interference of signals generated by the top and bottom TMD layer [131]. This is consistent with our observation in the as-stacked heterobilayer region where the SFG and SHG signal intensities are significantly reduced compared to the monolayer regions. However, the nano-squeegeed heterobilayer region shows significantly enhanced SFG and SHG signals. Specifically, in the SFG image in Figure 4.4a, the squeegeed heterobilayer region shows a high emission intensity at 2.75 eV which is even comparable to the intensity from monolayer regions. In the SHG images in Figure 4.4b and c, the emission intensities at 2.96 eV and 2.54 eV from the squeegeed heterobilayer region are still appreciably stronger than from the as-stacked heterobilayer region, although being much weaker than the SFG emission at 2.75 eV. These observations are quantified by Figure 4.4 d, e, and f which show the average values and standard deviations of the emission intensity data collected in different regions. The enhancement factor η is defined as $\eta=(I^{sqgd}-I^0)/I^0$ where I^{sqgd} and I^0 are the averaged intensities from the squeegeed region and the as-stacked region, respectively. In all images the enhancement factor η for the heterobilayer region are about 40%-60%. The effect of nano-squeegee process on interference of optical waves may be neglected since pressing the heterobilayer with an AFM tip is not expected to induce a large change in sample thickness compared with the optical wavelength. Therefore, we attribute the enhanced nonlinear emission to be originated from interlayer excitonic resonance which is strengthened by the squeegee process. Furthermore, the strong dependence of nonlinear emission intensity on emission energy suggests that 2.75 eV may be more close to a high energy interlayer exciton state which resonantly enhances nonlinear emission. Based on the clear contrast observed from confocal imaging, we envision that a full excitation spectroscopy study of twisted heterobilayer samples can provide critical information on interlayer exciton states.

4.6 Conclusion

In conclusion, continuous-wave generation of second harmonic and sum frequency signals are realized with atomically thin transition metal dichalcogenides and van der Waals

heterostructures, with pump irradiance about three orders of magnitude lower than conventional pulsed generation. The strong nonlinearity originates from the strong exciton effects in these materials. We demonstrate the application of CW SFG for excitation spectroscopy with the capability of controlling energy and polarization of individual pump photons independently, which were not possible with previous SHG experiments. We find that both SFG and SHG processes are greatly enhanced when the emission rather than excitation energy becomes resonant with high energy exciton states in monolayer TMDs, and reveal the unique helicity selection rule that forbids SFG generation from two photons with opposite circular polarizations. In addition, confocal CW dual-beam imaging is performed on twisted heterobilayer TMDs to provide simultaneous mapping of nonlinear signals emitted at different energies, revealing the local strengths of interlayer electronic coupling in van der Waals heterostructures.

4.7 Additional contents

4.7.1 Accounting for interference local field effects on nonlinear characterization and excitation spectroscopy

Atomically thin layers of transition metal dichalcogenide (TMD) samples are typically mechanically exfoliated on to SiO_2/Si substrates which provide higher optical contrast for easy and fast identification of monolayer, bilayer and trilayer flakes of interest under microscope. Significant interference effects will be induced by the stratified substrate in the wavelength range of our experiments, as sketched by Figure 4.7.1. For linear photoluminescence excitation spectroscopy [19] such interference effects can be reliably corrected. However, for broadband nonlinear excitation spectroscopy, the signal wavelength changes with the pump wavelength, and both of them are strongly affected by interference. SHG intensity scales with the square of excitation power, so the interference effect on pump beam will be amplified as well. Moreover, tightly-focused laser beams generated by high numerical aperture (NA) objectives are desired for nonlinear excitation. For our experiments objective with NA=0.95 is used. This also makes it inaccurate to use plane wave approximation for the calculation of interference-induced local field factor. Therefore, we use finite difference time domain (FDTD) numerical simulation with Lumerical software to calculate the SHG local field factor on different substrates as shown by Figure 4.7.1b. The total local field factor ρ_{tot} is the product of pump local field factor ρ_{pump} and collection local field factor $\rho_{col.}$ as defined below.

$$\rho_{tot} = \rho_{pump}\rho_{col.}$$

$$\rho_{pump} = \left|\frac{E_{loc}^{\omega}}{E_{inc}^{\omega}}\right|^4, \qquad \rho_{col.} = \frac{P_{col.}^{2\omega}}{P_{emit}^{2\omega}}$$

The pump (excitation) local field factor is calculated as the fourth power of the ratio between electric field intensity of the incident wave into the objective and the local electric field intensity right on top of the substrate. In order to calculate the collection local field factor, dipole sources are placed on top of the substrate, and the ratio between the power collected within the angle of NA=0.95 and the total radiating power is calculated as the collection local field factor. With these, the relationship between SHG irradiance and pump irradiance can be expressed as:

$$I^{2\omega} = 4\eta k_{\omega}^2 \,|\, \chi^{(2)} \,|^2\, \rho_{tot} (I^{\omega})^2$$

Where η is the impedance of surrounding environment (air), k_ω is the wavevector of pump beam in air, and $|\chi^{(2)}|$ is the absolute value of 2nd order susceptibility tensor elements. Here I^{ω} and $I^{2\omega}$ are the pump and SHG irradiance measured in experiments, after the calibration of system efficiency. We notice that when plane wave approximation and Fresnel equations are for calculating local field enhancement, the above equation is consistent with that derived in [132]. The above equation is also used for reporting quantitative values of $|\chi^{(2)}|$ measured on quartz substrates.

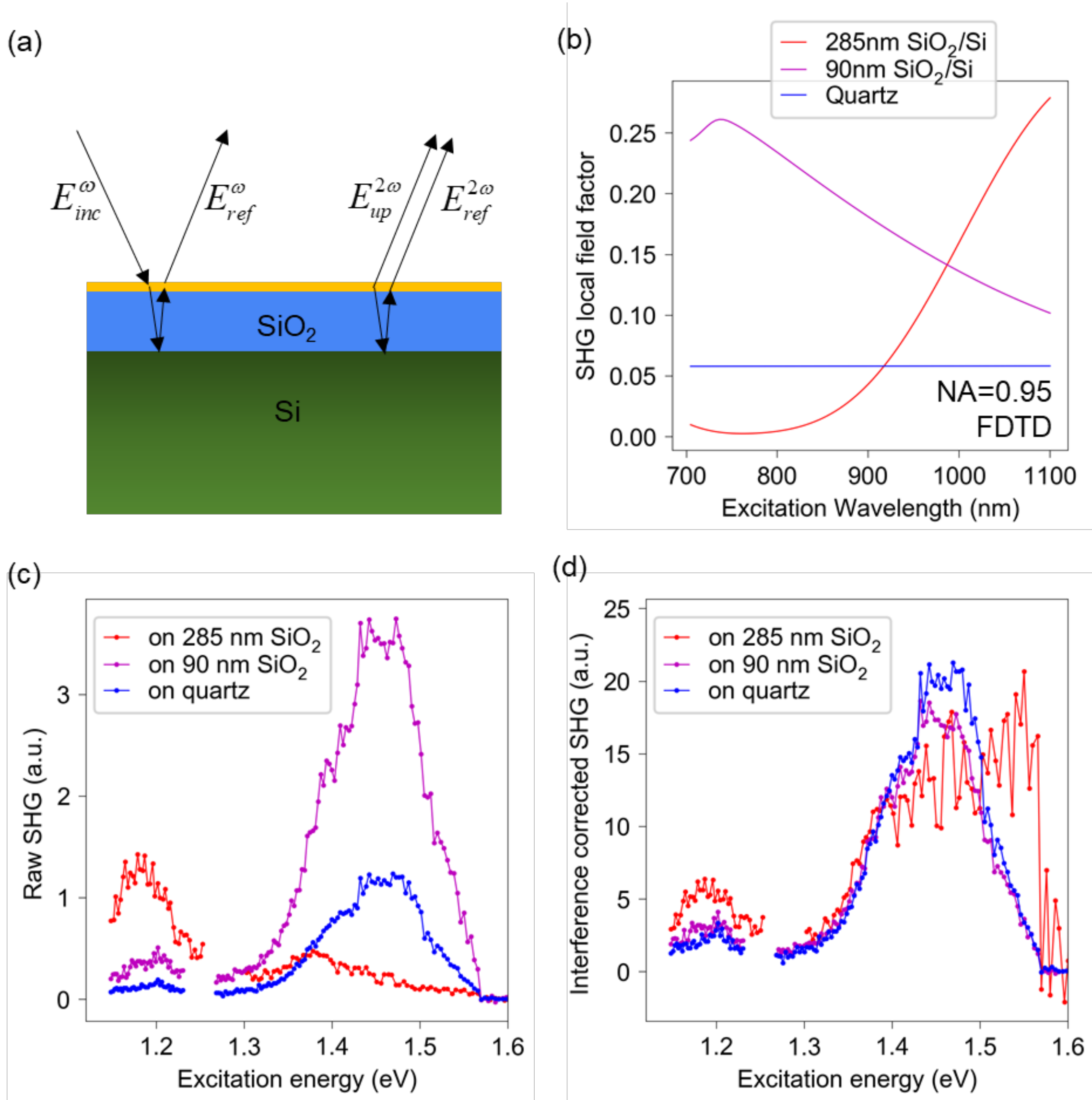

Figure 4.7.1. Accounting for substrate interference effects on nonlinear excitation spectroscopy. (a) Illustration of the excitation and collection interference effects induced by a stratified substrate where the atomically thin layers (orange color) are exfoliated. The net interference effects at ω and 2ω gives the SHG local field factor. (b) The SHG local field factor for the experimental setup with a NA=0.95 objective, calculated by finite difference time domain (FDTD) numerical method. (c) Raw data of SHG excitation spectra for 1L-WSe_2 measured on different substrates. The sample on quartz is encapsulated by thin (~10nm) hexagonal boron nitride (hBN) layers. (d) SHG excitation

spectra obtained after applying interference local field factor corrections on the raw data. For (c) and (d), the SHG intensities for all spectra are scaled with an arbitrary but the same number.

As a demonstration of successful interference correction, Figure 4.7.1 c shows the raw data of SHG excitation spectra measured on 285 nm and 90 nm SiO_2/Si substrates as well as bulk quartz substrates, and Figure 4.7.1 d shows the interference-corrected SHG excitation spectra. We can see that data measured for samples on 90 nm SiO_2/Si and quartz substrates show large differences in raw SHG intensity, and this can be well accounted for by our FDTD calculation of local field factor. However, the interference effects induced by 285 nm SiO_2/Si substrates are extremely strong, with the local field factor varying across two orders of magnitude as shown in Figure 4.7.1b, which imposes large uncertainties in interference correction. As a result, for quantitative nonlinear measurements and excitation spectroscopy, thin SiO_2/Si substrate or bulk quartz substrate should be used.

4.7.2 Layer-dependent continuous wave SHG and SFG

SHG and SFG are both 2nd order nonlinear processes which are expected to vanish in centrosymmetric crystals, such as even layer TMDs, as shown by Figure 4.7.2.

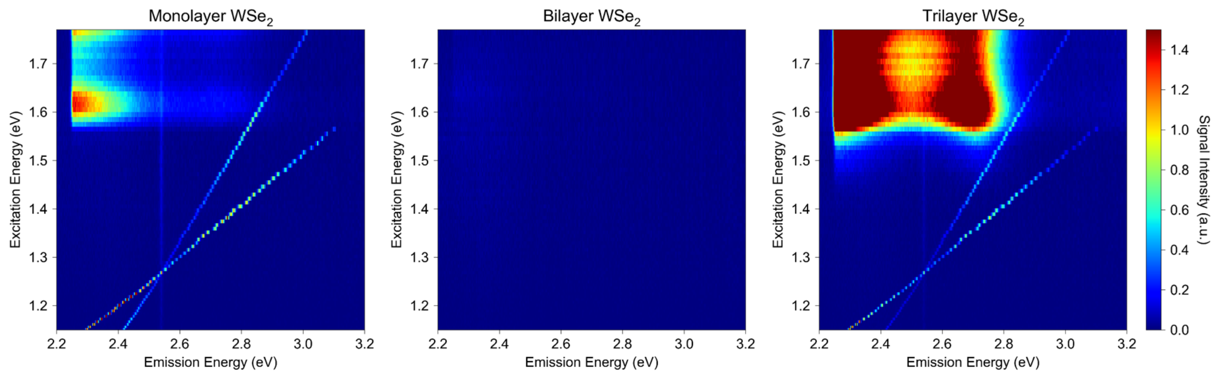

Figure. 4.7.2. Continuous-wave dual-beam excitation spectroscopy on monolayer, bilayer and trilayer WSe_2.

4.7.3 Second order helicity selection rules in monolayer TMD crystals

The unique crystal structure of TMDs impose an interesting helicity selection rule for second order nonlinear transitions. As a result of the threefold crystal rotational symmetry, the matrix elements will be conserved under $\widehat{C_3}$ operation giving that:

$$\sum_{|i>} < v | \mathbf{p}^*_{\pm}(\omega_S) | c > < c | \mathbf{p}_{\pm}(\omega_2) | i > < i | \mathbf{p}_{\pm}(\omega_1) | v >$$

$$= \sum_{|i>} < v | \widehat{C_3^\dagger} \widehat{C_3}\, \mathbf{p}^*_{\pm}(\omega_S) \widehat{C_3^\dagger} \widehat{C_3} | c > < c | \widehat{C_3^\dagger} \widehat{C_3}\, \mathbf{p}_{\pm}(\omega_2) \widehat{C_3^\dagger} \widehat{C_3} | i > < i | \widehat{C_3^\dagger} \widehat{C_3} \mathbf{p}_{\pm}(\omega_1) \widehat{C_3^\dagger} \widehat{C_3} | v >$$

$$= e^{-i\frac{2\pi}{3}(-\sigma_S + \sigma_2 + \sigma_1)} \sum_{|i>} < v | \mathbf{p}^*_{\pm}(\omega_S) | c > < c | \mathbf{p}_{\pm}(\omega_2) | i > < i | \mathbf{p}_{\pm}(\omega_1) | v >$$

Here σ_1, σ_2, and σ_S represents the angular momentum of the two pump photons at ω_1, ω_2, and the sum frequency photon at ω_S, respectively. In the derivation above, we used the rotational transformation of the momentum operators and the Bloch eigenstates, shown as following.

$$\widehat{C_3}\,\mathbf{p}_\pm \widehat{C_3^\dagger} = e^{\mp i\frac{2\pi}{3}}\mathbf{p}_\pm$$

$$\widehat{C_3}\,|\phi> = e^{-i\frac{2\pi}{3}m_\phi}\,|\phi>$$

Therefore, in order to have a non-vanishing $|\boldsymbol{\chi}^{(2)}|$, the helicity selection rule requires that

$$\sigma_1 + \sigma_2 - \sigma_S = 3N,\ \ N = 0,1,2,...$$

This means SFG can only be pumped by two photon with the same spin, and then generating a sum frequency photon with opposite spin. When the sum frequency photon is in resonance with ***K*** and ***K'*** valley carriers, this SFG helicity selection rule further implies the locking of nonlinear processes with valley degree of freedom.

4.7.4 Determination of the twist angle of heterobilayer sample with polarization dependent SHG

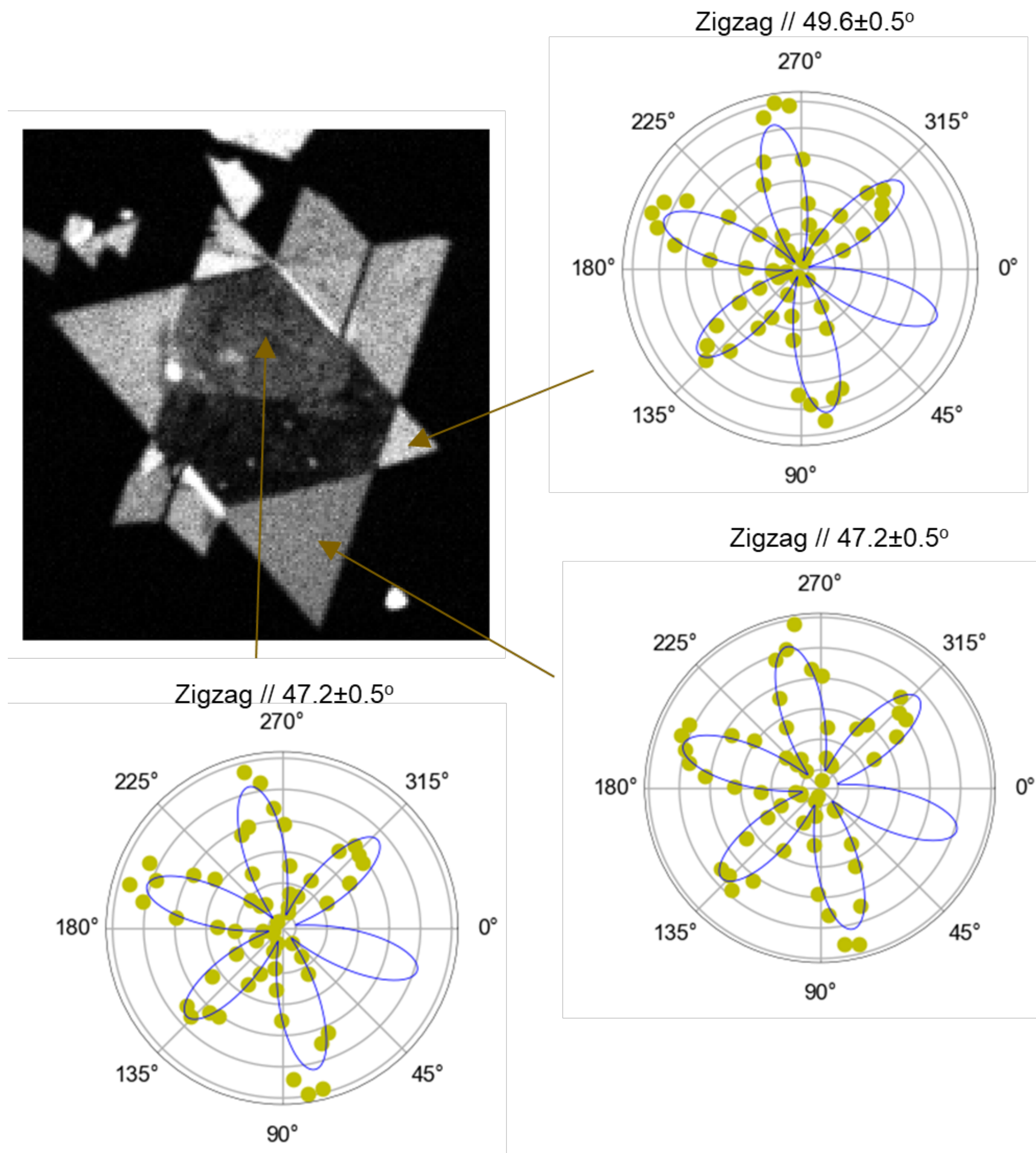

Figure. 4.7.3. Confocal SHG imaging and polarization dependent SHG measured at different locations on the twisted heterobilayer sample of 1L-$MoSe_2$ on 1L-WSe_2 as investigated in Figure. 4.4. The twist angle is determined to be 62.4±0.5°. Note that only with SHG data on bare monolayer flakes we cannot tell whether it's 62.4±0.5° or 2.4±0.5°. This is further determined by the darkness of the as-stacked (without being squeegeed) heterobilayer region indicating a destructive interference between SHG generated by the two layers. Instead, if twist angle was 2.4±0.5°, the as-stacked heterobilayer region would be brighter than monolayer regions.

Chapter 5 - Two-dimensional materials and heterojunctions for applications in microelectromechanical systems (MEMS)

5.1 Overview

This section includes two cases of practical device applications of two-dimensional materials and heterostructures in MEMS. These devices are not limited to the demonstration and utilization of exciton properties, but involve a combination of general mechanical, electrical, and optical properties. In the first part, we introduce a solar-blind ultraviolet (UV) photodetector using graphene as a transparent electrode on top of microcrystalline diamond grown by hot filament chemical vapor deposition (HFCVD). A facile fabrication method is developed to peel-off wafer-scale layers of microcrystalline diamond and transfer them onto a flexible substrate, and then transfer large area of CVD-grown monolayer graphene onto the diamond thin film as a transparent top electrode. The carbon-carbon heterojunction formed by the graphene layer and the diamond layer has a favorable band alignment for separating photo-excited carriers. Moreover, with analytical modeling we show that the interface states allows efficient photo-induced modulation of heterojunction barrier height which provides very high photocurrent sensitivity. The graphene/diamond photodetectors are only sensitive to UV photons with energies higher than the band gap of diamond. Therefore they're very promising for outdoor MEMS sensing which requires minimization of solar background noise, such as the detection of corona discharge from high voltage power lines. In the second part, we describe MEMS strain sensor devices made using the electron gas (2DEG) formed at AlGaN/GaN interface. In this case a quantum well forms at the interface between AlGaN/GaN due to piezoelectric effect, and the electrons are confined within this quasi two-dimensional quantum well extending about ten nanometer range in the vertical direction, forming the conduction channel of the high electron mobility transistor (HEMT). The drain current of HEMT is expected to increase with increasing tensile strain, but we found quite the opposite trend after measuring several tens of devices that we fabricated. We further notice that our observation of the opposite strain-sensing trend and improved sensitivity are also confirmed by later works. Moreover, our devices show improved strain sensitivity despite the opposite trend, indicating that a new mechanism could be playing a role in improving HEMT for strain sensing. By combining high-low frequency capacitance-voltage measurements and device modeling, we determined the new mechanism to be piezoelectricity-induced variation of gate Schottky barrier height. Overall the two examples described in this chapter demonstrate the promising potential of using atomically thin semiconductors for MEMS sensors. With the more recent emergence of van der Waals heterostructure devices and the growing capability to grow and fabricate large-area and even wafer scale transition metal dichalcogenide materials and devices, more opportunities are expected to arise for pushing atomically thin semiconductors towards practical MEMS applications.

5.2. A flexible solar-blind UV detector based on graphene-microcrystalline diamond heterojunctions

Heterojunctions between graphene and conventional semiconductors such as Si [133] [134] [135], GaAs [136], Ge [137], etc. have been extensively investigated recently for optoelectronic applications in photodetectors and solar cells. These systems are realized by the direct transfer of CVD-grown or exfoliated graphene films onto the semiconductor substrates as transparent electrodes to form Schottky junctions. On the other hand, the advancement of material

technologies over the past decades has inspired research in several wide bandgap semiconductors such as GaN, GaP, ZnO, 4H-SiC, and diamond for ultraviolet (UV) sensing applications [138] [139] [140]. These wide bandgap semiconductors only respond to high energy UV photons without being affected by low energy illumination noises from the environment. Among these materials, ZnO, 4H-SiC, GaN and GaP are considered as "*visible blind*" since they respond to part of the solar radiation arriving at the earth's surface (280nm-400nm). On the other hand, diamond has an ultra-wide bandgap (5.45eV) for a "*solar-blind*" material as it only responds to radiation shorter than 230nm, where solar radiation is completely absorbed by the ozone layer of the earth's atmosphere. Therefore, for diamond photodetectors, the background noises from solar radiation are essentially zero [141].

Experimental studies on the heterojunction between graphene and diamond have been difficult due to complications in the graphene transfer process [142]. There are four types of diamond films, including single-crystalline diamond, microcrystalline diamond (MCD), nanocrystalline diamond and ultrananocrystalline diamond [143]. Single-crystalline diamond is the ideal choice for the graphene/diamond heterojunction for its exceptional optical, electrical and thermal properties [144]. However, the manufacturing cost is very high since single-crystalline diamond is synthesized on limited substrates with either lattice matching crystalline structures with diamond or on natural diamond by the homoepitaxy chemical vapor deposition process. Microcrystalline diamond, on the other hand, can be deposited on silicon and SiO_2 substrates while maintaining good physical properties with large grain sizes. However, the surface roughness of as-grown diamond films is usually on the order of hundreds of nanometers. Previously, it has been demonstrated that graphene can be transferred onto well-polished ultrananocrystalline diamond [142] composed of small single crystalline particles with degraded optical property. Here, a simple yet practical method has been developed to circumvent the surface roughness problem for the realization of the graphene-MCD heterojunction. Specifically, large-scale MCD thin films have been peeled off directly from the growth silicon substrate to expose their back surfaces which are smooth originating from the flat growth substrates. The grain boundaries of the MCD films are mostly in the direction perpendicular to the film surface such that the vertical device structure is more favorable as compared with the conventional lateral device structure layout based on interdigitated electrodes [145] [146] [147] [148]. In the vertical devices, carriers are transported in the direction parallel to the diamond grain boundaries to minimize losses due to boundary scatterings [149]. In this work, we are able to construct a flexible, sandwich-structured, solar-blind UV detector based on microcrystalline diamond using graphene and metal as the top and bottom electrodes, respectively, to allow carriers to move along the vertical direction in the device.

Figure 5.1a is the conceptual illustration of the overall device structure. A 2μm-thick MCD layer is sandwiched between a monolayer graphene, which serves as the top electrode, and an annealed metal electrode (Ti/Au – 150nm/300nm) as the bottom electrode. A contact pad (yellow color in the figure) made of SiO_2/Ti/Au with the size of 2mm by 5mm is deposited on the top surface of the MCD film. For electrical measurements, the bottom electrode (Ti/Au) is kept grounded while the bias voltage is applied to graphene via the SiO_2/Ti/Au contact pad. Figure 5.1b sketches the band diagram of the device when a negative bias voltage is applied to the MCD under UV illumination. Both Ec, Ev are the conduction and valence bands of the diamond film, respectively and E_{FS} and E_{FG} correspond to the Fermi levels of diamond and graphene, respectively. Since graphene is transparent to UV light [150], incident photons with an energy (*hv*) higher than the bandgap of MCD (5.45eV) can excite the inter-band transitions to generate electron-hole pairs

which are then separated by the applied electric field and collected by top and bottom electrode, respectively. Figure 5.1c shows the optical photo of the flexible MCD/metal/tape film being peeled off from the growth substrate. The film is 20 x 30 mm^2 in size and is bended by two fingers with a radius of curvature of roughly 14mm.

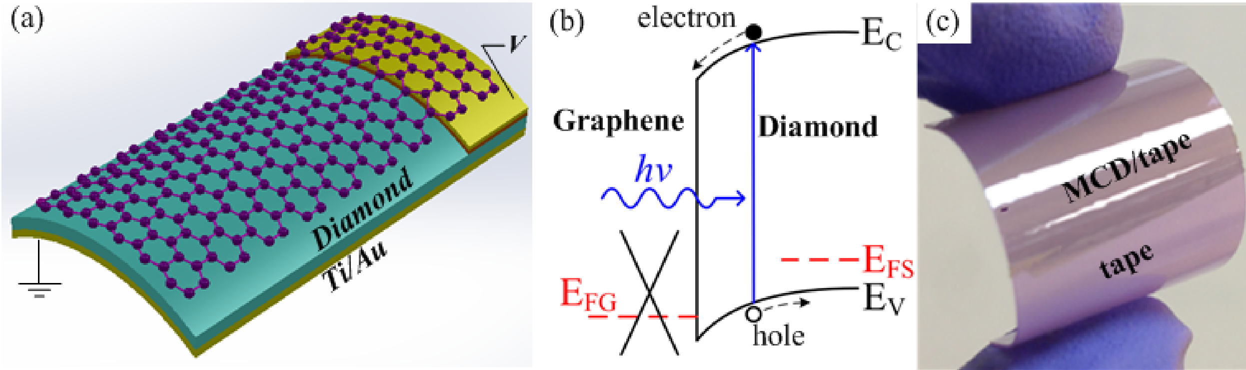

Figure 5.1. (a) Conceptual illustration of the solar-blind UV detector based on the graphene-microcrystalline diamond heterojunction. (b) Schematic band diagram of the system under UV illumination. (c) Optical photograph of the flexible MCD/metal/tape bended between two human fingers.

The device fabrication process is illustrated in Figures 2a and 2b. First, MCD (blue-color) is grown on a 4-inch silicon wafer with a 1µm-thick, thermally grown oxide layer on top. Diamond nucleation seeds with the size of about 10nm are first spin-coated on the silicon substrate. The hot-filament chemical vapor deposition (HFCVD) process is conducted in a reactor chamber with 200 sccm of CH_4, 5,000 sccm of H_2, 10,000 sccm of N_2, and a reaction temperature of 720 °C. Boron is introduced as the p-type dopant source via a controlled Trimethylboron (TMB) into the reaction gas. Two types of MCD films, with and without TMB - denoted as pMCD and iMCD, respectively, have been grown and the field-effect measurements have been carried out to estimate the doping concentrations for the pMCD film as $4\times10^{17}cm^{-3}$ and the iMCD film as $5\times10^{15}cm^{-3}$, respectively. The resulting grain size of the 2□m-thick diamond films is approximately 1µm. The Ti/Au (150/300nm) layers are evaporated afterwards on the front side. In order to achieve ohmic contact, the wafer is subsequently annealed in forming gas at 500ºC for 45mins following the standard recipe [151]. A 80-90 □m-thick tape (Nito™ Revalpha thermal release tape 3195V, or 3M™ XYZ conductive tape 9713) is firmly applied and flattened onto the front side. Electrical contact areas are opened and filled with silver paste on the tape and the whole structure (tape, metal layer, and diamond film) is mechanically peeled off, as shown in Figure 5.2a. The success of this mechanical peeling process relies on the internal residual stress due to the mismatch of the thermal expansion coefficients of the diamond film and silicon substrate and the poor adhesion force between them. It is found that the MCD/metal/tape film from a whole 4-inch in diameter can be peeled off and transferred onto a new wafer (Figure 5.6a). Furthermore, the exposed backside of the MCD film appears to be very smooth under naked eyes and microscope (Figures S1b and S1c).

After these steps, the MCD/metal/tape film is placed on top of a flexible polymer substrate and a layer of SiO_2/Ti/Au (500/20/100nm) is evaporated by electron beam evaporation with a shadow mask to construct the electrical contact pad for the graphene, in order to avoid direct

electrical shorting between the bias voltage and the MCD film. A monolayer graphene is then transferred onto the back side of the MCD film by the widely used wet-transfer method [152]. The CVD-grown graphene (Graphene Supermarket, on copper foil) is first spin-coated with 300nm-thick PMMA and then placed on the $FeCl_3$ solution (1mol/L in DI water) to etch the Cu foil and further cleaned with the modified RCA process [152]. After being rinsed in DI water for several times, the PMMA/graphene film is scooped out of the DI water using the MCD/metal/tape structure. After these steps, Figure 5.2b applies. The optical microscope image of the transferred graphene in Figure 5.2c is taken with the illumination of a white light LED and the optical contrast is good enough for graphene identification as the area covered by graphene appears darker as compared to the exposed MCD in the scratched area on the top-right corner. The transferred graphene is free of macroscopic contaminations. Figure 5.2d shows the SEM image of the boundary between the transferred graphene and exposed MCD. In the region covered by graphene, texture of the nanometer-sized diamond nucleation seeds can be observed, indicating an intimate and conformal coverage of graphene on MCD.

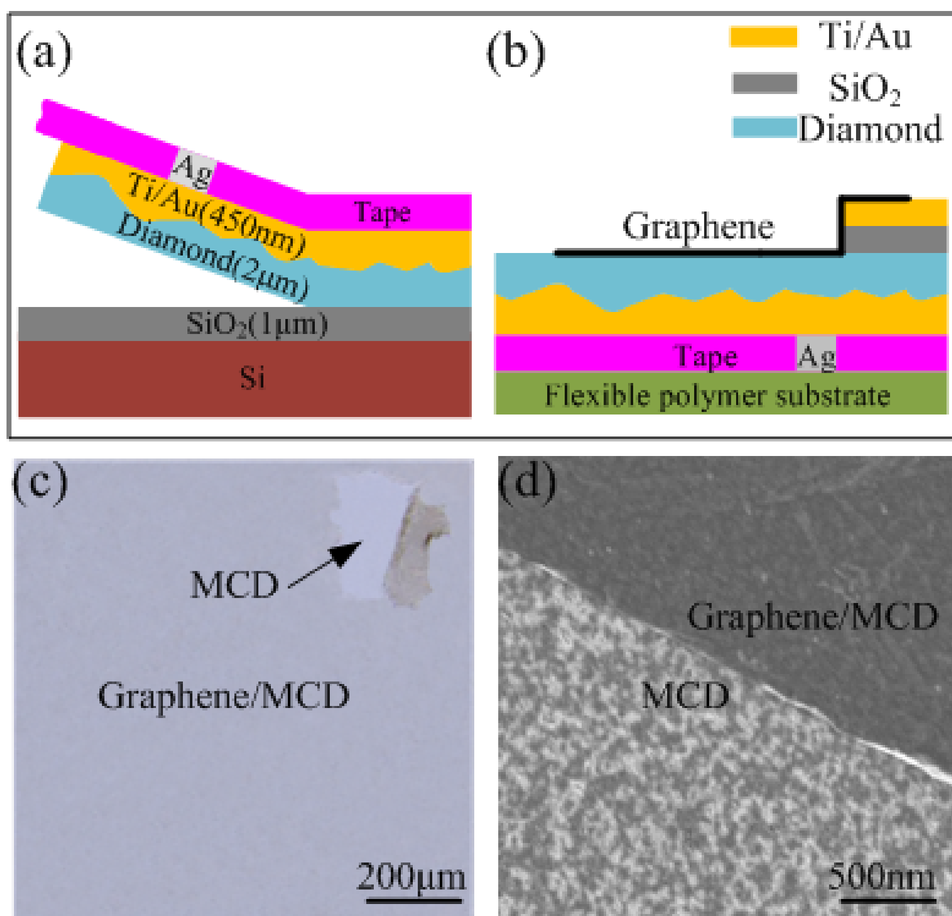

Figure 5.2. (a-b) Illustration of the layer transfer process for making the graphene/MCD heterojunction. Yellow, blue, purple, grey and sliver color represent metal, MCD, tape, SiO_2 and silver, respectively. (c) Optical microscope photo and (d) SEM image after the graphene transfer process onto the back side of MCD.

It's critical to use the back side of the MCD film for the graphene transfer process as it is very smooth. The front side of the MCD film have large micrometer-sized diamond crystals as

seen in Figure 5.3a with a measured RMS (root mean square) surface roughness of 155nm in Figure 5.3c. Another important factor is the surface hydrophilicity of the target substrate [152] as there is significant amount of residue water in the graphene transfer process. A hydrophilic substrate is desirable since the spread of water resulting in flat and breakage-free PMMA/graphene films. Specifically, the water contact angles on the front and back side of the MCD film has been measured as shown in Figure 5.3d. It's observed that the contact angle of ~67° for the front surface is much larger than the smooth back surface of ~33°. Figure 5.3d shows the measured RMS surface roughness for the back side is as low as 7nm. When the graphene film is directly transferred onto the front side, results show the breakage of graphene in Figure 5.6e. In the high magnification SEM image (Figure 5.6f), graphene is punctured apart by the sharp crystal edges and corners of the diamond crystals. The iMCD thin film has a sheet resistance of ~150 kΩ/sq as measured by the four-point probe method without measurable changes after the graphene transfer process. On the contrary, the measured sheet resistance drops to only 130 Ω/sq after the graphene transfer process onto the back side of the diamond film.

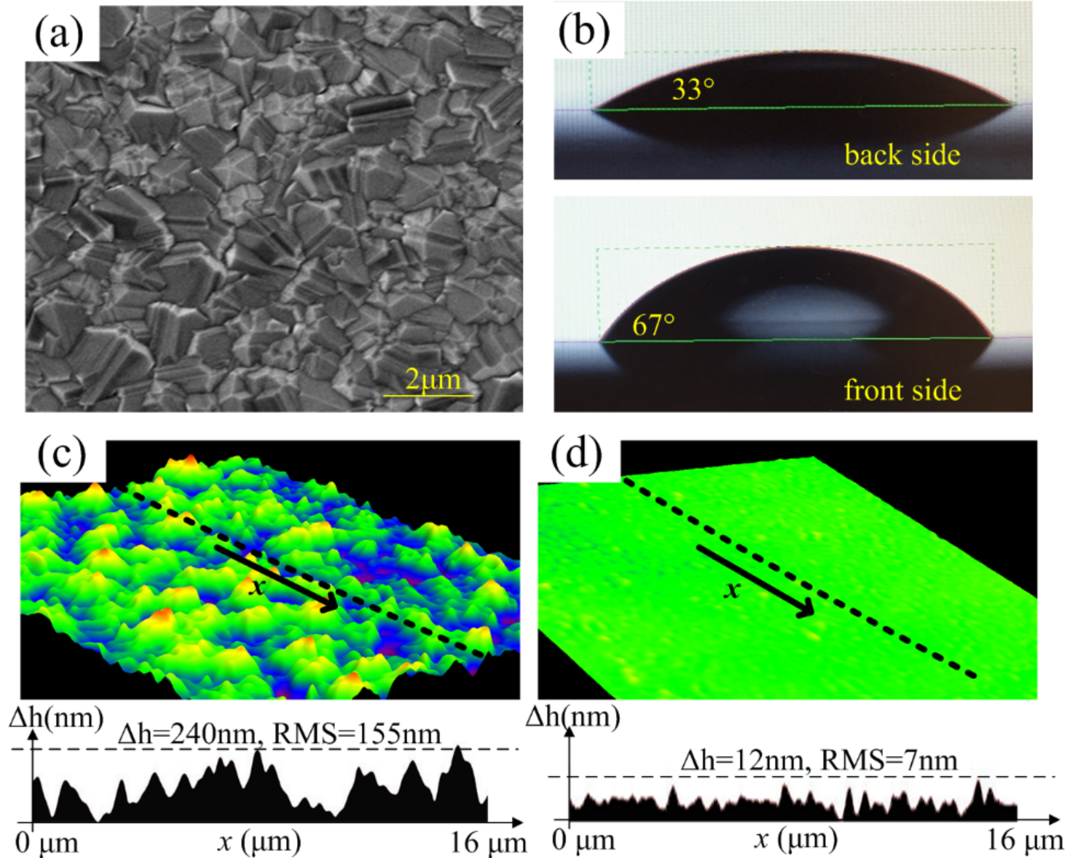

Figure 5.3. (a) SEM image of the rough front surface of the MCD. (b) Water contact angles on the back and front side of the MCD film. Confocal microscope photo of (c) front side and (d) back side of the MCD film in a 20μm by 20μm area. The bottom panels show the surface roughness profile measured along the dashed lines.

Raman spectroscopy (532nm and 1mW) has been performed to study the graphene/iMCD and graphene/pMCD heterojunctions with a spot diameter of ~1μm. The black curve in Figure

5.4a shows the characteristic G and 2D peaks of graphene while the defect-induced D peak is invisible. The 2D peak can be well fitted by a single-peak Lorentzian function with a full width half magnitude (FWHM) of $30cm^{-1}$ (Figure 5.4b) with a much larger intensity as compared with the G peak (I_{2D}/I_G~4). All these features imply that the transferred graphene is monolayer with low defect density [153]. The blue and red curve in the middle of Figure 5.4a shows the Rama spectrum of bare pMCD substrate and the graphene/pMCD heterojunction, respectively. For the bare pMCD sample, a strong and sharp peak at $\sim 1332cm^{-1}$ is observed as the sp^3 bonds of diamond [150]. There are also shoulder-like bands around $1200cm^{-1}$ and $1580cm^{-1}$. The former one is the vibrational mode due to the embedded boron atoms in sp^3-bonded carbon atoms [154], and the latter one can be attributed to the sp^2 phases due to the grain boundaries of MCD [155]. The spectrum of the graphene/pMCD heterojunction inherits the sp^3 peak, $1200cm^{-1}$ band and $1580cm^{-1}$ band from that of the bare pMCD film. Additionally, strong G and 2D peaks are observed due to the graphene film. The blue and green curve on the top of Figure 5.4a are the Raman spectra of the bare iMCD film and graphene/iMCD heterojunction, respectively. For these two samples the $1200cm^{-1}$ bands are absent since boron dopants are not introduced while the $1580cm^{-1}$ band and sp^3 peak are still present. The graphene/iMCD spectrum shows additional G and 2D peaks as compared to the spectrum from the bare iMCD. The intensity ratio I_{2D}/I_G for both heterojunctions are around 3~4.

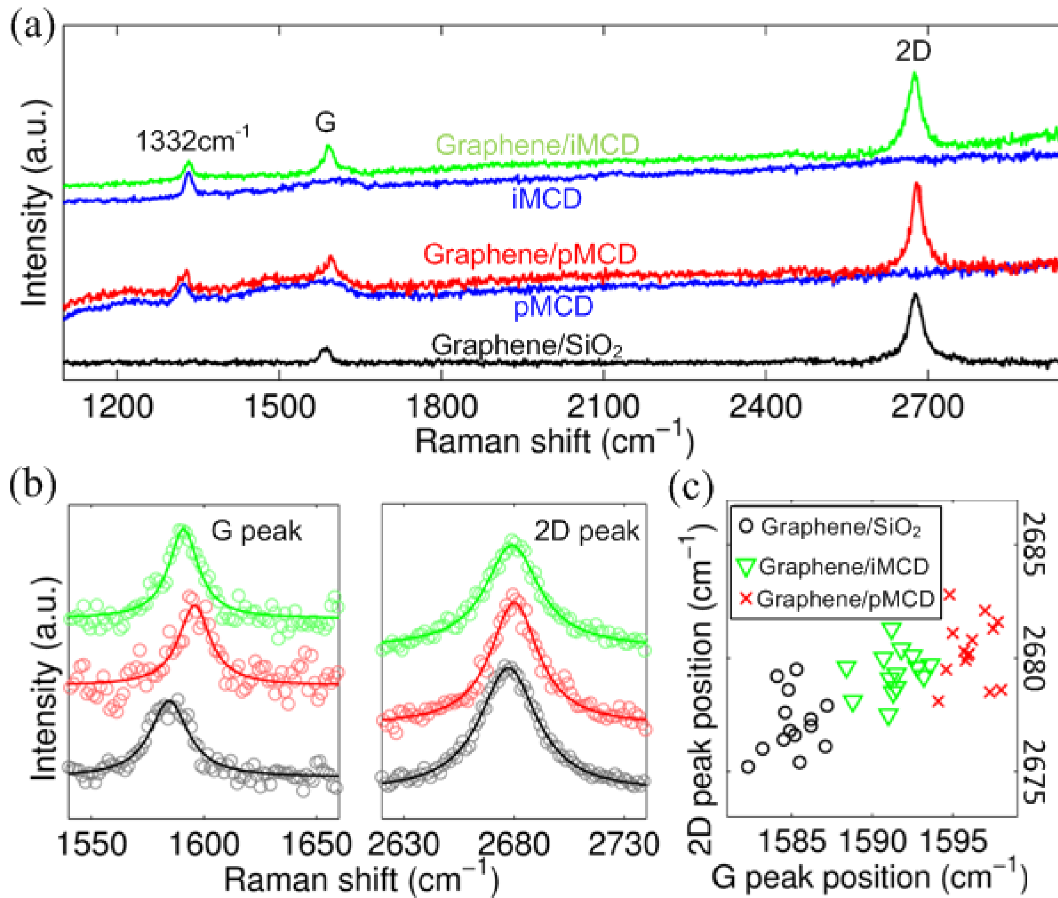

Figure 5.4. (a) Raman spectra of the same batch of CVD-grown graphene transferred onto SiO_2/Si substrate, intrinsic MCD (iMCD) and p-type doped MCD (pMCD). Raman spectra of bare iMCD and pMCD are also shown for comparison. (b) Comparing positions of G and 2D peaks of

graphene/SiO_2 (black), graphene/iMCD (green), and graphene/pMCD (red). Circles are experimental data and lines are Lorentzian fits. (c) G and 2D peak positions obtained from multiple measurements on multiple samples.

Raman spectra of the graphene/MCD heterojunctions provide important information on the charge transfer between graphene and MCD. Graphene's carrier concentration strongly affects its phonon frequency due to the breakdown of Born-Oppenheimer approximation in graphene [156]. As a result, positions of both G and 2D peaks will change upon doping. Specifically, a major blue shift of G peak and a minor red shift of 2D peak are observed with an increasing electron concentration. On the other hand, with an increasing hole concentration, a major blue shift of G peak and a minor blue shift of 2D peak will be observed [156] [157]. Figure 5.4b shows the zoom-in view of the G peaks and 2D peaks, respectively, of graphene/SiO_2 (black), graphene/pMCD (red), and graphene/iMCD (green) samples. Circles are experimental data and lines are Lorentzian fits. The Lorentzian fitting from Figure 5.4b shows that the G/2D peak frequency of our graphene transferred onto SiO_2, iMCD, and pMCD is at 1584.5/2676.4, 1591.1/2679.1, and 1595.9/2680.1 cm^{-1}, respectively. Raman spectra have been taken at several similarly-prepared samples, and at many different randomly-selected locations on each sample. The spectra shown in Figures 4a and 4b are typical spectra of all measurements. In addition, Figure 5.4c shows the distribution of G peak and 2D peak positions over multiple measurements on multiple samples. It's clearly observed that, in the order of graphene/SiO_2, graphene/iMCD, and graphene/pMCD, the G/2D peak experiences a large to small blue shift, despite a sample-to-sample uncertainty of about $3cm^{-1}$. The graphene/SiO_2 sample has been measured to be p-type doped with a doping concentration of $2\times10^{12}cm^{-2}$. Our results in Figure 5.4c show that the graphene on MCD substrate is p-type doped. Comparing our G peak positions with the results given by Das et al. [157], graphene on iMCD is estimated to have a doping concentration of $6\times10^{12}cm^{-2}$, and graphene on pMCD is estimated to have a doping concentration of $1.1\times10^{13}cm^{-2}$. Since samples of graphene on pMCD show a significantly higher doping concentration than that of graphene on iMCD, the origin of such doping must be direct charge (hole) transfer from MCD to graphene, unlike the case of graphene on SiO_2/Si where substrate impurity charge puddles play a major role in the doping of graphene [158]. The direct hole transfer from MCD to graphene will leave a depletion region in MCD such that a heterojunction is built with an electrical potential barrier blocking the transport of holes from graphene to MCD.

Current-voltage (J-V) characteristics of the fabricated heterojunctions are measured in dark and under illuminations of different wavelengths. All measurements are carried out at room temperature and in the atmospheric environment. The black curves in Figures 5a and 5b are J-V characteristics of graphene/iMCD and graphene/pMCD, respectively, measured in dark. Both of them show a strong rectification behavior: the forward bias (negative voltage) current increases exponentially with the forward bias voltage while the reverse bias current remains at a low level under the reverse bias voltage. According to our experiments, breakdown happens when the reverse bias voltage becomes larger than 5V. Junctions between graphene and conventional finite-gap semiconductors typically behave similar to metal-semiconductor Schottky junctions and can usually be described by the law of thermionic emission [159] [160]:

$$J = A^*T^2 \exp(-\frac{q\phi_b}{kT})\,(\exp(-\frac{qV}{kT}) - 1) \tag{5.1}$$

where J is current density, A^* is the Richardson constant [161], k is the Boltzmann constant, T is temperature, φ_b is heterojunction barrier height, and V is the bias voltage. A more accurate model for current-voltage characteristics of graphene-based Schottky-like junctions has been proposed by considering the dependence of φ_b on V [160]. Unlike metals, graphene has a limited density of states (DOS) around its Fermi level and therefore its Fermi-level position, as well as φ_b, will be shifted by the applied bias voltage V. Assuming under a constant φ_b, a fairly constant reverse current is expected according to Eq. (5.1). However, the measured data show a clear trend of increasing J with the increasing magnitude of V, which implies that φ_b must decrease with the increasing magnitude of V.

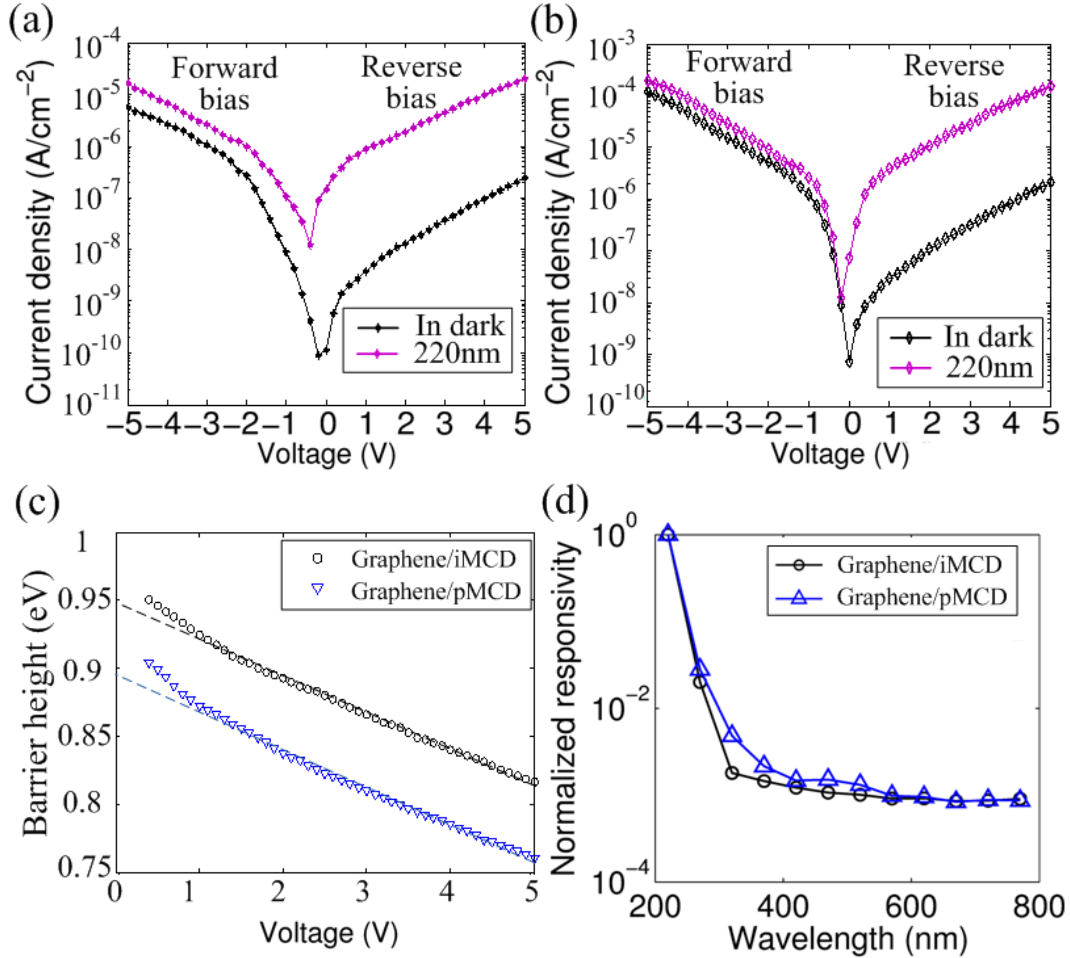

Figure 5.5. Current-voltage (J-V) characteristics of (a) graphene/iMCD and (b) graphene/pMCD heterojunctions in dark (black) and under an illumination of 220nm (purple) light source with a power density of 100μW/cm^2. (c) Extrapolation of zero-bias barrier height from measured J-V data. (d) Dependence of normalized optical responsivity on illumination wavelength.

To estimate the heterojuction barrier height, the thermionic emission equation (Eq. (5.1)) can be approximated by the equation below, when the bias voltage V is much larger than $3kT$ (when V>> 0.1V at room temperature).

$$J = A^* T^2 \exp(-\frac{q\phi_b(V)}{kT}) \qquad (5.2)$$

The value of φ_b can be plotted as a function of V using the measured J-V data and Eq. 5.2, as shown in Figure 5.5c. The zero-bias barrier height is extrapolated to be 0.947eV and 0.89eV for the graphene/iMCD and graphene/pMCD heterojunctions, respectively. Deviations at the low voltage end might be caused by finite ideality factors[1] which are neglected here.

The purple curves in Figures 5a and 5b are J-V characteristics recorded under illumination at 220nm with a power density of 100μW/cm^2. Monochromatic illumination is generated by filtering a 350W broadband Xenon lamp with a monochromator (FWHM~15nm). Incident optical power has been carefully calibrated with a commercial silicon photodiode. Interestingly, it's observed that the J-V rectification effect observed in dark is annihilated by the UV illumination, and the J-V characteristics become ohmic-like with high current under both forward and reverse bias voltages. This could be explained by a significant reduction of heterojunction barrier by the UV illumination. A large difference between the illuminated current and dark current can be obtained in the reverse bias region. The responsivity under the 5V reverse bias for the graphene/iMCD and graphene/pMCD device reaches 0.2A/W and 1.4A/W, respectively. For ideal photodiodes with a quantum efficiency of η, the responsivity R for illumination at frequency ν can be evaluated by [162]:

$$R = \frac{\eta e}{h\nu} \qquad (5.3)$$

The measured R values of our devices are larger than the maximum (η=100%) responsivity (R_{max}=0.18A/W at 220nm), indicating the existence of a photocurrent gain which is absent in ideal Schottky photodiodes [162]. Similar non-ideal gain behaviors have also been observed on metal/diamond and metal/GaN Schottky-junction photodiodes [163] [164]. For those devices the defects at metal/semiconductor interface can capture and trap photo-generated carriers, and induce a reduction of Schottky barrier height upon illumination, leading to a photocurrent gain. Non-ideal behaviors of our graphene/MCD photodiodes here might be also due to interface defects. However, further experimental characterizations and theoretical analyses are required to clarify this. Figure 5.5c plots the normalized responsivity measured at different illumination wavelengths ranging from 220nm to 770nm, showing the solar-blind feature of graphene/MCD as a photodetector. Responsivity at 220nm is found to be almost three orders of magnitude higher than those within the visible (400-700nm) and near UV (300nm-400nm) ranges.

In summary, a novel layer transfer process is developed to transfer monolayer graphene onto microcrystalline diamond (MCD) films which combining the benefits of low cost and excellent optoelectronic properties. The surface roughness problem of the MCD film is successfully surpassed by using its smooth backside for the graphene transfer process. Charge transfer between graphene and MCD is probed by Raman spectroscopy, showing that holes from MCD move towards the graphene layer on top and a graphene/MCD heterojunction is formed. Such a flexible device is demonstrated as solar-blind photodiode with graphene as a transparent electrode. Current-voltage characteristics are measured both in dark and under illuminations of different wavelengths, showing high responsivity under UV illumination as well as high UV/solar rejection ratio.

The followings are additional material and device characterizations involved in this work but not included in the main text above.

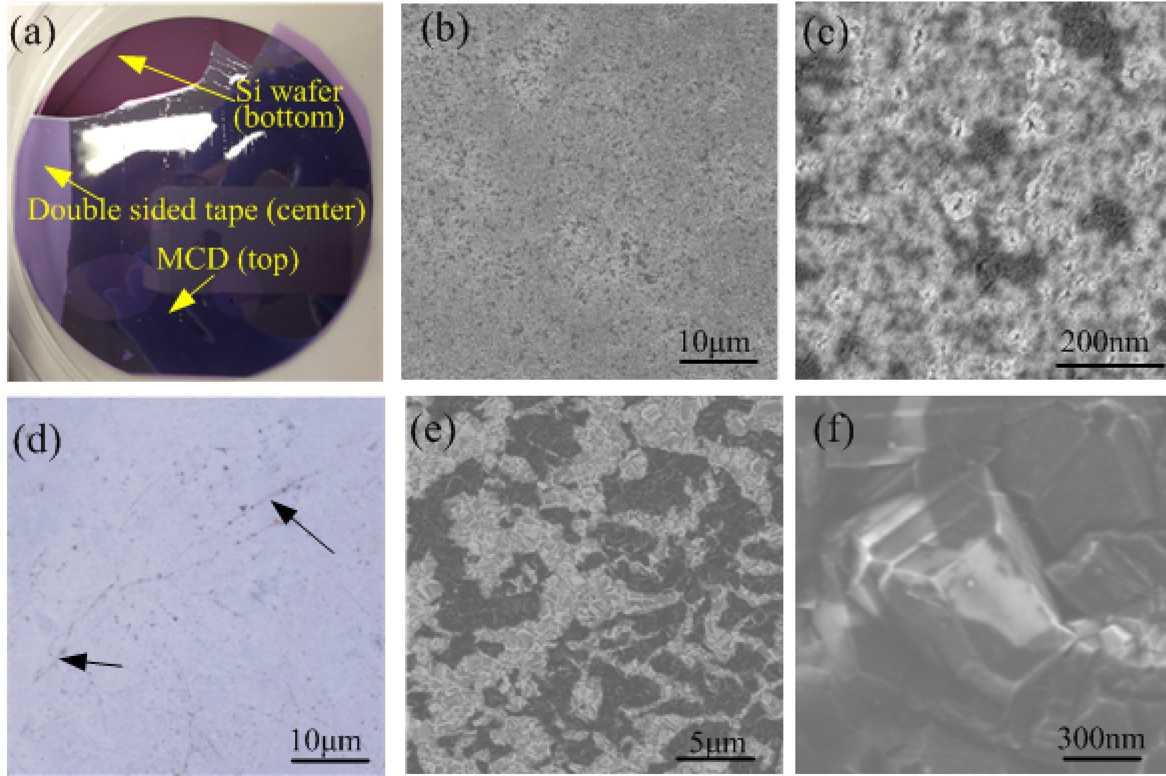

Figure 5.6. (a) Photograph of the whole 4-inch in diameter MCD film (partially broken on the left and top edges) being transferred to a silicon substrate. The double-sided tape is used to attach and peel off the MCD film from the growth substrate and to transfer the film onto a new substrate with the flat MCD surface (the backside of the film on the original growth substrate) on top now. (b, c) SEM images of the exposed backside of the peeled-off MCD film. (d) Optical microscope photos after the graphene sheet is placed onto the back side of the MCD film. Arrows indicate graphene wrinkles. (e, f) SEM images showing results of the graphene sheet being placed on the rough front side of the MCD film. Graphene (darker in contrast) is punctured apart by the sharp crystal edges and corners of the diamond crystals into smaller pieces as shown.

MCD field effect transistors (FETs) are fabricated for material property evaluations using a 300nm-thick SiO_2 layer as the gate dielectric material; ebeam-evaporated Au (50nm) as the gate metal and annealed Ti/Au (150nm/300nm) as the source/drain contact pads. A shadow mask is used to define the channel length of 2mm and width of 4mm. Doping concentration (N_A) and the field effect hole mobility μ are estimated from the linear region of the I_D-V_G curve (Figure 5.7a) at room temperature by the least-square fitting. In the linear region under small V_D, experimental data can be fitted with the equation [162]:

$$I_D = \frac{W \mu C}{L}(V_G - V_T)V_D \qquad (5.4)$$

For MCD FETs, C is gate capacitance (300nm SiO_2) per unit area and V_T is the threshold voltage. Linear hole mobility μ is fitted (Figure 5.7a) to be 35cm^2/(V-s) and 38cm^2/(V-s) for the pMCD and iMCD, respectively. Doping concentration (~carrier concentration) is estimated by combining the resistivity at the zero gate voltage and the linear region mobility calculated above.

It is noted that when V_G is zero, both FETs based on the pMCD and iMCD films are in the linear region. Doping concentration is calculated as:

$$N_A \approx p = \frac{I_D L}{eV_D W t \mu} \tag{5.5}$$

where t is channel thickness (~2μm) and N_A is calculated as $4\times10^{17}cm^{-3}$ and $5\times10^{15}cm^{-3}$ for the pMCD and iMCD films, respectively.

Electrical properties of CVD-grown graphene is also characterized (Figure 5.7b) by measuring a graphene FET (inset in Figure 5.7b) with heavily p-doped silicon substrate as the back gate, and ebeam-evaporated Cr/Au (20nm/100nm) as the source/drain contact pads. The channel length and width are both 10μm. The I_D-V_G curve is fitted (Figure 5.7b) with the following device equations taking quantum capacitance into consideration [165]:

$$R_{sd} = \frac{I_D}{V_D} = \frac{L/W}{q\mu\sqrt{p_o^{\,2} + p^2}} \tag{5.6}$$

$$V_{gD} - V_g = \frac{q}{C_{ox}} p + \frac{\hbar v_F \sqrt{\pi p}}{q} \tag{5.7}$$

Since only the low-field hole mobility is used in this work, only the p-type branch is fitted. Here R_{sd} is channel resistance; p_0 is the initial impurity doping concentration of the CVD-graphene; p is the induced doping due to gate voltage; and C_{ox} is gate capacitance (300nm SiO_2) per unit area. The fitted mobility is $3500cm^2/(V\text{-}s)$ and $p_0=2\times10^{12}cm^{-2}$.

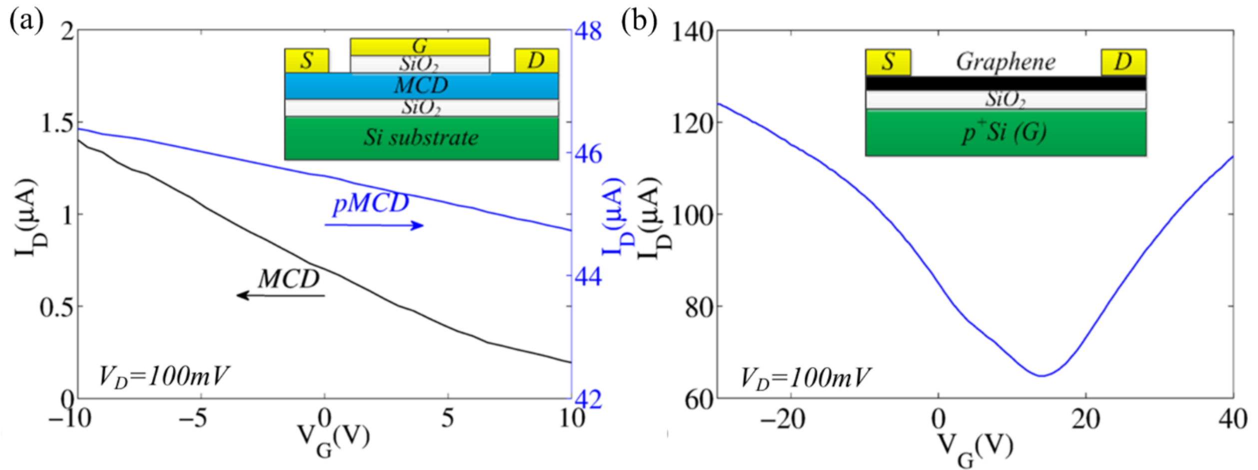

Figure 5.7. Field effect transistor characterizations of: (a) MCD thin film; and (b) CVD-grown graphene for the estimations of doping concentration and mobility.

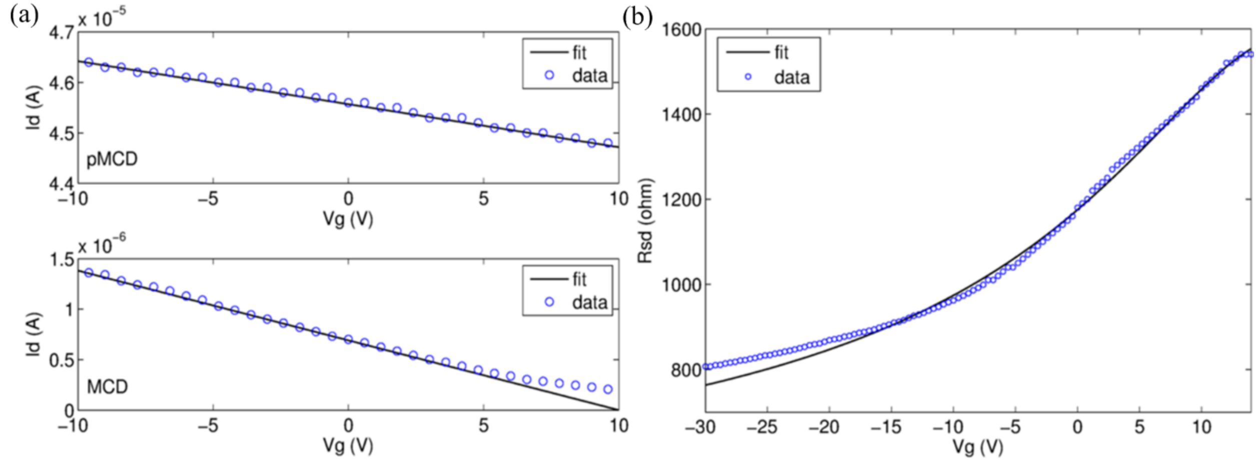

Figure 5.8. (a) Fitting results of the I_d-V_g transfer characteristics on the pMCD and iMCD FETs, with V_D of 100mV. (b) Fitting results of the p-type branch of the R_{sd}-V_g transfer characteristics of the graphene FET, with V_D of 100mV.

5.3 Piezoelectricity-induced Schottky barrier height variations in AlGaN/GaN high electron mobility transistors

High electron mobility transistors (HEMTs) based on the AlGaN/GaN heterostructure featuring two-dimensional electron gas (2DEG) have been actively studied for high frequency and high power electronics, as well as chemical and mechanical sensors [166]. Applications such as micro strain and pressure sensors have attracted great interests [167] [168] [169] [170] due to the good piezoelectric properties of AlGaN and GaN along the [0001] direction. Externally applied strain can change the net polarization charge density at the AlGaN/GaN interface due to the differences in their piezoelectric coefficients which results in variations in 2DEG concentrations [167]. This phenomenon is defined as the direct piezoelectric effect in this paper. For Ga-faced HEMT devices (this work), an external tensile strain will result in an increased 2DEG concentration. However, an opposite trend to the direct piezoelectric effect has been recorded in this work. In order to explain the observed behavior, Schottky gate barrier height changes due to the applied strains for 2DEG devices are investigated. Our findings show good consistency between analytical and experimental results. As such, piezoelectricity induced Schottky barrier height change could be an important element to be considered for the design of AlGaN/GaN HEMT-based electronic and sensing devices.

The fabrication process starts with custom-made wafers with $Al_{0.2}Ga_{0.8}N$/GaN (30nm/2µm) grown on Si (111) by using the metalorganic chemical vapor deposition (MOCVD) process [171]. Very low wafer bow (-0.5µm and -5.1µm) were measured by laser profilometry indicating small residual stress. Mesas of 40 um in diameter are first etched by the Cl_2/BCl_3/Ar plasma with a depth of 180nm for electrical isolation. A layer of Ti/Al/Pt/Au (20/80/50/100nm) is evaporated for source/drain ohmic contact with a rapid thermal annealing process at 850ºC for 35 seconds. The contact resistance is measured using the transmission line geometry method as $1.6x10^{-5}\Omega.cm^{-2}$. The Schottky gate contact is constructed by using evaporated Ni/Au (20/200nm). Before the gate metal evaporation process, the exposed AlGaN surface has been first cleaned by oxygen plasma (1min with RF power of 50W and pressure of 180mTorr), and rinsed in diluted NH_4OH solution (1:10) for 10 seconds to remove surface oxide. A 200nm thick PECVD SiN_x

layer is deposited at 350ºC for the passivation. Without the passivation layer, the drain current fluctuates and decreases greatly with time and can't be recorded for meaningful results. Finally, contact pads are opened on the SiN_x layer.

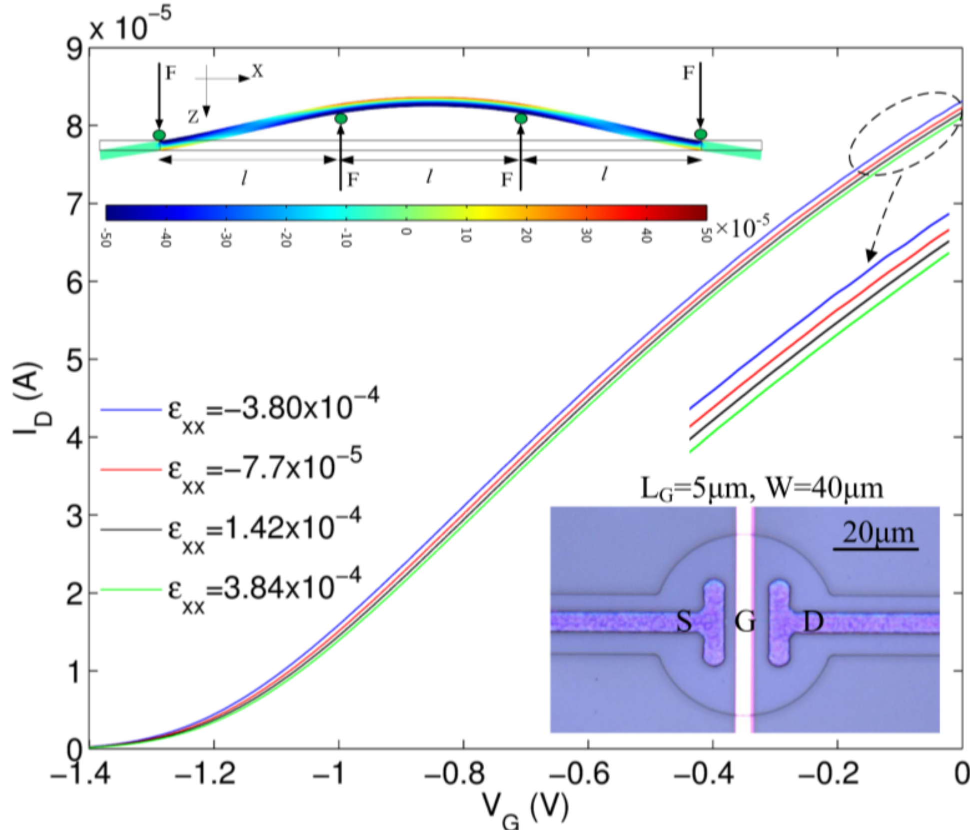

Figure 5.9. The I_D versus V_G transfer characteristics of an AlGaN/GaN HEMT device measured with different magnitudes of externally applied strain ε_{xx}. Inset shows the schematics of four-point wafer bending setup with simulated ε_{xx} profile under a loading force *F* of 15N, and an optical photo of a fabricated device with detailed dimensions.

Two wafers have been fabricated and cut into 5cm×2.5cm chips for the strain tests using a standard four-point bending method as shown in Figure 5.9. A total of 11 devices have been measured and reported. The uniaxial stress is applied along the x-direction and the magnitude of the applied force is monitored by a high-precision load cell. The induced strains (ε_{xx}, ε_{yy}, and ε_{zz}) are calculated analytically [172] and simulated numerically using the commercial finite element software (COMSOL).

Figure 5.9 presents the I_D-V_G transfer characteristics measured with different magnitudes of strain ε_{xx}, under V_{DS} of 0.1V. Inset of Figure 5.9 shows microscope photo of a fabricated HEMT device and the schematics of the four-point bending test setup. It is observed that the drain current decreases/increases with respect to tensile/compressive strain under a fixed V_G, respectively. Furthermore, time-resolved variations of I_D under fixed V_G have been measured with stepwise changes of ε_{xx} (not shown here) to confirm that the measured trend of I_D with respect to ε_{xx} is highly repeatable and hysteresis-free.

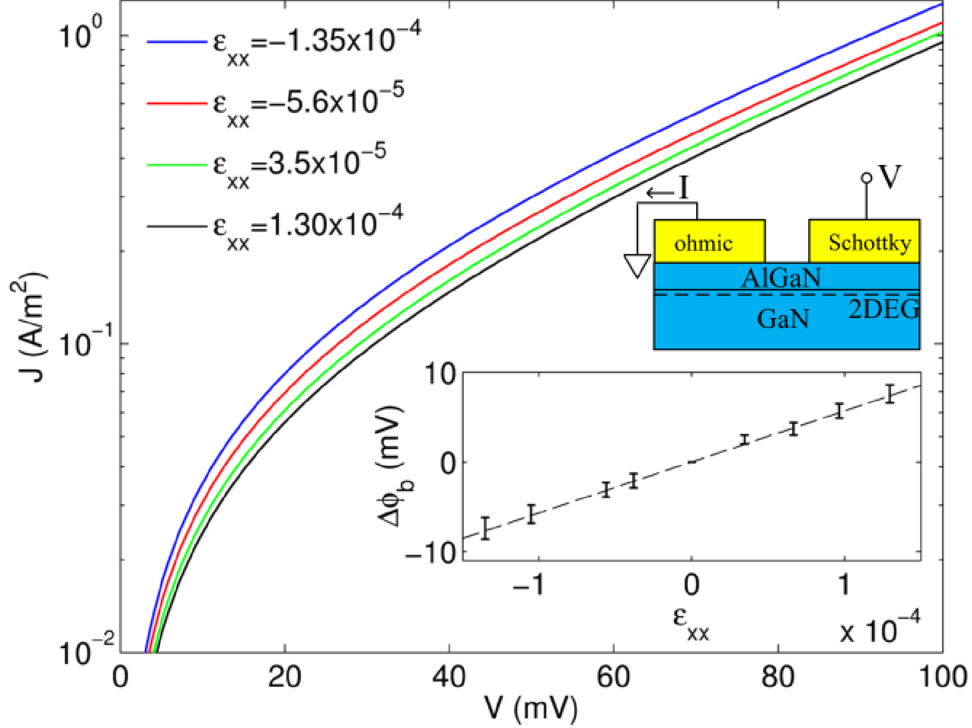

Figure 5.10. The gate-to-source *J-V* measurements under forward bias with different magnitudes of externally applied strain, ε_{xx}. Inset: extracted values of Schottky barrier height versus ε_{xx}, and a cross-sectional view of the measurement setup.

To explain the opposite trend (external tensile strain results in decreased 2DEG concentration), the *J-V* characteristics between gate and source are characterized under different magnitudes of strain as shown in Figure 5.10. It is observed that under a fixed voltage, the resulting current density decreases under the tensile strain and increases under compressive strain. Previously, researchers have found that under a small forward bias, gate-to-source *J-V* characteristics follow the law of thermionic emission [173] with Schottky barrier height, φ_b. Therefore variations of current in Figure 5.10 indicate changes of φ_b, as shown by the inset. The slope between the barrier variation $\Delta\varphi_b$ and ε_{xx} is ~55µV per microstrain in this work.

The gate Schottky barrier height φ_b has a strong effect on the transfer characteristics of AlGaN/GaN HEMT. Threshold voltage V_{th} and 2DEG electron concentration n_s are extracted from measured I_D-V_G curves under different strain using the published AlGaN/GaN HEMT device model [174] [175]. The Hall measurement hasn't been employed here as the four point wafer bending setup is made of stainless steel. Variations of V_{th} and n_s (denoted ΔV_{th} and Δn_s) in presence of ε_{xx} are plotted in Figure 5.11. The analytical expression of V_{th} is given by [174]:

$$V_{th} = \phi_b - \frac{\Delta E_C}{q} - \frac{\sigma_{tot} d_{AlGaN}}{\varepsilon_{AlGaN}} \quad (5.8)$$

where q is electron charge, σ_{tot} is the total polarization charge density at the AlGaN/GaN interface; d_{AlGaN} and ε_{AlGaN} are the thickness and permittivity of the AlGaN barrier layer, respectively; and ΔE_C is the AlGaN/GaN heterojunction band offset. In Figure 5.11a, the Schottky barrier effect calculation is simply the slope of measured $\Delta\varphi_b$-ε_{xx}, while the direct piezoelectric effect is calculated by:

$$\Delta\sigma_{tot} = (p_{31}^{AlGaN} - p_{31}^{GaN})(\varepsilon_{xx} + \varepsilon_{yy}) + (p_{33}^{AlGaN} - p_{33}^{GaN})\varepsilon_{zz} \tag{5.9}$$

where $\Delta\sigma_{tot}$ is the strain-induced change of σ_{tot}; p_{31}^{AlGaN}, p_{31}^{GaN}, p_{33}^{AlGaN} and p_{33}^{GaN} are material piezoelectric coefficients. In Figure 5.11b, the values of Δn_s are calculated based on [176]:

$$\Delta n_s = \frac{\Delta\sigma_{tot}}{q} - \left(\frac{\varepsilon_{AlGaN}}{d_{AlGaN} q^2}\right) e\Delta\phi_b \tag{5.10}$$

The yellow and blue shaded areas indicate the calculation uncertainties based on previously reported piezoelectric and elastic stiffness coefficients [177] [178] [179] [180]. For both ΔV_{th} and Δn_s, the Schottky barrier effect and direct piezoelectric effect give opposite contributions as shown. The experimentally measured results in this work matches well with the combined effect.

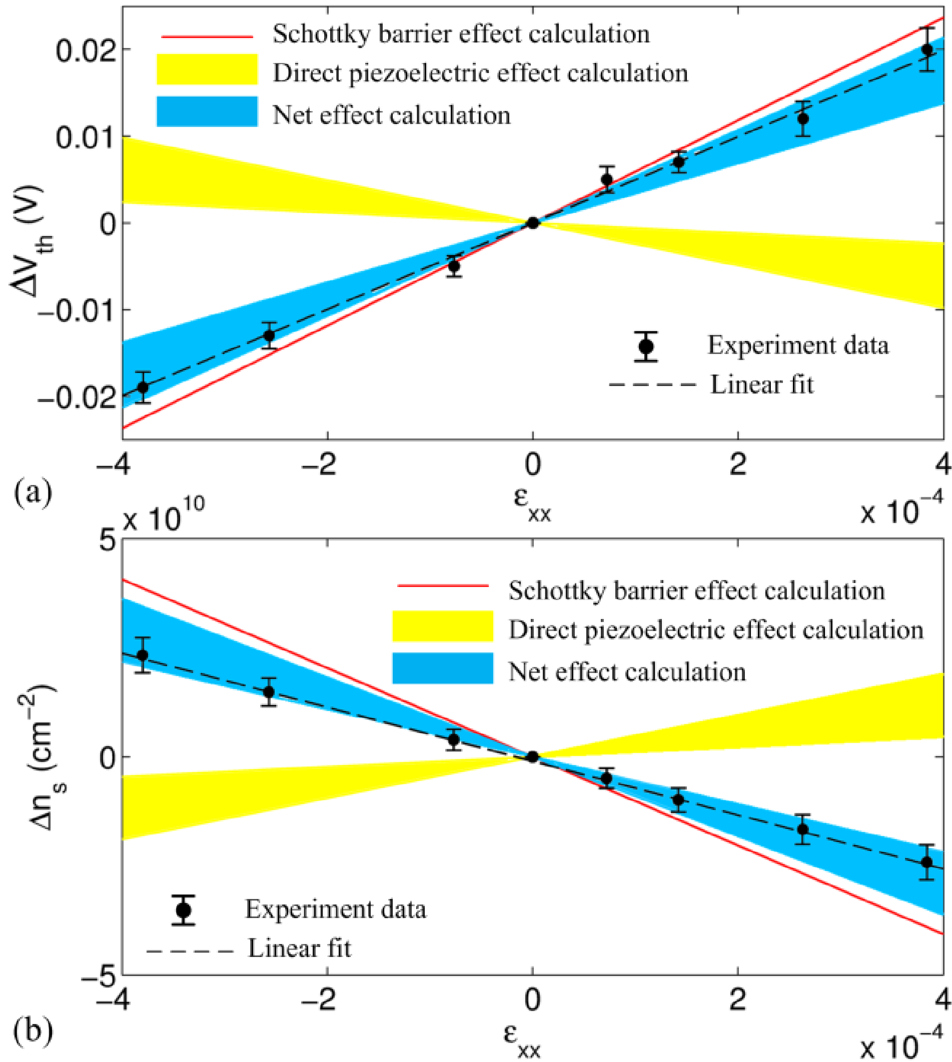

Figure 5.11. Comparison of the Schottky barrier effect, direct piezoelectric effect, and their combined effect with measured results for (a) ΔV_{th} and (b) Δn_s with respect to ε_{xx}. The yellow and blue shaded areas are calculation uncertainties based on previously reported piezoelectric and stiffness coefficients [177] [178] [179] [180].

The above analyses and results support the proposed effect of piezoelectricity induced Schottky barrier height changes. The external tensile stress results in tensile strain ε_{xx} and compressive strains ε_{yy} and ε_{zz} while p_{33} (p_{zz}) is positive and p_{31} (p_{zx}) is negative. The overall net piezoelectric effect is an increase of the negative polarization charges at the top surface of AlGaN barrier. In response, more interface donor states may be ionized to hold positive charges, and the conduction band edge energy of AlGaN at the Ni/AlGaN interface moves upward leading to an increase in gate barrier height. Another factor is the charge changes at the gate due to the applied strain. The gate capacitance, C_G, is the parallel plate capacitance between gate metal and 2DEG before depletion. For example, under a strain ε_{xx} of $1.5\text{x}10^{-4}$, ΔQ_G is calculated as $1.5\times10^{-7}V_G$ C/m^2 (using dielectric constant and poison ratio of AlGaN from [176]). The charge changes due to the piezoelectric effect is calculated (right side of Eq. 5.11) as $7.2\text{x}10^{-5}$ C/m^2, which is 2~3 orders of magnitude higher than that of ΔQ_G (for typical V_G in our experiments). Therefore, the gate charge changes due to strain are neglected and net charge changes are expressed as:

$$q^2\Delta\phi_b D_{it} \approx p_{31}^{AlGaN}(\varepsilon_{xx}+\varepsilon_{zz})+p_{33}^{AlGaN}\varepsilon_{yy} \qquad (5.11)$$

where D_{it} is the interface state density. Under the same applied strain, the right hand side of Eq. 5.11 is the same and smaller D_{it} results in a larger Schottky barrier variation. Here, capacitance and conductance of a circular-shape (70µm radius) Ni/Au Schottky contact have been measured with respect to frequency in Figure 5.12a and D_{it} is extracted as $4.5\pm0.4\times10^{12}$cm^{-2}eV^{-1} [50] -a low number as compared with prior reports [181] [182] [183]. Figure 5.12b shows the values of $\Delta\varphi_b$ extracted from experimental data and compared with the model (Eq. 5.11) with very good agreements over the applied strain. If D_{it} is 1.8×10^{13}cm^{-2}eV^{-1} or larger, the strain-induced Schottky barrier variation becomes negligible as shown by the red shaded area in Figure 5.12b.

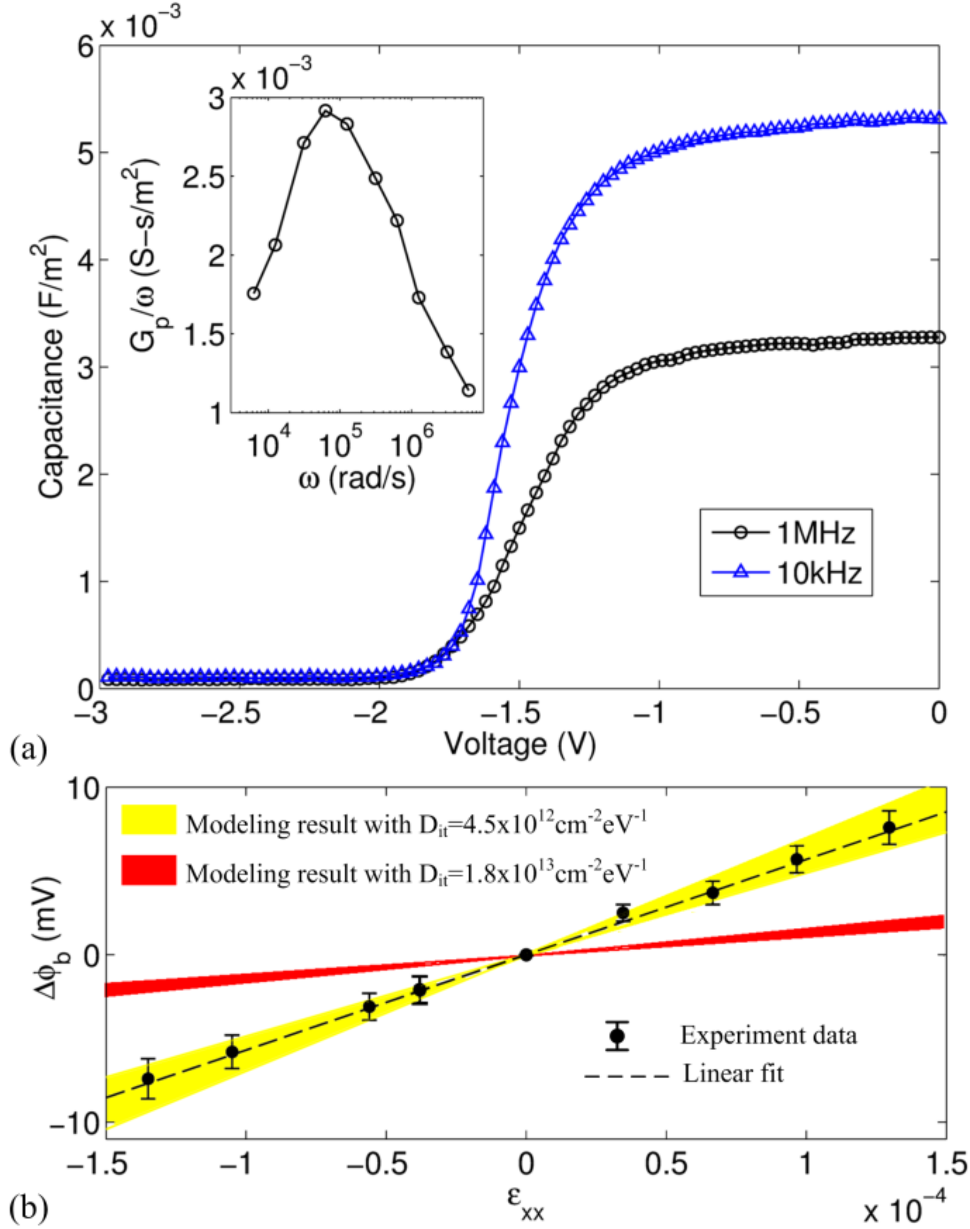

Figure 5.12. (a) Capacitance-voltage characteristics of Ni/Au contacts on the AlGaN/GaN devices. Inset - dependence of conductance on angular frequency. (b) Comparing experimental and modeled $\Delta\varphi_b$-ε_{xx} relation. The red and yellow shaded areas are uncertainties based on reported material coefficients [44-48].

The nickel-based Schottky gate structure for the AlGaN/GaN HEMT devices has been studied and piezoelectricity induced Schottky barrier height variations have been characterized. The observed barrier height variations with respect to the applied strain are attributed to the Ni/AlGaN interface state charges. This effect is shown to have a strong influence on the HEMT threshold voltage and 2DEG electron concentrations.

Bibliography

[1] Novoselov, K.S., Geim, A.K., Morozov, S.V., Jiang, D., Zhang, Y., Dubonos, S.V., Grigorieva, I.V. and Firsov, A.A., "Electric field effect in atomically thin carbon films.," *Science ,* vol. 306, no. 5696, pp. 666-669, 2004.

[2] Mak K.F., Lee C., Hone J., Shan J., and Heinz T.F., "Atomically Thin MoS2: A New Direct-Gap Semiconductor," *Phys. Rev. Lett.,* vol. 105, p. 136805, 2010.

[3] Splendiani, A., Sun, L., Zhang, Y., Li, T., Kim, J., Chim, C.Y., Galli, G. and Wang, F., , "Emerging photoluminescence in monolayer MoS2.," *Nano letters,* vol. 10(4), pp. pp.1271-1275., 2010.

[4] Zhao W., Ghorannevis Z., Chu L., Toh M., Kloc C., Tan P.H., and Eda G., "Evolution of Electronic Structure in Atomically Thin Sheets of WS2 and WSe2," *ACS Nano,* vol. 7, p. 791, 2012.

[5] Ross, J.S., Wu, S., Yu, H., Ghimire, N.J., Jones, A.M., Aivazian, G., Yan, J., Mandrus, D.G., Xiao, D., Yao, W. and Xu, X.,, "Electrical control of neutral and charged excitons in a monolayer semiconductor.," *Nature communications,* vol. 4, p. p.1474., 2013 .

[6] Wu, S., Buckley, S., Schaibley, J.R., Feng, L., Yan, J., Mandrus, D.G., Hatami, F., Yao, W., Vuckovic, J., Majumdar, A. and Xu, X., "Monolayer semiconductor nanocavity lasers with ultralow thresholds," *Nature,* vol. 520(7545), p. 69, 2015.

[7] Ye, Y., Wong, Z.J., Lu, X., Ni, X., Zhu, H., Chen, X., Wang, Y. and Zhang, X., "Monolayer excitonic laser," *Nature Photonics,* vol. 9(11), p. 733, 2015.

[8] Xiao, D., Liu, G.B., Feng, W., Xu, X. and Yao, W., "Coupled spin and valley physics in monolayers of MoS 2 and other group-VI dichalcogenides.," *Phys. Rev. Lett.,* vol. 108, no. 19, p. 196802, 2012.

[9] Cao, T., Wang, G., Han, W., Ye, H., Zhu, C., Shi, J., Niu, Q., Tan, P., Wang, E., Liu, B. and Feng, J, "Valley-selective circular dichroism of monolayer molybdenum disulphide.," *Nature communications,* vol. 3, p. 887, 2012.

[10] Ribeiro-Palau, R., Zhang, C., Watanabe, K., Taniguchi, T., Hone, J. and Dean, C.R., "Twistable electronics with dynamically rotatable heterostructures.," *Science,* vol. 6403, no. 301, pp. 690-693., 2018.

[11] Koperski, M., Nogajewski, K., Arora, A., Cherkez, V., Mallet, P., Veuillen, J.Y., Marcus, J., Kossacki, P. and Potemski, M., "Single photon emitters in exfoliated WSe2 structures.," *Nature nanotechnology,* vol. 6, no. 10, p. 503, 2015.

[12] Seyler, K.L., Rivera, P., Yu, H., Wilson, N.P., Ray, E.L., Mandrus, D.G., Yan, J., Yao, W. and Xu, X., "Signatures of moiré-trapped valley excitons in MoSe2/WSe 2 heterobilayers.," *Nature,* vol. 7746, no. 567, p. 66, 2019.

[13] Qiu, D.Y., Felipe, H. and Louie, S.G. , "Optical spectrum of MoS 2: many-body effects and diversity of exciton states," *Physical review letters,* vol. 111(21), p. 216805, 2013.

[14] M.L. Cohen, S.G. Louie, Fundamentals of Condensed Matter Physics, Cambridge University Press, 2016.

[15] Wang, G., Marie, X., Gerber, I., Amand, T., Lagarde, D., Bouet, L., Vidal, M., Balocchi, A. and Urbaszek, B., "Giant enhancement of the optical second-harmonic emission of WSe 2 monolayers by laser excitation at exciton resonances," *Phys. Rev. Lett.,* vol. 114, no. 9, p. 097403, 2015.

[16] Scuri, G., Zhou, Y., High, A.A., Wild, D.S., Shu, C., De Greve, K., Jauregui, L.A., Taniguchi, T., Watanabe, K., Kim, P., Lukin, M.D., and Park, H., "Large excitonic reflectivity of monolayer MoSe2 encapsulated in hexagonal boron nitride," *Physical review letters,* vol. 120, no. 3, p. 037402, 2018.

[17] Bernardi, M., Palummo, M. and Grossman, J.C., "Extraordinary sunlight absorption and one nanometer thick photovoltaics using two-dimensional monolayer materials," *Nano letters,* vol. 13(8), pp. 3664-3670, 2013.

[18] Seyler, K.L., Schaibley, J.R., Gong, P., Rivera, P., Jones, A.M., Wu, S., Yan, J., Mandrus, D.G., Yao, W. and Xu, X., "Electrical control of second-harmonic generation in a WSe2 monolayer transistor.," *Nature nanotechnology,* vol. 10, no. 5, p. 407, 2015.

[19] Yao, K., Yan, A., Kahn, S., Suslu, A., Liang, Y., Barnard, E., Tongay, S., Zettl., A., Borys, N.J., and Schuck, P.J.;, "Optically discriminating carrier-induced quasiparticle band gap and exciton energy renormalization in monolayer MoS2," *Phys. Rev. Lett.,* p. Accepted, 2017.

[20] J. Jackson, Classical electrodynamics, 1999.

[21] Mak, K.F., He, K., Lee, C., Lee, G.H., Hone, J., Heinz, T.F. and Shan, J., "Tightly bound trions in monolayer MoS2," *Nature materials,* vol. 12(3), pp. 207-211, 2013.

[22] Chernikov, A., van der Zande, A.M., Hill, H.M., Rigosi, A.F., Velauthapillai, A., Hone, J. and Heinz, T.F., "Electrical tuning of exciton binding energies in monolayer WS2.," *Physical review letters,* vol. 12, no. 115, p. 126802, 2015.

[23] Yao K., T. E. Smidt, M. Collins, K. M. Nell, E. S. Barnard, N. J. Borys, T. Kuykendall, J.B. Neaton, J.N. Hohman, and P.J.Schuck, "Strongly Quantum Confined Excitons in Two Dimensional Layered Hybrid Metal Chalcogenolate Multi Quantum Wells," *In preparation.*

[24] Ye, Z., Cao, T., O'Brien, K., Zhu, H., Yin, X., Wang, Y., Louie, S.G. and Zhang, X., "Probing excitonic dark states in single-layer tungsten disulphide," *Nature,* vol. 513(7517), pp. 214-218., 2014.

[25] Wang, G., Robert, C., Glazov, M.M., Cadiz, F., Courtade, E., Amand, T., Lagarde, D., Taniguchi, T., Watanabe, K., Urbaszek, B. and Marie, X., "In-plane propagation of light in transition metal dichalcogenide monolayers: optical selection rules.," *Phys. Rev. Lett.,* vol. 119, no. 4, p. 047401, 2017.

[26] D. Kozawa, R. Kumar, A. Carvalho, K.K. Amara, W. Zhao, S. Wang, M. Toh, R.M. Ribeiro, A.C. Neto, K. Matsuda, and G. Eda, "Photocarrier relaxation pathway in two-dimensional semiconducting transition metal dichalcogenides," *Nat. Commun.,* vol. 5, p. 4543, 2014.

[27] Dresselhaus, M., Dresselhaus, G., Cronin, S.B., Gomes Souza Filho, A., Solid State Properties, Springer, 2018.

[28] Liang, Y. and Yang, L., "Carrier plasmon induced nonlinear band gap renormalization in two-dimensional semiconductors," *Physical review letters,* vol. 114(6), p. p.063001, 2015.

[29] Chernikov, A., Ruppert, C., Hill, H.M., Rigosi, A.F. and Heinz, T.F., "Population inversion and giant bandgap renormalization in atomically thin WS2 layers," *Nature Photonics,* vol. 9(7) , pp. pp.466-470., 2015.

[30] Chernikov, A., Berkelbach, T.C., Hill, H.M., Rigosi, A., Li, Y., Aslan, O.B., Reichman, D.R., Hybertsen, M.S. and Heinz, T.F., "Exciton binding energy and nonhydrogenic Rydberg series in monolayer WS2.," *Physical review letters,* vol. 113(7), p. 076802, 2014.

[31] Koch, S.W., Kira, M., Khitrova, G. and Gibbs, H.M., "Semiconductor excitons in new light.," *Nature materials,* vol. 5, no. 7, p. 523, 2006.

[32] Wang, K., Wang, J., Fan, J., Lotya, M., O'Neill, A., Fox, D., Feng, Y., Zhang, X., Jiang, B., Zhao, Q. and Zhang, H., "Ultrafast saturable absorption of two-dimensional MoS2 nanosheets.," *ACS nano,* vol. 7, no. 10, p. 9260, 2013.

[33] Liu, H., Li, Y., You, Y.S., Ghimire, S., Heinz, T.F. and Reis, D.A., "High-harmonic generation from an atomically thin semiconductor.," *Nature Physics,* vol. 13, no. 3, p. 262, 2017.

[34] Novoselov, K.S., Mishchenko, A., Carvalho, A. and Neto, A.C., "2D materials and van der Waals heterostructures.," *Science,* vol. 353, no. 6298, p. 9439, 2016.

[35] Gan, X.T., Zhao, C.Y., Hu, S.Q., Wang, T., Song, Y., Li, J., Zhao, Q.H., Jie, W.Q. and Zhao, J.L.,, "Microwatts continuous-wave pumped second harmonic generation in few-and mono-layer GaSe," *Light: Science & Applications,* vol. 7, no. 1, p. 17126, 2018.

[36] Li, Y., Rao, Y., Mak, K.F., You, Y., Wang, S., Dean, C.R. and Heinz, T.F., "Probing symmetry properties of few-layer MoS2 and h-BN by optical second-harmonic generation.," *Nano letters,* vol. 13, no. 7, p. 3329, 2013.

[37] Kumar, N., Najmaei, S., Cui, Q., Ceballos, F., Ajayan, P.M., Lou, J. and Zhao, H., "Second harmonic microscopy of monolayer MoS2.," *Physical Review B,* vol. 16, no. 87, p. 161403, 2013.

[38] Malard, L.M., Alencar, T.V., Barboza, A.P.M., Mak, K.F. and De Paula, A.M. , "Observation of intense second harmonic generation from MoS 2 atomic crystals," *Physical Review B ,* vol. 87, no. 20, p. 201401, 2013.

[39] Yin, X., Ye, Z., Chenet, D.A., Ye, Y., O'Brien, K., Hone, J.C. and Zhang, X., "Edge nonlinear optics on a MoS2 atomic monolayer," *Science,* vol. 344, no. 6183, p. 488, 2014.

[40] Y. Shen, The principles of nonlinear optics., New York: Wiley-Interscience, 1984.

[41] E.J. Sie, A.J. Frenzel, Y.H. Lee, J. Kong, and N. Gedik, , "Intervalley biexcitons and many-body effects in monolayer MoS2," *Phys. Rev. B,* vol. 92, p. 125417, 2015.

[42] Lui, C.H., Frenzel, A.J., Pilon, D.V., Lee, Y.H., Ling, X., Akselrod, G.M., Kong, J. and Gedik, N., "Trion-induced negative photoconductivity in monolayer MoS2," *Physical review letters,* vol. 113(16) , p. p.166801, 2014.

[43] Mak, K.F., He, K., Shan, J. and Heinz, T.F., "Control of valley polarization in monolayer MoS2 by optical helicity," *Nature nanotechnology,* vol. 7(8), pp. pp.494-498, 2012.

[44] Klingshirn, C.F., Semiconductor optics, Springer Science & Business Media, 2012.

[45] Venema, L., Verberck, B., Georgescu, I., Prando, G., Couderc, E., Milana, S., Maragkou, M., Persechini, L., Pacchioni, G. and Fleet, L., "The quasiparticle zoo," *Nature Physics,* vol. 12(12), pp. 1085-1089, 2016.

[46] Das, S., Chen, H.Y., Penumatcha, A.V. and Appenzeller, J., , "High performance multilayer MoS2 transistors with scandium contacts.," *Nano letters, ,* Vols. 13(1), , pp. pp.100-105., 2012. .

[47] Cui, X., Lee, G.H., Kim, Y.D., Arefe, G., Huang, P.Y., Lee, C.H., Chenet, D.A., Zhang, X., Wang, L., Ye, F., Pizzocchero, F., Bjarke S. Jessen, Kenji Watanabe, Takashi Taniguchi, David A. Muller, Tony Low, Philip Kim, James Hone, "Multi-terminal transport measurements of MoS2 using a van der Waals heterostructure device platform.," *Nature nanotechnology,* 2015.

[48] Lee, C.H., Lee, G.H., Van Der Zande, A.M., Chen, W., Li, Y., Han, M., Cui, X., Arefe, G., Nuckolls, C., Heinz, T.F., Guo, J., James Hone, Philip Kim , "Atomically thin p–n junctions with van der Waals heterointerfaces.," *Nature nanotechnology,* Vols. 9(9),, pp. pp.676-681., 2014 .

[49] Kappera, R., Voiry, D., Yalcin, S.E., Branch, B., Gupta, G., Mohite, A.D. and Chhowalla, M., "Phase-engineered low-resistance contacts for ultrathin MoS2 transistors," *Nature materials,* vol. 13(12), pp. pp.1128-1134., 2014.

[50] Lin, Z., McCreary, A., Briggs, N., Subramanian, S., Zhang, K., Sun, Y., Li, X., Borys, N.J., Yuan, H., Fullerton-Shirey, S.K., Chernikov, A., Hui Zhao, Stephen McDonnell, Aaron M Lindenberg, Kai Xiao, Brian J LeRoy, Marija Drndić, James C M, et al,, "2D materials advances: from large scale synthesis and controlled heterostructures to improved characterization techniques, defects and applications.," *2D Materials,* Vols. 3(4), , p. p.042001., 2016.

[51] Chakraborty, C., Kinnischtzke, L., Goodfellow, K.M., Beams, R. and Vamivakas, A.N., "Voltage-controlled quantum light from an atomically thin semiconductor," *Nature nanotechnology,* vol. 10(6) , pp. pp.507-511., 2015.

[52] Koppens, F.H.L., Mueller, T., Avouris, P., Ferrari, A.C., Vitiello, M.S. and Polini, M., "Photodetectors based on graphene, other two-dimensional materials and hybrid systems.," *Nature nanotechnology,* vol. 9(10) , pp. pp.780-793., 2014.

[53] Ugeda, M.M., Bradley, A.J., Shi, S.F., Felipe, H., Zhang, Y., Qiu, D.Y., Ruan, W., Mo, S.K., Hussain, Z., Shen, Z.X., Wang, F., S. G. Louie, M. F. Crommie, "Giant bandgap renormalization and excitonic effects in a monolayer transition metal dichalcogenide semiconductor.," *Nature materials,* vol. 13(12), pp. pp.1091-1095., 2014.

[54] K. He, N. Kumar, L. Zhao, Z. Wang, K.F. Mak, H. Zhao, and J. Shan , "Tightly bound excitons in monolayer WSe2," *Phys. Rev. Lett.,* vol. 113, p. 026803, 2014.

[55] Zhang, C., Johnson, A., Hsu, C.L., Li, L.J. and Shih, C.K., "Direct imaging of band profile in single layer MoS2 on graphite: quasiparticle energy gap, metallic edge states, and edge band bending," *Nano letters,* vol. 14(5), pp. pp.2443-2447, 2014.

[56] Liu, B., Zhao, W., Ding, Z., Verzhbitskiy, I., Li, L., Lu, J., Chen, J., Eda, G. and Loh, K.P., "Engineering Bandgaps of Monolayer MoS2 and WS2 on Fluoropolymer Substrates by Electrostatically Tuned Many-Body Effects," *Advanced Materials,* vol. 28(30), pp. 6457-6464, 2016.

[57] Gao, S., Liang, Y., Spataru, C.D. and Yang, L., "Dynamical Excitonic Effects in Doped Two-Dimensional Semiconductors," *Nano Letters,* vol. 16(9), pp. pp.5568-5573, 2016.

[58] Hill, H.M., Rigosi, A.F., Roquelet, C., Chernikov, A., Berkelbach, T.C., Reichman, D.R., Hybertsen, M.S., Brus, L.E. and Heinz, T.F., "Observation of excitonic Rydberg states in monolayer MoS2 and WS2 by photoluminescence excitation spectroscopy.," *Nano letters,* vol. 15(5), pp. 2992-2997, 2015.

[59] Borys, N.J., Barnard, E.S., Gao, S., Yao, K., Bao, W., Buyanin, A., Zhang, Y., Tongay, S., Ko, C., Suh, J. , Weber-Bargioni, A., Wu, J., Yang, L., Schuck, P.J., "Anomalous Above-Gap Photoexcitations and Optical Signatures of Localized Charge Puddles in Monolayer Molybdenum Disulfide," *ACS nano,* vol. 11, no. 2, pp. 2115-2123., 2017.

[60] Tongay, S., Suh, J., Ataca, C., Fan, W., Luce, A., Kang, J.S., Liu, J., Ko, C., Raghunathanan, R., Zhou, J., Ogletree, F., Wu, J., et. al., "Defects activated photoluminescence in two-dimensional semiconductors: interplay between bound, charged, and free excitons," *Scientific reports,* vol. 3, p. 2657, 2013.

[61] P.K. Chow, R.B. Jacobs-Gedrim, J. Gao, T.M. Lu, B. Yu, H. Terrones, and N. Koratkar, "Defect-induced photoluminescence in monolayer semiconducting transition metal dichalcogenides," *ACS Nano,* vol. 9, p. 1520, 2015.

[62] Yan, A., Chen, W., Ophus, C., Ciston, J., Lin, Y., Persson, K. and Zettl, A., "Identifying different stacking sequences in few-layer CVD-grown Mo S2 by low-energy atomic-resolution scanning transmission electron microscopy.," *Physical Review B,* p. 93(4), 2016.

[63] B. Radisavljevic, A. Radenovic, J. Brivio, I.V. Giacometti, and A. Kis, "Single-layer MoS2 transistors," *Nat. Nanotechnol.,* vol. 6, p. 147, 2011.

[64] Berghaeuser, G., Malic, E., "Analytical approach to excitonic properties of MoS2," *Physical Review B,* vol. 89, pp. 125309-125309, 2014.

[65] Steinhoff, A., Rosner, M., Jahnke, F., Wehling, T.O. and Gies, C., "Influence of excited carriers on the optical and electronic properties of Mos2," *Nano letters,* vol. 14(7), pp. 3743-3748, 2014.

[66] Ruckenstein, A.E. and Schmitt-Rink, S., "Many-body aspects of the optical spectra of bulk and low-dimensional doped semiconductors," *Physical Review B,* vol. 35(14), p. 7551, 1987.

[67] Cheiwchanchamnangij, T., Lambrecht, W.R., "Quasiparticle band structure calculation of monolayer, bilayer, and bulk MoS2," *Physical Review B,* vol. 85(20), p. 205302, 2012.

[68] Ramasubramaniam, A., "Large excitonic effects in monolayers of molybdenum and tungsten dichalcogenides," *Phys. Rev. B,* vol. 86, p. 115409, 2012.

[69] H. Shi, H. Pan, Y.W. Zhang, and B.I. Yakobson , "Quasiparticle band structures and optical properties of strained monolayer MoS2 and WS2," *Phys. Rev. B,* vol. 87, p. 155304, 2013.

[70] Klots, A.R., Newaz, A.K.M., Wang, B., Prasai, D., Krzyzanowska, H., Lin, J., Caudel, D., Ghimire, N.J., Yan, J., Ivanov, B.L. and Velizhanin, K.A., "Probing excitonic states in suspended two-dimensional semiconductors by photocurrent spectroscopy," *Scientific reports,* vol. 4, pp. 6608-6608, 2014..

[71] Shi, J., Liu, M., Wen, J., Ren, X., Zhou, X., Ji, Q., Ma, D., Zhang, Y., Jin, C., Chen, H. and Deng, S., "All Chemical Vapor Deposition Synthesis and Intrinsic Bandgap Observation of MoS2/Graphene Heterostructures," *Advanced Materials,* vol. 27(44), p. pp.7086, 2015.

[72] Krane, N., Lotze, C., Läger, J.M., Reecht, G. and Franke, K.J., "Electronic structure and luminescence of quasi-freestanding MoS2 nanopatches on Au (111)," *Nano Letters,* vol. 16(8), pp. pp.5163-5168, 2016.

[73] Zhang, C., Wang, H., Chan, W., Manolatou, C. and Rana, F., "Absorption of light by excitons and trions in monolayers of metal dichalcogenide Mo S 2: Experiments and theory," *Physical Review B,* vol. 89(20), p. p.205436, 2014.

[74] Zhou X., Kang K. , Xie S. , Dadgar A. , Monahan N.R., Zhu X.Y. , Park J. , and Pasupathy A.N. , "Atomic-Scale Spectroscopy of Gated Monolayer MoS2," *Nano Lett.,* vol. 16, p. 3148, 2016.

[75] Robert, C., Lagarde, D., Cadiz, F., Wang, G., Lassagne, B., Amand, T., Balocchi, A., Renucci, P., Tongay, S., Urbaszek, B. and Marie, X., "Exciton radiative lifetime in transition metal dichalcogenide monolayers," *Physical Review B,* vol. 93(20), p. 205423, 2016.

[76] Orfanidis, S.J., Electromagnetic waves and antennas, New Brunswick, NJ: Rutgers University, 2002.

[77] Cohen, M.L. and Louie, S.G., Fundamentals of Condensed Matter Physics, Cambridge University Press, 2016.

[78] Sun, D., Rao, Y., Reider, G.A., Chen, G., You, Y., Brézin, L., Harutyunyan, A.R. and Heinz, T.F., "Observation of rapid exciton–exciton annihilation in monolayer molybdenum disulfide," *Nano letters,* vol. 14(10), pp. 5625-5629, 2014.

[79] Hao, K., Specht, J., Nagler, P., Xu, L., Tran, K., Singh, A., Dass,C., Schüller, C., Korn, T., Richter, M., Knorr, A., Li, X., and Moody, G.;, "Neutral and charged inter-valley biexcitons in monolayer MoSe2," *Nature communications,* vol. 8, p. 15552, 2017.

[80] You, Y., Zhang, X.X., Berkelbach, T.C., Hybertsen, M.S., Reichman, D.R. and Heinz, T.F., "Observation of biexcitons in monolayer WSe2," *Nature Physics,* vol. 11(6), p. 477, 2015.

[81] Back, P., Zeytinoglu, S., Ijaz, A., Kroner, M. and Imamoğlu, A., "Realization of an electrically tunable narrow-bandwidth atomically thin mirror using monolayer MoSe2.," *Physical review letters,* vol. 120, no. 3, p. 037401, 2018.

[82] Ross, J.S., Klement, P., Jones, A.M., Ghimire, N.J., Yan, J., Mandrus, D.G., Taniguchi, T., Watanabe, K., Kitamura, K., Yao, W. and Cobden, D.H., "Electrically tunable excitonic light-emitting diodes based on monolayer WSe2 pn junctions.," *Nature nanotechnology,* Vols. 9(4),, pp. pp.268-272., 2014..

[83] Ye, Y., Wong, Z.J., Lu, X., Ni, X., Zhu, H., Chen, X., Wang, Y. and Zhang, X., "Monolayer excitonic laser," *Nature Photonics,* vol. 9(11), pp. 733-737, 2015.

[84] Li, Y., Zhang, J., Huang, D., Sun, H., Fan, F., Feng, J., Wang, Z. and Ning, C.Z., "Room-temperature continuous-wave lasing from monolayer molybdenum ditelluride integrated with a silicon nanobeam cavity," *Nature nanotechnology,* vol. 12, no. 10, p. 987, 2017.

[85] Zhang, H., Lu, S.B., Zheng, J., Du, J., Wen, S.C., Tang, D.Y. and Loh, K.P., "Molybdenum disulfide (MoS2) as a broadband saturable absorber for ultra-fast photonics.," *Optics express,* vol. 22, no. 6, p. 7249., 2014.

[86] Low, T., Chaves, A., Caldwell, J.D., Kumar, A., Fang, N.X., Avouris, P., Heinz, T.F., Guinea, F., Martin-Moreno, L. and Koppens, F., "Polaritons in layered two-dimensional materials.," *Nature materials,* vol. 16, no. 2, p. 182, 2017.

[87] Liu, X., Galfsky, T., Sun, Z., Xia, F., Lin, E.C., Lee, Y.H., Kéna-Cohen, S. and Menon, V.M., "Strong light–matter coupling in two-dimensional atomic crystals," *Nature Photonics,* vol. 9, no. 1, p. 30, 2015.

[88] Liu, X., Bao, W., Li, Q., Ropp, C., Wang, Y. and Zhang, X., "Control of coherently coupled exciton polaritons in monolayer Tungsten Disulphide," *Physical review letters,* vol. 119, no. 2, p. 027403, 2017.

[89] Wang, N., Cheng, L., Ge, R., Zhang, S., Miao, Y., Zou, W., Yi, C., Sun, Y., Cao, Y., Yang, R. and Wei, Y., et. al., "Perovskite light-emitting diodes based on solution-processed self-organized multiple quantum wells.," *Nature Photonics,* vol. 10, no. 11, p. 699, 2016.

[90] Liang, D., Peng, Y., Fu, Y., Shearer, M.J., Zhang, J., Zhai, J., Zhang, Y., Hamers, R.J., Andrew, T.L. and Jin, S. , "Color-pure violet-light-emitting diodes based on layered lead halide perovskite nanoplates.," *ACS nano,* vol. 10, no. 7, pp. 6897-6904, 2016.

[91] Wu, X., Trinh, M.T. and Zhu, X.Y., "Excitonic many-body interactions in two-dimensional lead iodide perovskite quantum wells," *The Journal of Physical Chemistry C,* vol. 119, no. 26, p. 14714, 2015.

[92] Yaffe, O., Chernikov, A., Norman, Z.M., Zhong, Y., Velauthapillai, A., van Der Zande, A., Owen, J.S. and Heinz, T.F., "Excitons in ultrathin organic-inorganic perovskite crystals," *Physical Review B,* vol. 82, no. 4, p. 045414, 2015.

[93] Dou, L., Wong, A.B., Yu, Y., Lai, M., Kornienko, N., Eaton, S.W., Fu, A., Bischak, C.G., Ma, J., Ding, T., Ginsberg, N.S., Wang L.W., Alivisatos A.P., Yang P., "Atomically thin two-dimensional organic-inorganic hybrid perovskites," *Science,* vol. 349, no. 6255, p. 1518, 2015.

[94] Trang, B., Yeung, M., Popple, D.C., Schriber, E.A., Brady, M.A., Kuykendall, T.R. and Hohman, J.N., "Tarnishing Silver Metal into Mithrene," *Journal of the American Chemical Society,* 2018.

[95] Schriber, E.A., Popple, D.C., Yeung, M., Brady, M.A., Corlett, A., Hohman, J.N.;, "Mithrene is a Self-Assembling Robustly Blue-Luminescent Metal-Organic Chalcogenolate Assembly for 2D Optoelectron-ic Applications," *ACS Applied Nano Materials,* 2018.

[96] Muth, J.F., Lee, J.H., Shmagin, I.K., Kolbas, R.M., Casey Jr, H.C., Keller, B.P., Mishra, U.K. and DenBaars, S.P., "Absorption coefficient, energy gap, exciton binding energy, and recombination lifetime of GaN obtained from transmission measurements," *Applied Physics Letters,* vol. 71, no. 18, p. 2572, 1997.

[97] Teke, A., Özgür, Ü., Doğan, S., Gu, X., Morkoç, H., Nemeth, B., Nause, J. and Everitt, H.O., "Excitonic fine structure and recombination dynamics in single-crystalline ZnO," *Physical Review B ,* vol. 70, no. 19, p. 195207, 2004.

[98] Withers, F., Del Pozo-Zamudio, O., Mishchenko, A., Rooney, A.P., Gholinia, A., Watanabe, K., Taniguchi, T., Haigh, S.J., Geim, A.K., Tartakovskii, A.I. and Novoselov, K.S., "Light-emitting diodes by band-structure engineering in van der Waals heterostructures," *Nature materials,* vol. 14, no. 3, p. 301, 2015.

[99] Dufferwiel, S., Schwarz, S., Withers, F., Trichet, A.A.P., Li, F., Sich, M., Del Pozo-Zamudio, O., Clark, C., Nalitov, A., Solnyshkov, D.D. and Malpuech, G., " Exciton–polaritons in van der Waals heterostructures embedded in tunable microcavities.," *Nature communications,* vol. 6, p. 8579, 2015.

[100] Cuthbert, H.L., Wallbank, A.I., Taylor, N.J. & Corrigan, J.F. , "Synthesis and Structural Characterization of [Cu20Se4(μ3-SePh)12(PPh3)6] and [Ag(SePh)]∞," *Zeitschrift für anorganische und allgemeine Chemie ,* vol. 628, p. 2483, 2002.

[101] Zhang, K., Borys, N.J., Bersch, B.M., Bhimanapati, G.R., Xu, K., Wang, B., Wang, K., Labella, M., Williams, T.A., Haque, M.A. and Barnard, E.S., "Deconvoluting the Photonic and Electronic Response of 2D Materials: The Case of MoS2.," *Scientific Reports,* vol. 7, no. 1, p. 16938, 2017.

[102] Amani, M., Lien, D.H., Kiriya, D., Xiao, J., Azcatl, A., Noh, J., Madhvapathy, S.R., Addou, R., Santosh, K.C., Dubey, M., Cho, K., et al,, "Near-unity photoluminescence quantum yield in MoS2," *Science,* vol. 350, no. 6264, p. 1065, 2015.

[103] Schnitzer, I., Yablonovitch, E., Caneau, C., Gmitter, T.J. and Scherer, A. , "30% external quantum efficiency from surface textured, thin-film light-emitting diodes.," *Applied Physics Letters,* vol. 63, no. 16, pp. 2174-2176., 1993.

[104] L. Maserati, S.Refaely-Abramson, C. Kastl, C. Chen, N. J. Borys, C. Eisler, M. Collins, E. Barnard, et al., "Theoretical and Experimental Observation of Anisotropic 2D Excitons in Self-Assembled Hybrid Quantum Wells," *submitted,* 2018.

[105] Haug, H. and Koch, S.W., Quantum theory of the optical and electronic properties of semiconductors (Vol. 5)., Singapore: World scientific., 2004.

[106] Bellessa, J., Voliotis, V., Grousson, R., Wang, X.L., Ogura, M. and Matsuhata, H., "Quantum-size effects on radiative lifetimes and relaxation of excitons in semiconductor nanostructures," *Physical Review B,* vol. 58, no. 15, p. 9933, 1998.

[107] Palummo, M., Bernardi, M. and Grossman, J.C., " Exciton radiative lifetimes in two-dimensional transition metal dichalcogenides," *Nano letters,* vol. 15(5), pp. 2794-2800, 2015.

[108] Y. Matthew, P. Derek, S. Elyse, K. Tevye, J. Hohman, "On the Corrosion of Late- and Post-Transition Metals into Metal-Organic Chalcogenolate Assemblies (MOCHAs)," *submitted,* 2018.

[109] Krasser, W., Ervens, H., Fadini, A. and Renouprez, A.J. , "Raman scattering of benzene and deuterated benzene chemisorbed on silica-supported nickel," *Journal of Raman Spectroscopy,* vol. 9, no. 2, p. 80, 1980.

[110] Asundi, R.K. and Padhye, M.E. , "Fermi resonance in benzene," *Nature ,* vol. 163, no. 4147, p. 638, 1949.

[111] Zhou, M., Wang, K., Men, Z., Gao, S., Li, Z. and Sun, C., "Study of high-pressure Raman intensity behavior of aromatic hydrocarbons: Benzene, biphenyl and naphthalene," *Spectrochimica Acta Part A: Molecular and Biomolecular Spectroscopy,* vol. 97, p. 526, 2012.

[112] Wood, R.W., "Raman spectra of benzene and diphenyl," *Physical Review,* vol. 36, no. 9, p. 1431, 1930.

[113] Green, J.H.S. , "Vibrational spectra of benzene derivatives-III. Anisole, ethylbenzene, phenetole methyl phenyl sulphide and ethyl phenyl sulphide," *Spectrochimica Acta,* vol. 18, no. 1, p. 39, 1962.

[114] T. E. Smidt, "Toward the Systematic Design of Complex Materials from Structural Motifs," *PhD Dissertation,* 2018.

[115] Elyse A. Schriber, Derek C. Popple, Matthew Yeung, Michael A. Brady, Stephen Corlett, J. Nathan Hohman, "Mithrene is a Self-Assembling Robustly Blue-Luminescent Metal-Organic Chalcogenolate Assembly for 2D Optoelectron-ic Applications," *ACS Applied Nano Materials,* 2018.

[116] Janisch, C., Wang, Y., Ma, D., Mehta, N., Elías, A.L., Perea-López, N., Terrones, M., Crespi, V. and Liu, Z., "Extraordinary second harmonic generation in tungsten disulfide monolayers," *Scientific reports,* vol. 4, p. 5530, 2014.

[117] Rivoire, K., Lin, Z., Hatami, F., Masselink, W.T. and Vučković, J.,, "Second harmonic generation in gallium phosphide photonic crystal nanocavities with ultralow continuous wave pump power.," *Optics express,* vol. 17, no. 25, p. 22609, 2009.

[118] Carmon, T. and Vahala, K.J., "Visible continuous emission from a silica microphotonic device by third-harmonic generation.," *Nature Physics,* vol. 3, no. 6, p. 430, 2007.

[119] Basov, D.N., Fogler, M.M. and De Abajo, F.G., "Polaritons in van der Waals materials," *Science,* vol. 354, no. 6309, p. 1992, 2016.

[120] Lin, K.Q., Bange, S. and Lupton, J.M., "Quantum interference in second-harmonic generation from monolayer WSe2.," *Nature Physics,* vol. 15, no. 3, p. 242, 2019.

[121] Yu, X., Scaccabarozzi, L., Harris, J.S., Kuo, P.S. and Fejer, M.M., "Efficient continuous wave second harmonic generation pumped at 1.55 μm in quasi-phase-matched AlGaAs waveguides," *Optics Express,* vol. 13, no. 26, p. 10742, 2005.

[122] Ducci, S., Lanco, L., Berger, V., De Rossi, A., Ortiz, V. and Calligaro, M., "Continuous-wave second-harmonic generation in modal phase matched semiconductor waveguides," *Applied physics letters,* vol. 84, no. 16, p. 2974, 2004.

[123] Hanbicki, A.T., Chuang, H.J., Rosenberger, M.R., Hellberg, C.S., Sivaram, S.V., McCreary, K.M., Mazin, I.I. and Jonker, B.T., "Double indirect interlayer exciton in a MoSe2/WSe2 van der Waals heterostructure.," *ACS nano,* vol. 5, no. 12, p. 4719, 2018.

[124] Rosenberger, M.R., Chuang, H.J., McCreary, K.M., Hanbicki, A.T., Sivaram, S.V. and Jonker, B.T., "Nano-“Squeegee” for the Creation of Clean 2D Material Interfaces.," *ACS applied materials & interfaces,* vol. 10, no. 12, p. 10379, 2018.

[125] Le, C.T., Clark, D.J., Ullah, F., Senthilkumar, V., Jang, J.I., Sim, Y., Seong, M.J., Chung, K.H., Park, H. and Kim, Y.S., "Nonlinear optical characteristics of monolayer MoSe2.," *Annalen der Physik,* vol. 7, no. 528, p. 551, 2016.

[126] Fan, X., Jiang, Y., Zhuang, X., Liu, H., Xu, T., Zheng, W., Fan, P., Li, H., Wu, X., Zhu, X. and Zhang, Q., "Broken symmetry induced strong nonlinear optical effects in spiral WS2 nanosheets," *ACS nano,* vol. 11, no. 5, p. 4892, 2017.

[127] Autere, A., Jussila, H., Dai, Y., Wang, Y., Lipsanen, H. and Sun, Z., "Nonlinear optics with 2D layered materials," *Advanced Materials,* vol. 24, no. 30, p. 1705963, 2018.

[128] R. Sutherland, Handbook of nonlinear optics., New York City: CRC press, 2003.

[129] Li, Y., Chernikov, A., Zhang, X., Rigosi, A., Hill, H.M., van der Zande, A.M., Chenet, D.A., Shih, E.M., Hone, J. and Heinz, T.F., "Measurement of the optical dielectric function of monolayer transition-metal dichalcogenides: MoS2, MoSe2, WS2, and WSe2," *Physical Review B,* vol. 90, no. 20, p. 205422, 2014.

[130] Zhang, X.X., You, Y., Zhao, S.Y.F. and Heinz, T.F., "Experimental evidence for dark excitons in monolayer WSe2.," *Physical review letters,* vol. 115, no. 25, p. 257403, 2015.

[131] Hsu, W.T., Zhao, Z.A., Li, L.J., Chen, C.H., Chiu, M.H., Chang, P.S., Chou, Y.C. and Chang, W.H., "Second harmonic generation from artificially stacked transition metal dichalcogenide twisted bilayers.," *Acs Nano,* vol. 8, no. 3, p. 2951, 2014.

[132] Merano, M., "Nonlinear optical response of a two-dimensional atomic crystal.," *Optics letters,* vol. 41, no. 1, p. 187, 2016.

[133] An, Xiaohong, et al., "Tunable graphene–silicon heterojunctions for ultrasensitive photodetection.," *Nano letters ,* vol. 3, no. 13, p. 909, 2013.

[134] Wang, Xiaomu, et al. , "High-responsivity graphene/silicon-heterostructure waveguide photodetectors.," *Nature Photonics,* vol. 7, no. 11, p. 888, 2013.

[135] Li, Xinming, et al., "Graphene-on-silicon Schottky junction solar cells," *Advanced Materials,* vol. 22, no. 25, p. 2743, 2010.

[136] Jie, Wenjing, Fengang Zheng, and Jianhua Hao., " Graphene/gallium arsenide-based Schottky junction solar cells.," *Applied Physics Letters,* vol. 103, no. 23, p. 233111, 2013.

[137] Zeng, Long-Hui, et al., "Monolayer graphene/germanium Schottky junction as high-performance self-driven infrared light photodetector.," *ACS applied materials & interfaces,* vol. 519, p. 9362, 2013.

[138] Monroy, Eva, Franck Omnès, and Fernando Calle, " Wide-bandgap semiconductor ultraviolet photodetectors.," *Semiconductor Science and Technology,* vol. 418, p. 33, 2003.

[139] Luo, Lei, et al., "Fabrication and characterization of ZnO nanowires based UV photodiodes.," *Sensors and Actuators A: Physical ,* vol. 127, no. 2, p. 201, 2006.

[140] Guo, Fawen, et al. , "A nanocomposite ultraviolet photodetector based on interfacial trap-controlled charge injection.," *Nature nanotechnology,* vol. 7, no. 12, p. 798, 2012.

[141] Koide, Yasuo, et al., "Thermally stable solar-blind diamond UV photodetector.," *Diamond and related materials ,* vol. 15, no. 11, p. 1962, 2006.

[142] Yu, Jie, et al., " Graphene-on-diamond devices with increased current-carrying capacity: carbon sp2-on-sp3 technology.," *Nano letters,* vol. 12, no. 3, p. 1603, 2012.

[143] May, Paul W., "Diamond thin films: a 21st-century material," *Philosophical Transactions of the Royal Society of London A: Mathematical, Physical and Engineering Sciences,* vol. 358, no. 1766, p. 473, 2000.

[144] Koizumi, Satoshi, Christoph Nebel, and Milos Nesladek., Physics and applications of CVD diamond., John Wiley & Sons, 2008.

[145] Pace, E., R. Di Benedetto, and S. Scuderi. , "Fast stable visible-blind and highly sensitive CVD diamond UV photodetectors for laboratory and space applications.," *Diamond and Related Materials,* vol. 9, no. 3, p. 987, 2000.

[146] Pan, L. S., et al., "Carrier density dependent photoconductivity in diamond.," *Applied physics letters ,* vol. 6, no. 57, p. 623, 1990.

[147] Kania, D. R., et al. , "Diamond radiation detectors.," *Diamond and Related Materials,* vol. 2, no. 7, p. 1012, 1993.

[148] Binari, S. C., et al. , "Diamond metal-semiconductor-metal ultraviolet photodetectors," *Diamond and Related Materials,* vol. 2, no. 5, p. 1020, 1993.

[149] Thaiyotin, L., et al, "UV photodetector from Schottky diode diamond film," *Diamond and related materials,* vol. 3, no. 11, p. 442, 2002.

[150] Wang, Xuan, Linjie Zhi, and Klaus Müllen, "Transparent, conductive graphene electrodes for dye-sensitized solar cells.," *Nano letters,* vol. 1, no. 8, p. 323, 2008.

[151] Werner, Matthias, et al., "The effect of metallization on the ohmic contact resistivity to heavily B-doped polycrystalline diamond films.," *Electron Devices, IEEE Transactions on,* vol. 7, no. 42, p. 1344, 1995.

[152] Liang, Xuelei, et al., "Toward clean and crackless transfer of graphene.," *ACS nano,* vol. 5, no. 11, p. 9144, 2011.

[153] Saito, R., et al, "Raman spectroscopy of graphene and carbon nanotubes.," *Advances in Physics ,* vol. 60, no. 3, p. 413, 2011.

[154] Gonon, P., et al. ., "Characterization of heavily B-doped polycrystalline diamond films using Raman spectroscopy and electron spin resonance.," *Journal of applied physics,* vol. 78, no. 12, p. 7059, 1995.

[155] Knight, Diane S., and William B. White., "Characterization of diamond films by Raman spectroscopy.," *Journal of Materials Research* , vol. 4, no. 2, p. 385, 1989.

[156] Pisana, Simone, et al. , "Breakdown of the adiabatic Born–Oppenheimer approximation in graphene," *Nature materials,* vol. 6, no. 3, p. 198, 2007.

[157] Das, Anindya, et al., "Monitoring dopants by Raman scattering in an electrochemically top-gated graphene transistor.," *Nature nanotechnology,* vol. 3, no. 4, p. 210, 2008.

[158] Tan, Y-W., et al., "Measurement of scattering rate and minimum conductivity in graphene.," *Physical Review Letters,* vol. 99, no. 24, p. 246803, 2007.

[159] Chen, Chun-Chung, et al. , "Graphene-silicon Schottky diodes.," *Nano letters,* vol. 5, no. 2011, p. 11, 1863.

[160] Tongay, S., et al., "Rectification at graphene-semiconductor interfaces: zero-gap semiconductor-based diodes.," *Physical Review X,* p. 011002, 2012.

[161] Kang, W. P., et al. , "Temperature dependence and effect of series resistance on the electrical characteristics of a polycrystalline diamond metal-insulator-semiconductor diode.," *Journal of applied physics,* vol. 782, p. 1101, 1995.

[162] Sze, Simon M., and Kwok K. Ng., Physics of semiconductor devices., John Wiley & Sons, 2006.

[163] Liao, Meiyong, Yasuo Koide, and Jose Alvarez, "Thermally stable visible-blind diamond photodiode using tungsten carbide Schottky contact.," *Applied Physics Letters,* vol. 87, no. 2, 2005.

[164] Katz, O., G. Bahir, and J. Salzman, " Persistent photocurrent and surface trapping in GaN Schottky ultraviolet detectors.," *Applied physics letters* , vol. 84, no. 20, p. 4092, 2004.

[165] Kim, Seyoung, et al., "Realization of a high mobility dual-gated graphene field-effect transistor with Al2O3 dielectric.," *Applied Physics Letters,* vol. 94, no. 6, p. 062107, 2009.

[166] Pearton, S. J., et al., "GaN-based diodes and transistors for chemical, gas, biological and pressure sensing.," *Journal of Physics: Condensed Matter* , vol. 29, no. 16, p. 961, 2004.

[167] Koehler, Andrew D., et al., " Extraction of AlGaN/GaN HEMT Gauge factor in the presence of traps.," *Electron Device Letters, IEEE,* vol. 31, no. 7, p. 665, 2010.

[168] Chang, Chia-Ta, et al., "Changes of electrical characteristics for AlGaN/GaN HEMTs under uniaxial tensile strain.," *Electron Device Letters, IEEE,* vol. 30, no. 3, p. 213, 2009.

[169] Chu, S. N. G., et al., "Piezoelectric polarization-induced two dimensional electron gases in AlGaN/GaN heteroepitaxial structures: Application for micro-pressure sensors.," *Materials Science and Engineering: A* , vol. 409, no. 1, p. 340, 2005.

[170] Eickhoff, M., et al., "Piezoresistivity of AlxGa1-xN layers and AlxGa1-xN/GaN heterostructures.," *Journal of Applied Physics,* vol. 90, no. 7, p. 3383, 2001.

[171] EpiGaN, *Kempische steenweg 293, 3500 Hasselt, Belgium..*

[172] Timoshenko, Stephen., Strength of materials., New York, 1930.

[173] Ghosh, Sudip, et al., "Surface-Potential-Based Compact Modeling of Gate Current in AlGaN/GaN HEMTs.," *Electron Devices, IEEE Transactions on,* vol. 62, no. 2, p. 443, 2015.

[174] Khandelwal, Sourabh, Nitin Goyal, and Tor A. Fjeldly. , "A physics-based analytical model for 2DEG charge density in AlGaN/GaN HEMT devices.," *Electron Devices, IEEE Transactions on,* vol. 58, no. 10, p. 3622, 2011.

[175] Khandelwal, Sourabh, and Tor A. Fjeldly. , "A physics based compact model of I–V and C–V characteristics in AlGaN/GaN HEMT devices.," *Solid-State Electronics,* vol. 76, p. 60, 2012.

[176] Ambacher, O., et al. , "Two dimensional electron gases induced by spontaneous and piezoelectric polarization in undoped and doped AlGaN/GaN heterostructures.," *Journal of applied physics,* vol. 87, no. 1, p. 334, 2000.

[177] Bernardini, Fabio, Vincenzo Fiorentini, and David Vanderbilt, "Spontaneous polarization and piezoelectric constants of III-V nitrides," *Physical Review B,* vol. 16, no. 56, p. R10024, 1997.

[178] Shimada, Kazuhiro, Takayuki Sota, and Katsuo Suzuki., "First-principles study on electronic and elastic properties of BN, AlN, and GaN.," *Journal of Applied Physics,* vol. 84, no. 9, p. 4951, 1998.

[179] Tsubouchi, K., K. Sugai, and N. Mikoshiba, " AlN material constants evaluation and SAW properties on AlN/Al 2 O 3 and AlN/Si," *1981 Ultrasonics Symposium. IEEE,* 1981.

[180] Wright, A. F., " Elastic properties of zinc-blende and wurtzite AlN, GaN, and InN," *Journal of Applied Physics ,* vol. 6, no. 82, p. 2833, 1997.

[181] Iucolano, Ferdinando, et al. , "Influence of high-temperature GaN annealed surface on the electrical properties of Ni/GaN Schottky contacts.," *Journal of Applied Physics ,* vol. 9, no. 104, p. 3706, 2008.

[182] Bermudez, V. M. , "Simple interpretation of metal/wurtzite–GaN barrier heights.," *Journal of applied physics,* vol. 86, no. 2, p. 1170, 1999.

[183] Mamor, M. , "Interface gap states and Schottky barrier inhomogeneity at metal/n-type GaN Schottky contacts.," *Journal of Physics: Condensed Matter,* vol. 21, no. 33, p. 335802, 2009.